Coherent Spin Dynamics of a Spin-1 Bose-Einstein Condensate

A Thesis
Presented to
The Academic Faculty

by

Ming-Shien Chang

In Partial Fulfillment
of the Requirements for the Degree
Doctor of Philosophy

School of Physics
Georgia Institute of Technology
May 2006

Coherent Spin Dynamics of a Spin-1 Bose-Einstein Condensate

Approved by:

Professor Michael S. Chapman
School of Physics, Chair

Professor T. A. Brian Kennedy
School of Physics

Professor Chandra Raman
School of Physics

Professor Alex Kuzmich
School of Physics

Professor Gee-Kung Chang
School of Electrical and Computer Engineering

Date Approved: March, 29, 2006

To my parents,

Mr. Muh-Yen Chang and Mrs. Hsueh-Huang Chang

ACKNOWLEDGEMENTS

I would like to take this opportunity to thank the people who have inspired and supported me throughout my PhD studies. First, I would like to express my greatest gratitude to my advisor, Prof. Michael Chapman. Mike has amazing physics intuition and talent for solving challenging technical problems simply and cleverly. His great insight and capability has helped us from going in wrong directions to search for answers. Mike taught me how to be a good experimentalist. However, perhaps the more valuable things I learned from him are his optimistic attitude and leadership. I will offer two examples to demonstrate Mike's leadership. One day, I realized that our experiment control center, a heavy table hosting computers and power equipment, was too close to our vacuum chamber, and the magnetic noise from this table was badly affecting our measurements. Mike knew that I was going to move the control center in an evening. So he showed up that night, and we ended up moving heavy instruments and tossing perhaps 50 cables across the lab at midnight. While working on creating BECs in a single focus trap, we decided to compress the trap. Again, Mike was the person who pushed a manual translation stage for me in the late night for few hours, and, that night, we made the first "hand-made" BECs in the single focus trap. For Mike's advice and great leadership, he has my highest regard.

Next, I would like to extend my gratitude to Prof. Brian Kennedy, Li You, Chandra Raman, and Alex Kuzmich, for offering their expertise and physics insight through many stimulating discussions. Especially Brian, he always patiently cleared up my thoughts through rigorous deductions no matter how minute the questions I had.

I am grateful to work with several wonderful and talented lab colleagues after I arrived Georgia Tech. Prof. Murray Barrett was finishing up his thesis when I joined the lab. Working with Murray was very productive, and his determination and diligence really impressed me and has continued to inspire me throughout these years. After Murray left, Dr. Jacob Sauer helped me to quickly fill my knowledge gap on running the experiment with

his great experience. Jake is a versatile physicist with a vivid personality; it is always fun to have Jake involved, either at work of after school. Kevin Fortier not only works hard and sets a high standard on work ethics, but is a very good friend after school. Chris Hamley is a special and talented undergraduate student. His electronics knowledge and hands-on skills are far beyond what an undergraduate student should know. His beautiful work on the microwave electronics and horn have made our spinor studies possible. The beautiful Thor's Hammer (glass cell) he built is still awaiting to be turned into a BEC chamber.

I am also grateful to work with my theory collaborator, Dr. Wenxian Zhang. I have learned much physics of spinor condensates through countless discussions with him. I am also indebted to Wenxian for the numerical simulations he has done, which provided valuable insights for our spinor experiments.

I wish to thank our new postdoc Dr. Paul Griffin, and my junior colleagues, Qishu Qin, Eva Bookjans, Sally Maddocks, Shane Allman, Soo Kim, Michael Gibbons, Adam Steele, and Layne Churchill for their great help on the experiments, thesis proofread, and for companionship. I also would like to acknowledge colleagues from other groups. I have enjoyed discussing physics with Devang Naik, Stewart Jenkins, Dzmitry Matsukevich, Dr. Mishkatul Bhattacharya, Dr. Sergio Muniz, and others in the Journal Club.

Special thanks to Prof. Glenn Edwards of Duke Physics and Free Electron Laser Laboratory, and my good friend, Dr. Meng-Ru Li. Glenn was a kind advisor when I worked with him on biophysics, and his wise encouragement has continued to inspire me throughout these years. I would never thought of joining Georgia Tech were it not for an accidental crossover between Meng-Ru and Prof. Li You in a biophysics summer school. Meng-Ru mentioned my existence to Li, which in turn led to my great adventure at Tech.

Finally, I would like to thank my parents and my sisters for their unconditional and endless love and support throughout my endeavor. Their constant support make what I am today. For that, I am forever indebted to them.

Georgia Institute of Technology
May 2006

TABLE OF CONTENTS

LIST OF TABLES

LIST OF FIGURES

SUMMARY

Bose-Einstein condensation (BEC) is a well-known phenomenon in which identical bosons occupy the same quantum state below a certain critical temperature. A hallmark of BEC is the coherence between particles — every particle shares the same quantum wave function and phase. This matter wave coherence has been demonstrated for the external (motional) degrees of freedom by interfering two condensates. In this thesis, we show that the coherence extends to the internal spin degrees of freedom of a spin-1 Bose gas by observing coherent and reversible spin-changing collisions. The observed coherent dynamics are analogous to Josephson oscillations in weakly connected superconductors and represent a type of matter-wave four-wave mixing. We also demonstrate control of the coherent evolution of the system using magnetic fields.

In the first part of this thesis, the all-optical approaches to BEC that were first developed in our laboratory will be introduced. All-optical formation of Bose-Einstein condensates (BEC) in 1D optical lattice and single focus trap geometries will be presented. These techniques offer considerable flexibility and speed compared to magnetic trap approaches, and the trapping potential can be essentially spin-independent. These optical traps are ideally suited for studying condensates with internal spin degrees of freedom, so-called *spinor* condensates.

The second part of this thesis will be devoted to the study of spinor condensates. This new form of coherent matter exhibits complex internal structure, and the delicate interplay of the different magnetic quantum gases yields a rich variety of phenomenon including coherent spin mixing and spin domain formation. We begin our study on spinor condensates by tailoring the internal spin states of the spinor condensate. Using condensates with well-defined initially non-equilibrium spin configuration, spin mixing of $F = 1$ and $F = 2$ spinor condensates of ^{87}Rb atoms confined in an optical trap is observed. The equilibrium spin configuration in the $F = 1$ manifold is measured from which we confirm ^{87}Rb to be ferromagnetic. The coherent spinor dynamics are demonstrated by initiating spin mixing deterministically with a non-stationary spin population configuration. Finally, the interplay between the coherent spin mixing and spatial dynamics in spin-1 condensates with ferromagnetic interactions are investigated.

CHAPTER I

INTRODUCTION

Bose-Einstein condensation (BEC) in dilute atomic gases was first observed in 1995 [1, 2, 3], culminating a 20 year effort that began in the 1970s with atomic hydrogen [4, 5] and later with laser-cooled alkali atoms [6, 7]. Since initial observations of BEC in dilute gases, research in this field has grown with tremendous momentum, both experimentally and theoretically. Here we provide a brief and necessarily incomplete review of some of the developments over the past 11 years to highlight some of the distinctive properties of this new form of matter and to illustrate the vibrancy of this young research field.

1.1 A Brief Review of Bose-Einstein Condensation

Bose-Einstein condensation is a phenomenon whereby identical bosonic particles lose their individuality and act in unison as a single quantum entity through macroscopic occupation of a single quantum state. Condensation into a single quantum state occurs for identical bosons when the inter-particle separation is less than the thermal de Broglie wavelength of the particles, or, more precisely, when $n\,\lambda_{\mathrm{dB}}^3 > 2.612$, where n is the particle density and $\lambda_{\mathrm{dB}} = h/\sqrt{2\pi m k_{\mathrm{B}} T}$ is the thermal de Broglie wavelength. Here, h, k_{B}, m, and T are the Planck constant, Boltzmann constant, atomic mass, and temperature of the gas, respectively. For a room temperature gas, λ_{dB} is much less than the size of an atom, and although λ_{dB} increases for lower temperature, conventional condensation to liquid or solid will occur long before reaching the quantum degenerate regime [8]. Hence, an atomic BEC is a supercooled metastable state that exists in an ultrahigh vacuum chamber, and depending on the vacuum condition, the lifetime of a condensate ranges from only few seconds to few minutes [8, 9]. To prevent formation of normal condensed states, which occurs via three-body collisions leading to molecule formation, atoms must be kept at low densities, typically on the order of 10^{14} cm^{-3}, which is 5 orders of magnitude lower than ambient air pressure.

At such low densities, atoms need to be cooled to the sub-microKelvin regime in order to observe Bose-Einstein condensation.

In a Bose condensate, every atom possesses an identical spatial wavefunction, and the coherent superposition of these wavefunctions results in a macroscopic coherent matter wave. With a typical atomic diameter of 0.5 Å, it is quite extraordinary that the BEC wavefunction can be as large as 100 μm [10]. This matter wave coherence is perhaps the most appreciated hallmark of Bose-Einstein condensates, and several experiments have been devoted to demonstrating and studying this property. The macroscopic matter wave coherence was first demonstrated by the MIT group by interfering two independent BEC's [10]. Later, a type of double-slit experiment performed above and below the BEC transition temperature by the Munich group demonstrated that there is a fundamental difference between Bose condensed atoms and thermal atoms [11] — a BEC possesses a macroscopic wavefunction with a unique phase, while a cloud of thermal atoms does not. The observation of Josephson tunnelling of BECs between adjacent trapping potential wells demonstrated tunnelling of these macroscopic wavepackets, which is due to the phase difference between adjacent BECs [12, 13]. Condensates loaded in a 3D optical lattice have been observed to show transitions between the Mott-Insulator phase and the superfluidity phase [14], which showed that phase coherence can be established among many trapping potentials, or lattice sites, when wavepackets are allowed to tunnel between lattice sites. In analogy with coherent optical fields, a Bose condensate coupled out of the trap forms a so-called atom laser [15, 12, 16, 17]. In addition, higher order coherence, such as density correlations of condensates reflecting the statistical properties of boson fields has also been demonstrated [18, 19].

Bose-Einstein condensate is a second order phase transition in which bosons begin to macroscopically occupy the ground state when the temperatures falls below the phase transition temperature. A hallmark of atomic Bose-Einstein condensates is the relatively weak and well-characterized inter-atomic interactions that allow quantitative comparison with theory. Although textbook discussions of Bose-Einstein condensation typically focus on non-interacting (ideal) particles, interactions between the atoms, via elastic inter-atomic collisions, are required for a trapped gas to reach thermal equilibrium and for evaporative cooling of the gas to quantum degeneracy. Atomic interactions also affect the ground state and the dynamical properties of a BEC [20, 21]. In particular, repulsive interactions are required to maintain a large condensate from collapsing [22, 23].

An atomic BEC is typically well-described by a scalar order parameter $\psi(\vec{r},t)$ (the BEC "wavefunction") whose dynamics are governed by the Gross-Pitaevskii equation (or nonlinear Schrödinger equation) [24],

$$i\hbar\frac{\partial\psi}{\partial t} = -\frac{\hbar^2}{2m}\nabla^2\psi + V_t\psi + g|\psi|^2\psi, \tag{1.1}$$

where V_t is the external trapping potential, g is the two-body mean-field interaction coefficient, and $|\psi|^2 = n$ is the particle density. The weak atomic interactions, parameterized by g, are responsible for superfluid behavior of the gas, which can manifest as quantized vortices [25, 26, 27] and superfluid sounds [28, 29, 30]. In addition, the nonlinear nature of the atomic interactions has also allowed observations of bright and dark solitons in condensates [31, 32, 33].

The standard recipe for creating condensates in the lab involves laser cooling to the μK regime followed by evaporative cooling to quantum degeneracy in an atom trap. While for the first five years, condensates were created exclusively in magnetic traps, evaporation in an optical trap, developed in our laboratory, provides a simple and fast alternative approach for preparing an atomic BEC [34], and it is ideally suited for trapping atomic and molecular states that are not amenable to magnetic trapping [35, 34, 36]. Recently, condensates have been created in magnetic micro traps using lithographically patterned wires on a solid-state chip. These techniques offer prospects for miniaturization of the BEC apparatus, and also provides opportunities for studying interactions between ultracold atoms and the chip surface [37, 38].

1.2 Spinor Condensates

The vast majority of experimental work has involved single species and single component systems, using magnetic traps to confine just one Zeeman sub-level in the ground state hyperfine manifold. An important frontier in BEC research is the extension to multi-species and multi-component systems, which provides a unique opportunity to explore coupled, interacting quantum fluids. In particular, atomic BECs with internal spin degrees of freedom, or the so-called *spinor* condensates, offer a new form of coherent matter with complex internal quantum structures. These multi-component BEC systems are related to other macroscopic quantum systems in which internal degrees of freedom [39, 40, 41, 42, 34, 43, 44, 45] play a prominent role including superfluid ^{3}He [46, 47], neutron stars [48], p-wave [49] and d-wave BCS superconductors [50], while offering the exquisite control and microscopic understanding characteristic of weakly interacting quantum degenerate gases. In this thesis, we focus our studies on the dynamics of spinor condensates in optical traps.

The first two-component condensate was produced utilizing two hyperfine states of ^{87}Rb, and remarkable phenomena such as phase separation and Rabi oscillations between these two components were observed [41, 51]. Sodium $F = 1$ spinor BECs have been created by transferring spin polarized condensates into a far-off resonant optical trap to liberate the internal spin degrees of freedom [35]. This allowed investigations of the ground state properties of Na spinor condensates, and observations of domain structures, metastability, and quantum spin tunneling [42, 52, 53].

A single-component BEC is described by a scalar order parameter, and its dynamics are governed by Eq. 1.1. For spinor condensates, the formalism is extended to a vector order parameter $\vec{\psi} = [\psi_F, \psi_{F-1}, \cdots, \psi_{-F}]^{\mathrm{T}}$, which possesses $2F + 1$ components for spin-F condensates [39, 40] and is invariant under rotation in spin space [39, 40, 54]. For $F = 1$, the two-body interaction energy including spin is $U(r) = \delta(r)(c_0 + c_2\vec{F_1} \cdot \vec{F_2})$, where r is the distance between two atoms and c_2 is the spin dependent mean-field interaction coefficient. For $F = 2$, $U(r) = \delta(r)(\alpha + \beta\vec{F_1} \cdot \vec{F_2} + 5\gamma P_0)$, where α is a spin-independent coefficient, β and γ are spin-dependent coefficients, and P_0 is the projection operator [39, 40].

For a spin-1 BEC, the condensate is either ferromagnetic or anti-ferromagnetic [39], and the corresponding ground state structure and dynamical properties of these two cases are very distinct. The Na $F = 1$ spinor was found to be anti-ferromagnetic, while the $F = 1$ ^{87}Rb was predicted to be ferromagnetic [55, 56]. Even richer dynamics are predicted for spin-2 condensates [50], although they remain largely unexplored experimentally [43, 44].

1.3 Thesis Overview

In the first part of this thesis, we will describe our all-optical BEC experiments and present the creation of condensates in two new trap geometries. In the second part of the thesis, we will present the results of the studies on the dynamics of spinor condensates in our optical traps.

Chapter 2 describes our BEC experiment setup. The basic atomic physics and properties of ^{87}Rb relevant to this thesis are given. The background and implementation of laser cooling and optical dipole force trap are also briefly summarized. Chapter 3 introduces the probe techniques we use in our experiment to measure the properties of the ultracold gas.

In Chapter 4 the loading dynamics of different trap geometries are examined. The understanding gained from these studies has allowed us to create BECs in several different trap arrangements including a cross trap geometry [34], a 1D optical lattice geometry, and a single focus geometry. This latter configuration has resulted in a 10-fold increase in the number of condensed atoms in our experiments.

Chapters 5 to 8 are devoted to the studies of spinor condensates in optical traps. Chapter 5 introduces the microscopic theory of spinor condensates and spinor dynamics to provide the theoretical foundation of our experimental results. Chapter 6 details the experimental observation of the individual spinor components and spinor dynamics. In Chapter 7 coherent spinor dynamics, notably spin mixing, are examined. The ability to coherently control the spin mixing and the spinor ground state is demonstrated. The spatial dynamics of spinor condensates are examined in further details in Chapter 8. Observations of spin waves and spin domain formation are presented.

Chapter 9 concludes this thesis, and provides some final remarks and possible future research directions.

CHAPTER II

THE EXPERIMENTAL SETUP

Bose-Einstein Condensation (BEC) in a dilute atomic gas was first achieved in 1995 [1, 2, 3] by evaporative cooling a laser cooled atomic gas in a magnetic trap. Since then, this basic technique has been duplicated by over 30 groups worldwide. In this approach, $10^8 - 10^{10}$ atoms are captured and cooled to 100 μK regime in a magneto-optical trap (MOT). In the MOT, the density is limited to $< 10^{12}$ cm^{-3}, and the phase space density is 10^{-6}. The laser cooled atoms are then loaded into a magnetic trap and evaporative cooled to quantum degeneracy.

An all-optical approach to making condensates was first pioneered in our laboratory in 2001 and provided an alternative, simple and fast approach for preparing atomic condensates. Optical traps can provide tighter confinement for the atoms than a magnetic trap, and this can lead to higher density and efficient, fast evaporation in the trap. Our BEC machine consists of a simple vapor cell magneto-optical trap (MOT) and tightly focused CO_2 lasers [34]. This chapter briefly describes our BEC experimental setup.

2.1 Rubidium-87 Properties

The atomic number of rubidium is 37, and the ground state electron configuration is [Kr]5s^1, or $5^2S_{1/2}$ after L-S coupling. The atomic spin is given by $\vec{F} = \vec{I} + \vec{J}$, where $\vec{I}$ is the nuclear spin and $\vec{J}$ is the total angular momentum of the valence electron. For rubidium and all other alkali atoms in the electronic ground state, $\vec{J} = \vec{S}$ and $J = S = 1/2$ because $\vec{J} = \vec{L} + \vec{S}$ and $\vec{L} = 0$. Here $\vec{L}$ and $\vec{S}$ are the electronic orbital angular momentum and spin. This results in doublet ground states in all alkali atoms, *i.e.*, $F_{\text{upper}} = I + 1/2$ and $F_{\text{lower}} = I - 1/2$. The nuclear spin of ^{87}Rb is $I = 3/2$, so $F_{\text{upper}} = 2$ and $F_{\text{lower}} = 1$. The energy difference between these two states, the ground hyperfine splitting, is ~ 6.835 GHz.

The single valence electron of alkalis also leads to two first excited states, which for Rb are the $5^2\mathrm{P}_{1/2}$ and $5^2\mathrm{P}_{3/2}$ states that are separated by the fine structure splitting. The optical transitions between the ground state and these excited states constitute the famous D transitions, *i.e.*, the D_1 and D_2 lines. The ground and first excited hyperfine structures and the optical transitions of ^{87}Rb are illustrated in Fig. 2.1(a). The D_2 transitions are used for laser cooling and for probing in this thesis, and the precise frequencies of hyperfine splitting and the D_2 transition wavelength are given in the Fig. 2.1(b).

In each F state, there are $2F+1$ Zeeman sublevels, labeled as $m_F = F, F-1, \cdots, -F$. The selection rules for the electric dipole $S \leftrightarrow P$ optical transitions are $\Delta F, \Delta m_F = 0, \pm 1$, except for $m_F = 0 \leftrightarrow m_{F'} = 0$ when $\Delta F = 0$. These selection rules allow the $5^2\mathrm{S}_{1/2}$, $|F = 2, m_F = \pm 2\rangle$ and $5^2\mathrm{P}_{3/2}$, $|F = 3, m_F = \pm 3\rangle$ states (shorthand: $|F = 2, m_F = \pm 2\rangle$ and $|F' = 3, m_{F'} = \pm 3\rangle$) to form closed two-level systems. In addition, the optical transitions between $F = 2$ and $F' = 3$ refers to the cycling transitions (see Fig. 2.1(a)). These transitions are very important because they enable an atom to repeatedly scatter photons from a laser beam tuned to this transition frequency, which is the key for efficient laser cooling.

The degeneracy of the m_F states is lifted in the presence of a magnetic field. The magnetic energy shift, or Zeeman shift, of each m_F state can be calculated using the Breit-Rabi formula [58], and for the three m_F (1, 0, -1) states in the ground $F = 1$ manifold they are given as

$$\begin{aligned} E_1 &= -\frac{E_\mathrm{hfs}}{8} - g_I\mu_\mathrm{I}B - \frac{1}{2}E_\mathrm{hfs}\sqrt{1+x+x^2} \\ E_0 &= -\frac{E_\mathrm{hfs}}{8} - \frac{1}{2}E_\mathrm{hfs}\sqrt{1+x^2} \\ E_{-1} &= -\frac{E_\mathrm{hfs}}{8} + g_\mathrm{I}\mu_\mathrm{I}B - \frac{1}{2}E_\mathrm{hfs}\sqrt{1-x+x^2}, \end{aligned} \tag{2.1}$$

where

$$x = \frac{g_\mathrm{I}\mu_\mathrm{I}B + g_\mathrm{J}\mu_\mathrm{B}B}{E_\mathrm{hfs}}.$$

Here E_hfs is the hyperfine splitting, g_I and g_J are the Landé g-factor for the nucleus and the valence electron, μ_I and μ_B are the nuclear magnetic moment and the Bohr magneton, and B is the magnetic field. Since $g_\mathrm{I}\mu_\mathrm{I} \ll g_\mathrm{J}\mu_\mathrm{B}$, $g_\mathrm{I}\mu_\mathrm{I}$ is often neglected and $x \simeq g_\mathrm{J}\mu_\mathrm{B}B/E_\mathrm{hfs}$. The atomic parameters for ^{87}Rb are given in Appendix A, and the energy shift of ground

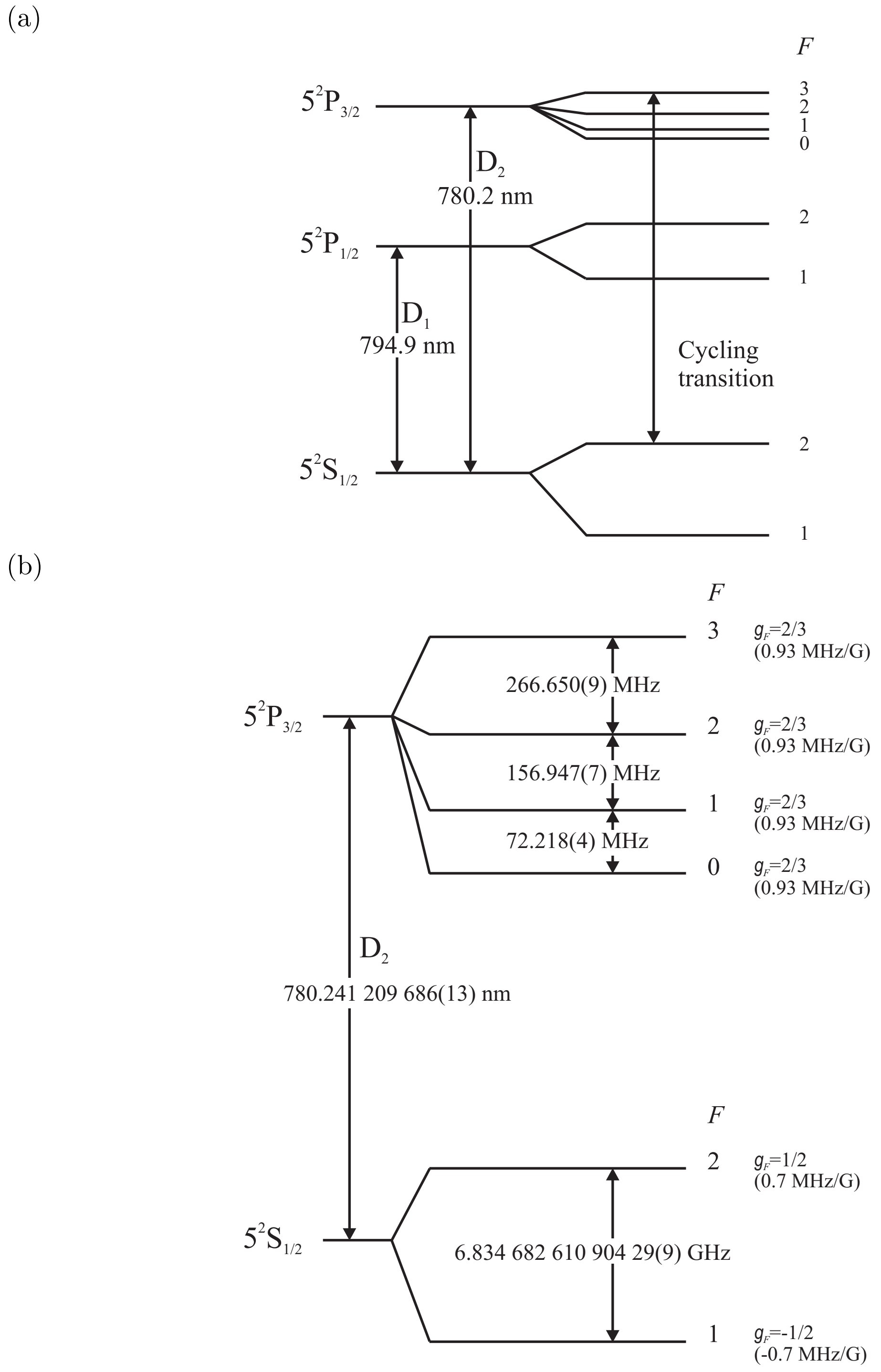

Figure 2.1: (a) ^{87}Rb D transition hyperfine structure. (b) Detailed D_2 transition hyperfine structure [57].

hyperfine states vs. magnetic field is plotted in Fig. 2.2(a). In the low fields, the energy splitting between two adjacent m_F states is ~ 0.7 MHz/G.

In the studies of spinor condensates, we have used microwaves tuned to the ground state hyperfine transitions to measure and zero the magnetic fields in the optical traps and to manipulate the internal spin states of the condensates. The allowed magnetic transitions between the $F = 1$ and $F = 2$ states and a typical microwave spectrum are shown in Fig. 2.2(b).

2.2 Magneto-Optical Trap

The magneto-optical trap (MOT), based on laser cooling, has provided an efficient and straightforward way to capture and cool millions of atoms to the micro-Kelvin regime. Since its invention in 1987 [6], magneto-optical trapping has become the workhorse for modern ultracold atomic physics in the micro-Kelvin regime.

The first atomic Bose-Einstein condensates were achieved using the alkali species: ^{87}Rb, ^{7}Li, and ^{23}Na. Between 1995 and 2003 all of the stable alkali bosonic isotopes and many of the fermionic isotopes have been cooled to quantum degeneracy. A very important reason for this success is that alkali atoms exhibit strong optical cycling transitions as noted in the last section, which enable efficient laser cooling to the μK regime. In BEC experiments, the MOT provides an increase in the phase space density (PSD) by a factor of over 10^9 from ambient conditions and provides favorable initial conditions for subsequent evaporation to quantum degeneracy.

The standard MOT consists of three orthogonal pairs of counter-propagating circularly polarized laser beams and a pair of anti-Hemholtz coils. The lasers are tuned to the red of the cycling transition by a few atomic linewidths for Doppler laser cooling [6]. The anti-Hemholtz coils (MOT coils) create a spatially varying Zeeman shift for the laser cooled atoms. The combination of the MOT coils and cooling lasers creates a spatial-dependent and velocity dependent radiation pressure that provide both a restoring and viscous force for the atoms.

The trap depth of a typical MOT is only ~ 1 mK. If it is used to directly capture atoms

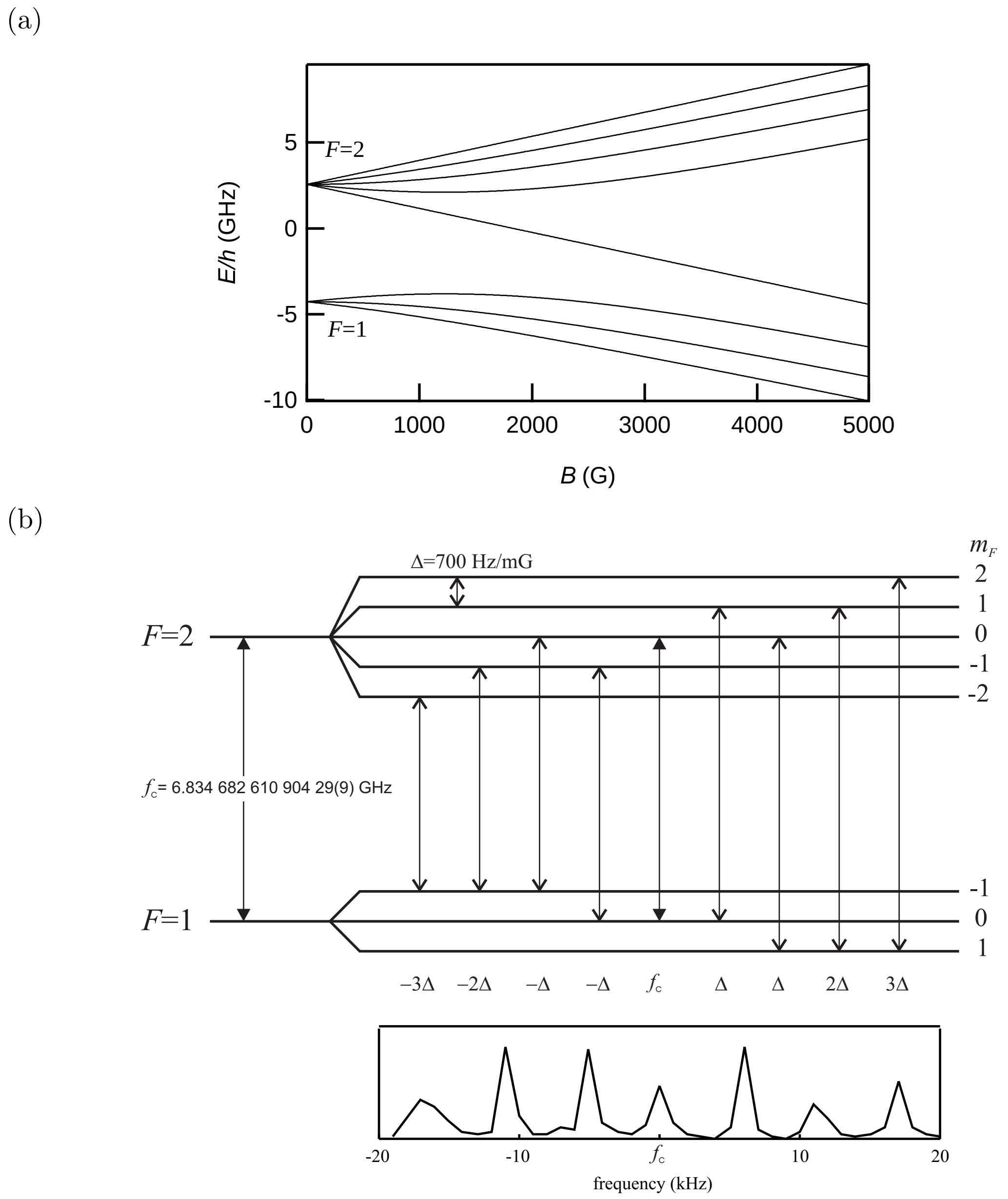

Figure 2.2: Ground hyperfine levels of ^{87}Rb. (a) The Zeeman splitting of ground $F = 1$ and $F = 2$ hyperfine states vs. magnetic field. (b) The magnetically allowed transitions between $F = 1$ and $F = 2$ states. The lower plot is a typical microwave spectrum of ultracold clouds with 1 kHz resolution in a field of 8 mG.

from a vapor at 300 K, it can only capture the atoms in the low velocity tail of the Boltzmann distribution. To enhance the capture efficiency of the MOT, various enhancement techniques have been developed. These include a Zeeman slower to increase the brightness of the atomic bream, and a double MOT system to transfer a MOT from a high pressure chamber to a low pressure chamber. In our experiment, neither of these two techniques is necessary. Thorough information of laser cooling and the MOT can be found in ref. [59].

2.2.1 Diode Lasers

One advantage of working with rubidium is that one can find inexpensive high-power single mode laser diodes and diode amplifier chips delivering up to 1 W at 780 nm. In addition, diodes lasers are compact, long lasting, and almost maintenance-free following initial setup. Furthermore, the laser linewidth can be easily reduced to below 1 MHz and locked to atomic transitions following well established techniques [60, 61, 62].

In this thesis, some of the experiments were done with homemade diode lasers. Lately, 1 W tapered diode amplifiers have become available, and we have recently used these amplifiers in our experiments.

The cooling lasers (MOT lasers) are tuned to the $F = 2 \leftrightarrow F' = 3$ transition of ^{87}Rb. Each laser beam is circularly polarized to favor $\sigma^{\pm}$ transitions ($\Delta m = \pm 1$). Although the MOT laser frequency is tuned close to the $F = 2 \leftrightarrow F' = 3$ transition, there is a small probability that the atoms can be excited to the $F' = 2$ state, which can spontaneously decay to the $F = 1$ ground state. Due to the large ground state hyperfine splitting, atoms in the $F = 1$ state are decoupled from the cooling light. To repump these atoms, a second laser resonant with the $F = 1 \leftrightarrow F' = 2$ transition is added to optically pump the atoms back to the $F = 2$ state — this is referred to as the repump laser.

The experiment requires up to four MOT lasers and one repump laser. As shown in Fig. 2.5 we use a master-slave configuration for the MOT lasers. An external-cavity diode laser (ECDL) serving as a master laser is frequency stabilized to an atomic transition of Rb. The output of the master laser is frequency shifted by a frequency tunable acousto-optic modulator (AOM), and then seeds three slave lasers. Each slave laser is sent through an

AOM to provide control of the optical power and then coupled into a single-mode, polarization maintaining optical fiber. After exiting the fiber, each beam is expanded, collimated, and then directed into the vacuum chamber through anti-reflection coated viewports. The typical power at the fiber output is $20 \sim 40$ mW, and the $1/e^2$ radius of each MOT beam is 12.5 mm. The repump laser is combined with one slave laser and then coupled into the same fiber. The repump power at the fiber output is 12 mW. The six MOT beams are formed by retro-reflecting the three MOT beams.

2.2.2 Laser Frequency Stabilization and Tuning

The diode lasers are first stabilized by controlling the temperature and diode current [63, 64, 65] with homemade temperature servo system and current controllers. The linewidth of master laser is then reduced to below 1 MHz by an external cavity, formed with an 1800 lines/mm grating in the Littrow configuration. The cavity length is controlled by a piezo-electric actuator (PZT). The master laser is locked to a Doppler-free atomic absorption signal obtained from a standard saturated absorption setup. The laser frequency is stabilized to an absorption peak using frequency modulation (FM) spectroscopy by locking it to a zero crossing point of the FM signal using a PI (proportional-integral) circuit. The setup for the FM spectroscopy is shown in Fig. 2.3, and the saturated absorption spectra and FM signal of ^{87}Rb D_2 transitions are shown in Fig. 2.4.

Doppler laser cooling requires the cooling lasers to be frequency stabilized to the red of the cycling transition. In the experiment, the master laser frequency is locked to the crossover of $F = 2 \leftrightarrow F' = 3$ and $F = 2 \leftrightarrow F' = 1$ transitions, which is -211.8 MHz below the cycling transition (see Fig. 2.4). To change the detuning between the MOT lasers and the cycling transition, the master laser output is shifted using a frequency tunable AOM. This AOM is configured in a double-pass configuration and the output laser beam of the AOM is then used to injection lock three slave lasers. The layout of the diode lasers is shown in Fig. 2.5. The frequency of the MOT beams can be changed from -180 MHz to +20 MHz relative to the cycling transition within $< 100\ \mu$s. This detuning range allows us to achieve sub-Doppler cooling in the final stage of the MOT. The typical MOT detuning

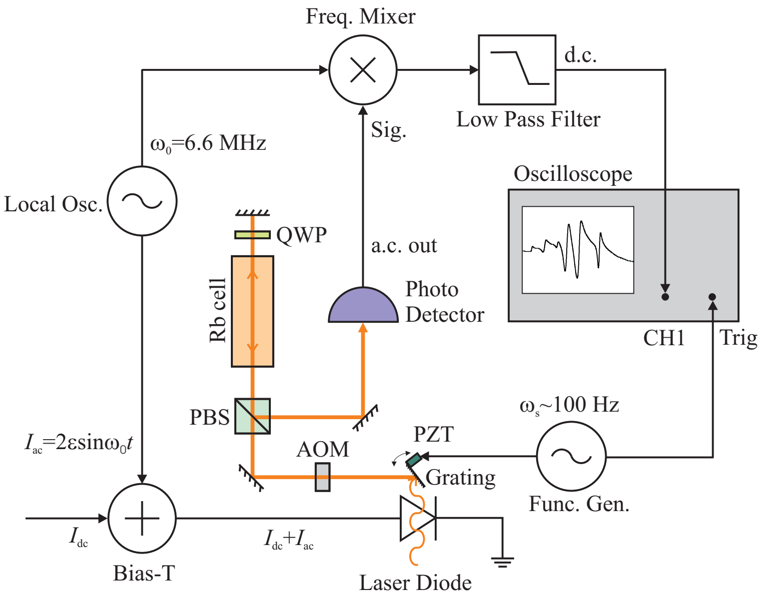

Figure 2.3: FM spectroscopy setup. This technique is necessary for the laser lock to work. FM spectrum is the 1st derivative of the saturated absorption spectrum. Therefore, locking the laser to an absorption peak is equivalent to locking the FM signal at a zero point. Here, AOM, PBS, and QWP are acousto-optic modulator, polarization beam splitter, and quarter wave plate. PZT is the piezo-electric actuator.

is -18 MHz, which is 3 atomic linewidths below resonance. To optimize loading into the CO_2 laser optical traps, the detuning is shifted to -140 MHz for sub-Doppler cooling [66].

The repump laser does not need to change frequency; it is locked to the crossover of $F = 1 \leftrightarrow F' = 2$ and $F = 1 \leftrightarrow F' = 1$ transitions and then frequency shifted to resonance with $F = 1 \leftrightarrow F' = 2$ transition using an AOM that also controls the repump power.

2.2.3 Magnetic Coils

Several sets of magnetic coils are employed to control the magnetic fields and field gradient in the experiment. The MOT coils consist of 15 turns and the power supply can produce up to 600 A, which allow us to produce gradients up to 30 G/cm. For the formation of the MOT, a field gradient of 7 G/cm is typically used. The MOT coils are also used to provide a field gradient for Stern-Gerlach experiments on the spinor condensates. This method is used to separate the different Zeeman states in order to measure the spin populations of condensates. Also, different field gradients are often applied during the evaporation to control the populations of the condensates in different Zeeman states.

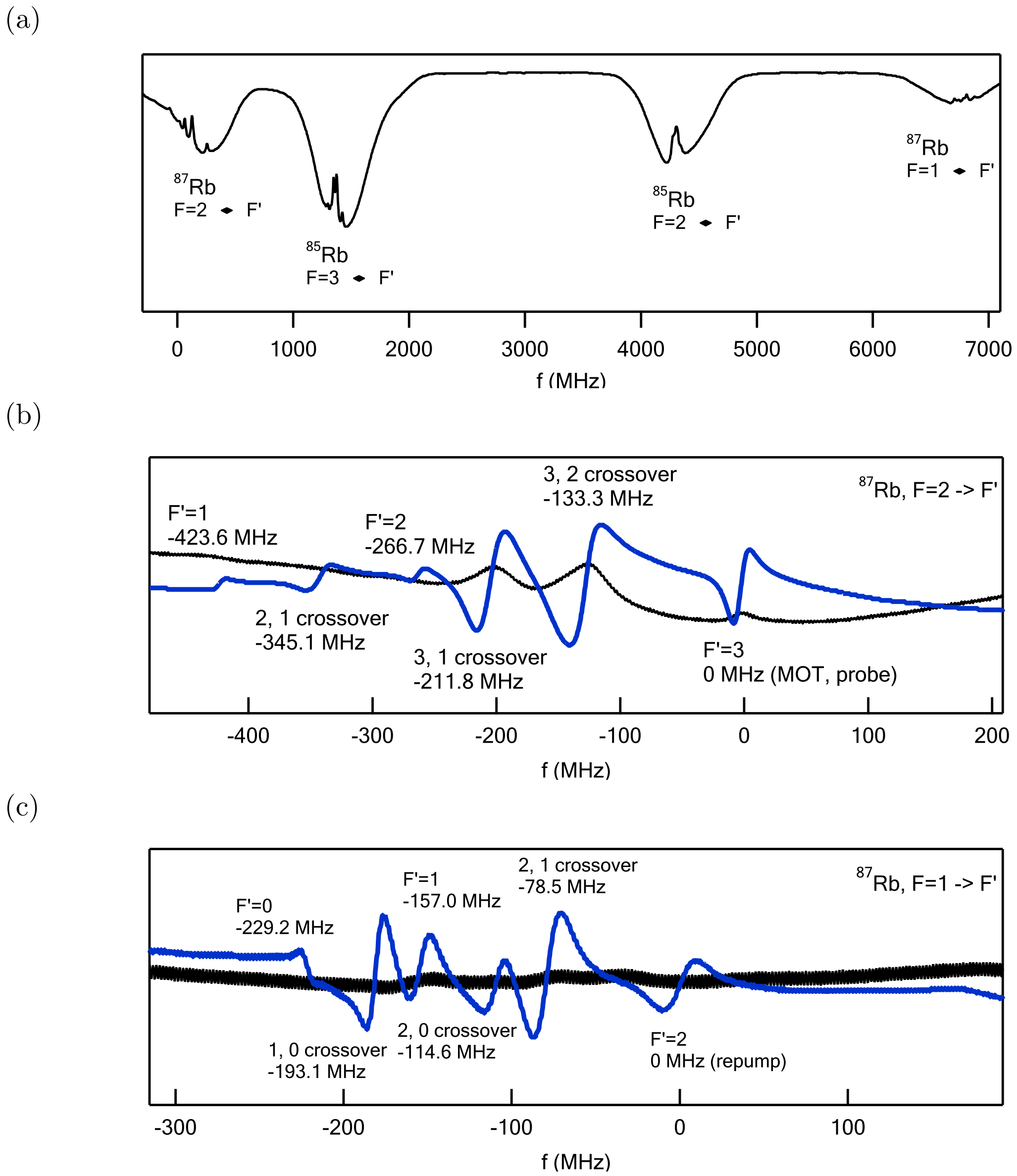

Figure 2.4: Saturated absorption spectra of D_2 transitions. (a) The spectra of D_2 transitions of ^{85}Rb and ^{87}Rb. (b) The saturated absorption and FM spectra of $F = 2 \rightarrow F'$ transitions for ^{87}Rb. (c) The saturated absorption and FM spectra of $F = 1 \rightarrow F'$ transitions for ^{87}Rb.

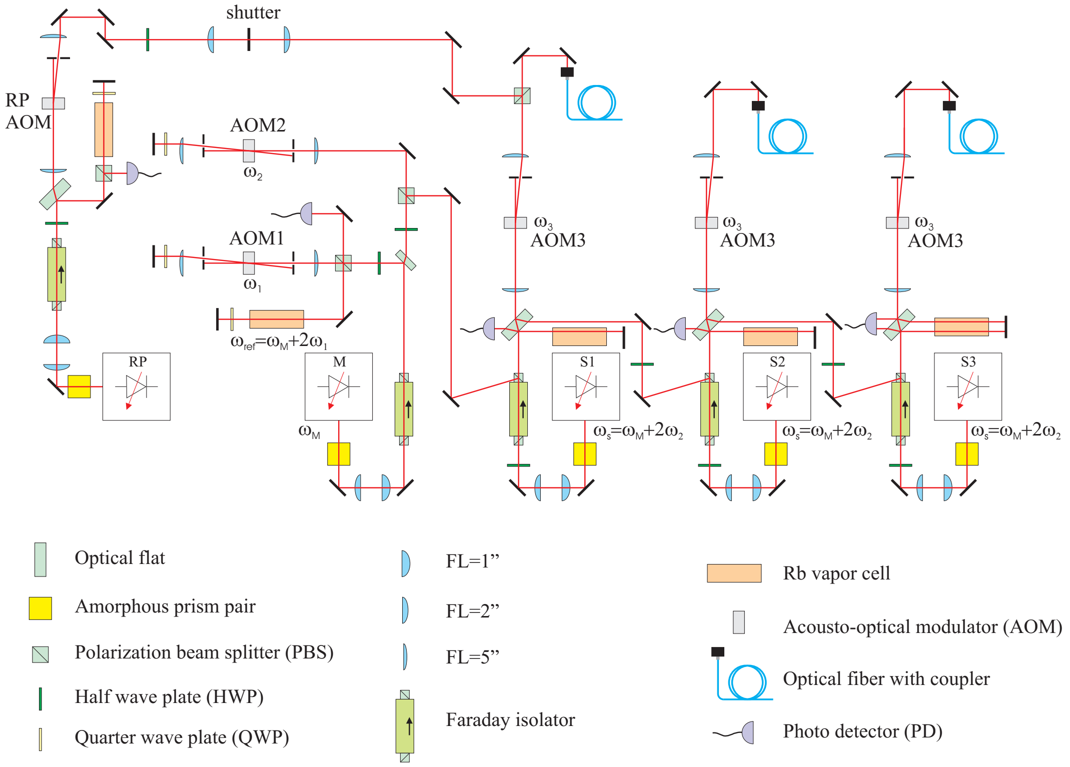

Figure 2.5: Diode laser setup.

In addition to the MOT coils, there are three orthogonal pairs of Helmholtz coils (trim coils) used to cancel the Earth's magnetic field (~ 0.5 G) and other stray magnetic fields. In addition, these coils are also used to apply magnetic fields required for studies of the spinor condensates. A pair of weaker anti-Helmholtz coils is used to add or compensate a field gradient along the horizontal trap direction, (the z direction in Fig. 2.6). This pair of anti-Helmholtz coils proved to be important in our spinor studies.

The layout of the magnetic coils (top view) is shown in Fig. 2.6. To perform controlled experiments on spinor condensates, it is desirable to have a uniform field across the condensate. However, since the coils are not all in perfect Helmholtz configuration due to the constraints of the vacuum chamber geometry, the field produced by the trim coils are not necessarily uniform. It is then necessary to know the inhomogeneity of the applied B field at the trap location. By decomposing the field into multipole fields and superimposing the contribution from different coils, the B field magnitude and gradient at the trap location can be computed.

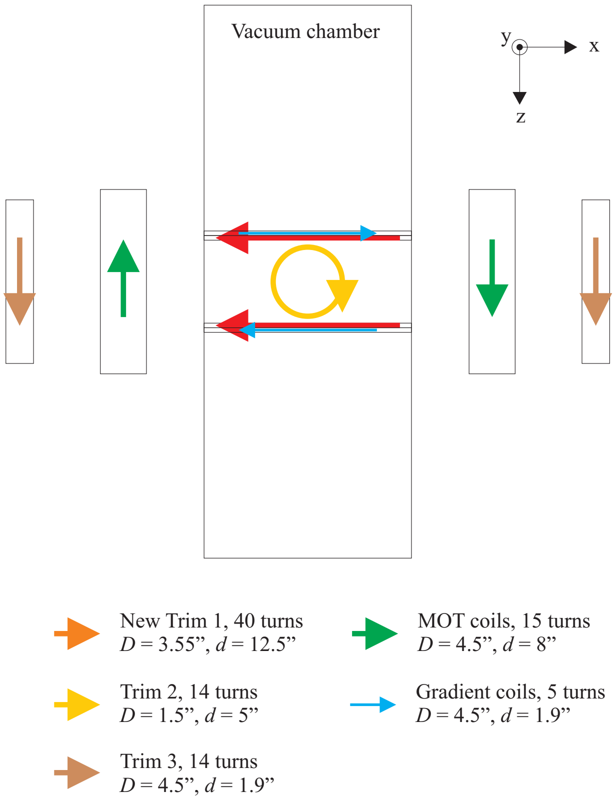

Figure 2.6: Top view of the Helmholtz (bias) and anti-Helmholtz (gradient) coils. The arrows represent the direction of the electric current of the coils. In this case, the diameter of each pair of coils is D, and separation between the two coils is d.

The multipole expansion (around the center) for a scalar magnetic potential of a circular Helmholtz coil is [67]

$$\psi(r,\theta) = -\mu_0 NI \sum_{n=odd}^{\infty} \frac{1}{n} \left(\frac{r}{a}\right)^n \sin\theta_0 P_n^1(\cos\theta_0) P_n(\cos\theta),\ r < a\ . \tag{2.2}$$

Here N and I are the number of winding turns and the electrical current, and a and θ_0 are defined in Fig. 2.7. $P_n(\cos\theta)$ are the Legendre polynomials, and $P_n^1(\cos\theta) = -\frac{\mathrm{d}}{\mathrm{d}\theta} P_n(\cos\theta)$ are the associated Legendre polynomials. The magnetic field is $B(r,\theta) = -\nabla\psi(r,\theta)$, and

$$B_r(r,\theta) = -\mu_0 NI \sum_{n=odd}^{\infty} \frac{r^{n-1}}{a^n} \sin\theta_0\, P_n^1(\cos\theta_0)\, P_n(\cos\theta)\ , \tag{2.3a}$$

$$B_\theta(r,\theta) = -\mu_0 NI \sum_{n=odd}^{\infty} \frac{1}{n} \frac{r^{n-1}}{a^n} \sin\theta_0 P_n^1(\cos\theta_0) P_n^1(\cos\theta)\ . \tag{2.3b}$$

With these expressions, together with a transformation to Cartesian coordinates, the magnetic fields and curvatures are readily found in different directions. Note that for symmetric coils, the magnetic field gradient of each pair of coils is cancelled. In our setup, the field curvature along the x direction is $B_x'' = 40$ mG/cm^2 per Gauss of field produced along x direction. Similarly, $B_y'' = 245$ and $B_z'' = 19$ mG/cm^2 for 1 G of field applied along the y, z direction, respectively. The x, y, z directions are defined in Fig. 2.6. It is noted that the Trim 2 coil has the largest field inhomogeneity (B_y'') since it is furthest from the ideal Helmholtz ($d = D/2$) geometry. Given the maximum fields we generated using different coils, and the trap position uncertainty of 1 mm with respect to the center of the coils, the estimated maximum field gradients are $B_x' \simeq B_x'' x \leq 20$ mG/cm at 1 G along x direction, $B_y' \simeq B_y'' y \leq 15$ mG/cm at 0.5 G along y direction, and $B_z' \simeq B_z'' z \leq 5$mG/cm at 0.5 G along z direction.

2.3 Vacuum Chamber and Atom Source

An ultra-high vacuum environment is required for BEC experiments in order to isolate the trapped ultracold atoms from collisions with fast room temperature atoms. The pressure in our vacuum chamber is between low 10^{-10} and high 10^{-11} torr, which results in a vacuum limited lifetime of 10 s [68]. This is sufficient for our experiments since evaporative cooling takes less than 2 s due to the fast collision dynamics in our optical traps. The lifetime

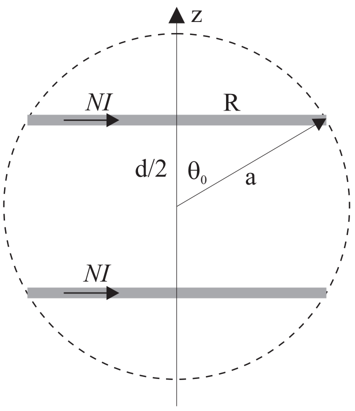

Figure 2.7: A side view of a Helmholtz coil (not necessary in perfect geometry).

of our condensates is $3 - 5$ sec, which is not limited by the vacuum but by three-body recombination loss.

We use ^{87}Rb in our BEC experiments, which is a metallic solid at room temperature. An ampule of rubidium metal is placed in a flexible bellows connected to the main chamber. This port is aligned in direct line of sight with the MOT. The vapor pressure of rubidium at room temperature is $\sim 2 \times 10^{-7}$ torr, and the vapor contains 27.8% of ^{87}Rb and 72.2% of ^{85}Rb by natural abundance. The atoms diffuse from the source to the main chamber when the valve between the two chambers is opened.

2.4 Optical Dipole Force Trap

Optical dipole force traps are important tools in our BEC experiments. The laser cooled atoms are loaded into the optical trap from which we perform forced evaporation to achieve quantum degeneracy. Optical traps offer higher restoring forces than typical magnetic traps, which leads to higher atomic density for efficient evaporation. Optical trapping of neutral atoms was first observed in 1986 [69], and evaporative cooling in a crossed optical trap was first demonstrated in 1994 [70].

The optical dipole force comes from the dispersive interaction of the intensity gradient of the light field with the atomic dipole moment which is induced by the optical field. The dipole moment induced by the field is given by $\vec{p} = \alpha \vec{E}$, where α is the complex frequency dependent atomic polarizability. The interaction potential of the induced dipole moment in the driving field is given by

$$U = -\langle \int \vec{p} \cdot \mathrm{d}\vec{E} \rangle = -\frac{1}{2}\langle \vec{p} \cdot \vec{E} \rangle = -\frac{1}{2\epsilon_0 c}\mathrm{Re}(\alpha) I, \tag{2.4}$$

where I is the light intensity. Here the angular brackets represent a time average over the oscillation period of the driving optical field. The averaged optical power dissipated by the atoms is given by

$$P_{\mathrm{abs}} = \langle \dot{\vec{p}} \cdot \vec{E} \rangle = \frac{\omega}{\epsilon_0 c}\mathrm{Im}(\alpha) I. \tag{2.5}$$

where ω is the angular frequency of the light field. The corresponding photon scattering rate is

$$\Gamma_{\mathrm{sc}} = \frac{P_{\mathrm{abs}}}{\hbar\omega}. \tag{2.6}$$

The polarizability α can be estimated using a simple Lorentz model, $\ddot{x} + \Gamma_\omega \dot{x} + \omega_0^2 = -\frac{e}{m}E(t)$, where the classical damping rate Γ_ω is due to radiative energy loss and is given by the Larmor formula, $\Gamma_\omega = \mathrm{e}^2\omega^2/6\pi\epsilon_0 m_e c^3$. Solving the equation of motion, the polarizability is found as

$$\alpha = 6\pi\epsilon_0 c^3 \frac{\Gamma/\omega_0^2}{\omega_0^2 - \omega^2 - i(\omega^3/\omega_0^2)\Gamma}. \tag{2.7}$$

Here Γ_ω is replaced with the on-resonance damping rate Γ with $\Gamma_\omega = (\omega_0/\omega)^2\Gamma$. The on-resonance damping rate can also be determined by the dipole transition in the semi-classical model, in which an atom is treated quantum mechanically, while the driving optical field is treated classically. Then the damping rate is given as

$$\Gamma = \frac{\omega_0^3}{3\pi\epsilon_0 \hbar c^3}|\langle e|p|g\rangle|^2, \tag{2.8}$$

where $\langle e|p|g\rangle$ is the dipole transition matrix element.

When the detuning is large and saturation effects can be neglected, the trapping potential and scattering rate can be approximated as

$$U(r) = -\frac{3\pi c^2}{2\omega_0^3}\left(\frac{\Gamma}{\omega_0 - \omega} + \frac{\Gamma}{\omega_0 + \omega}\right) I(r), \tag{2.9}$$

$$\Gamma_{\mathrm{sc}}(r) = \frac{3\pi c^2}{2\hbar\omega_0^3}(\frac{\omega}{\omega_0})^3 \left(\frac{\Gamma}{\omega_0 - \omega} + \frac{\Gamma}{\omega_0 + \omega}\right)^2 I(r). \tag{2.10}$$

In a case of a typical far-off resonance trap (FORT), in which the detuning $|\Delta| = |\omega - \omega_0| \ll \omega_0$, Eq. (2.9) and (2.10) can be further reduced to

$$U(r) = -\frac{3\pi c^2}{2\omega_0^3}\frac{\Gamma}{\Delta}I(r), \tag{2.11}$$

$$\Gamma_{\text{sc}} = \frac{3\pi c^2}{2\hbar\omega_0^3}\left(\frac{\Gamma}{\Delta}\right)^2 I(r) = \frac{\Gamma}{\hbar\Delta}U(r). \tag{2.12}$$

It is easily seen while keeping the same trap depth, the scattering rate can be greatly reduced by increasing the detuning. In an extreme case where $\omega \ll \omega_0$, such as the case of CO_2 laser, the condition $|\Delta| \ll \omega_0$ no longer holds. Eq. (2.9) and (2.10) should be reduced to

$$U(r) \simeq -\frac{3\pi c^2 \Gamma}{\omega_0^4}I(r) = -\frac{\alpha_s}{2\epsilon_0 c}I(r), \tag{2.13}$$

$$\Gamma_{\text{sc}} = \frac{2\Gamma}{\hbar\omega_0}\left(\frac{\omega}{\omega_0}\right)^3 U(r). \tag{2.14}$$

Here α_s is the static polarizability. In this case, the optical trap is a quasi electrostatic trap (QUEST) [71], and the scattering rate is reduced so much that it is essentially a conservative trap. Take for example, a typical trap depth of 100 μK for a CO_2 laser dipole force trap, the scattering rate is only 1.1 photon per atom per hour for ^{87}Rb! A more detail descussion of optical dipole traps can be found in ref. [72].

The dipole force trapping beams are generated from two CO_2 gas lasers (Synrad 48-1 and DEOS LC-100NV), with wavelength, $\lambda = 10.6$ μm. The beams are tightly focused with $f = 38$ mm focal length, ZeSn aspherical lenses inside the chamber. There are six lenses inside the chamber forming three orthogonal 1:1 telescopes that allow us to create a wide range of travelling wave and standing wave configurations including a 6 beam 3-D optical lattice. For the condensate work, two crossed lasers either in travelling wave or optical lattice configurations are used, intersected at right angles; one beam is oriented in the horizontal direction and one beam is inclined at 45° from the vertical direction. Each beam passes through a germanium AOM to provide independent control of the power in the two beams. Additionally, the beams are frequency shifted 80 MHz relative to each other so that any spatial interference patterns between the two beams are time-averaged to zero [73]. The layout of our CO_2 laser beams are provided in Fig. 2.8, and the radio frequency (RF) source for each AOM is given in Fig. 2.9.

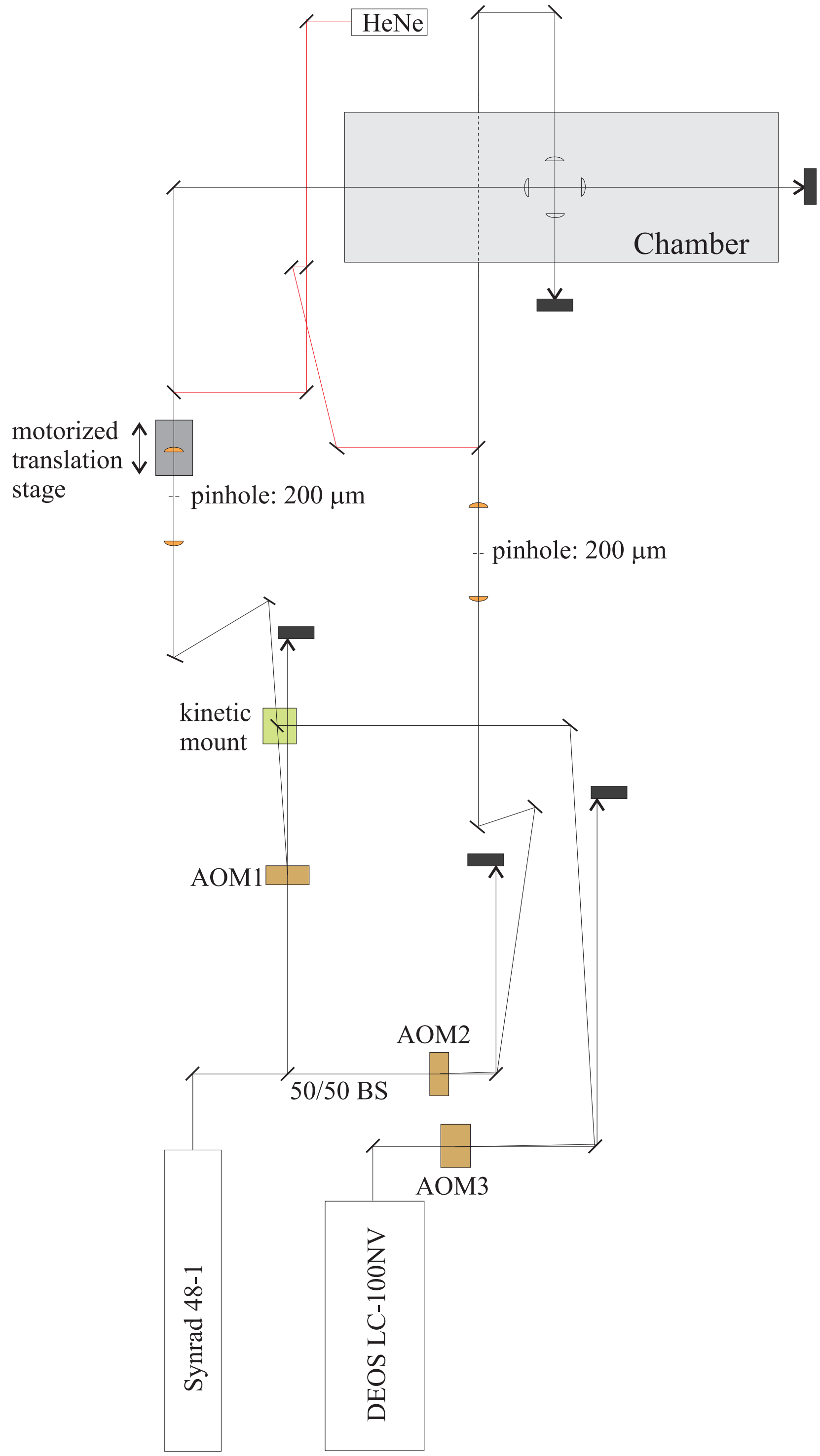

Figure 2.8: Setup of our CO_2 dipole force trap. The pinholes shown here are optional. The model number of AOM1 and AOM2 is Isomet 1207B-6, and that of AOM3 is IntraAction AGM-4010BJ1. Additionally, the model number of the motorized translation stage and its controller are Newport UTM50PP1HL and ESP300, respectively.

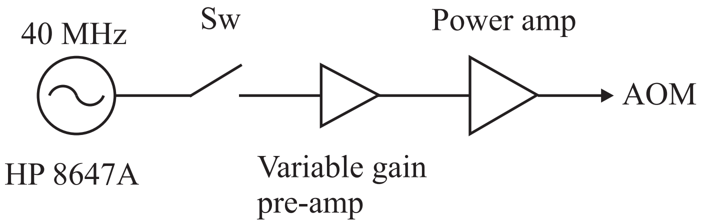

Figure 2.9: RF source for the germanium acousto-optical modulator (AOM). The CO_2 laser power is changed by varying the gain of the pre-amp. The model number of the switch, variable gain amplifier, and the RF power amplifier are Mini-Circuits ZYSWA-2-50DR, ZFL-1000GH, and Isomet RFA-1150, respectively.

2.4.1 Optical Trap Parameters

The spatial mode of our CO_2 laser is approximately TEM_{00} gaussian. The transverse intensity of a focused Gaussian beam is expressed as

$$I(x,y,z) = \frac{2P}{\pi w(z)^2} \exp\left[-2\frac{x^2+y^2}{w(z)^2}\right], \tag{2.15}$$

where

$$w(z) = w_0\sqrt{1+(\frac{z}{z_r})^2}. \tag{2.16}$$

Here P is the laser power, $z_r = \pi w_0^2/\lambda$ is the Rayleigh range, w_0 is the beam waist, and λ is the wavelength of the laser. The corresponding trap potential is then

$$\begin{aligned} U(x,y,z) &= \frac{\alpha}{2}|E(x,y,z)|^2 && (2.17a)\\ &= \frac{\alpha}{2}\frac{I(x,y,z)}{c\epsilon_0} && (2.17b)\\ &= \frac{1}{4\pi\epsilon_0}\frac{4\alpha P}{cw(z)^2}\exp\left[-2\frac{x^2+y^2}{w(z)^2}\right] && (2.17c)\\ &= U_0\exp\left[-2\frac{x^2+y^2}{w(z)^2}\right], && (2.17d) \end{aligned}$$

Here α is the polarizability, and for ^{87}Rb ground states, $\alpha = 5.3\times10^{-39}\ \mathrm{m}^2\frac{\mathrm{C}}{\mathrm{V}}$. The trap depth is given by

$$U_0 = \frac{1}{4\pi\epsilon_0}\frac{4\alpha}{c\,w_0^2}P. \tag{2.18}$$

When the temperature of the trapped cloud is much lower than the trap depth the trapping potential can be approximated with a simple harmonic oscillator. The trap frequencies

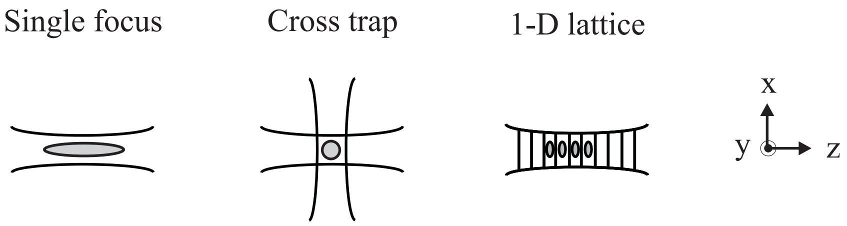

Figure 2.10: Three trap geometries.

Table 2.1: Table of trap frequencies. Here $w(z) = w_0\sqrt{1+(\frac{z}{z_r})^2}$, $z_r = \pi w_0^2/\lambda$, $k = 2\pi/\lambda$, and $U_0 = \frac{1}{4\pi\epsilon_0}\frac{4\alpha}{cw_0^2}P$, where P is the power per beam. We assume that the laser beams have the same circular Gaussian profile and the same power.

Trap Parameters	Single focus	Cross trap	1D lattice
Potential	$\frac{U_0}{1+(\frac{z}{z_r})^2}\mathrm{e}^{-\frac{2r^2}{w(z)^2}}$	$\frac{U_0}{1+(\frac{z}{z_r})^2}\mathrm{e}^{-\frac{2(x^2+y^2)}{w(z)^2}}$ $+\frac{U_0}{1+(\frac{x}{z_r})^2}\mathrm{e}^{-\frac{2(y^2+z^2)}{w(x)^2}}$	$\frac{4U_0}{1+(\frac{z}{z_r})^2}\mathrm{e}^{-\frac{2r^2}{w(z)^2}}\cos^2 kz$
Trap Depth	U_0	$2U_0$	$4U_0$
Low Frequency (ω_L)	$\sqrt{\frac{2U_0}{mz_r^2}}$	$\sqrt{\frac{4U_0}{mw_0^2}}$	$\sqrt{\frac{16U_0}{mw_0^2}}$
High Frequency (ω_H)	$\sqrt{\frac{4U_0}{mw_0^2}}$	$\sqrt{\frac{8U_0}{mw_0^2}}$	$\sqrt{\frac{8U_0k^2}{m}}$
Mean Frequency ($\bar{\omega}$)	$(\omega_L^2\omega_H)^{1/3}$	$(\omega_L^2\omega_H)^{1/3}$	$(\omega_L^2\omega_H)^{1/3}$
Aspect Ratio (ω_H/ω_L)	$\frac{\sqrt{2}\pi w_0}{\lambda}$	$\sqrt{2}$	$\frac{\sqrt{2}\pi w_0}{\lambda}$

can be measured using parametric resonance method, and they can be easily computed using

$$\omega_{r_i} = \left[\frac{-1}{m}\frac{\partial^2 U(x,y,z)}{\partial r_i^2}\right]^{1/2}_{(x,y,z)=(0,0,0)}, \tag{2.19}$$

where $r_i = x, y, z$, and m is the mass of the atom.

By superimposing more than one focused Gaussian beams, one can create optical potentials with a variety of trap geometries. In this thesis, the single focused, cross trap, and 1D lattice geometries are mainly used in the BEC experiments, and they are illustrated in Fig. 2.10. Some useful trap parameters for these traps are listed in Table 2.1 for reference.

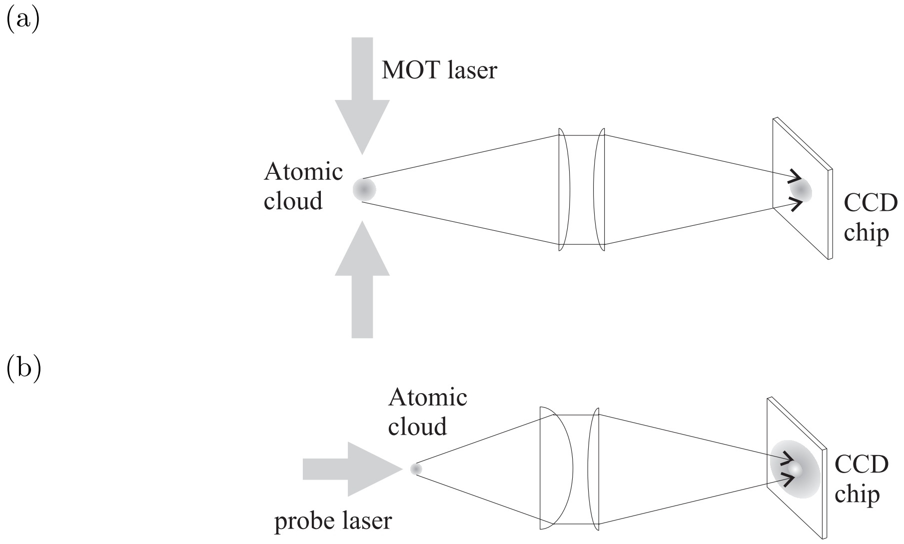

Figure 2.11: Schematic of probe techniques. (a) Fluorescence imaging. (b) Absorption imaging.

2.5 Atom Probe and Signal Collection

The atomic cloud is measured using either fluorescence or absorption imaging techniques. There are two imaging systems that view from the side and the top of the trap. A 1:1 imaging system is used to view from the side and the image is recorded by a surveillance charge-coupled device (CCD) camera. A 4:1 imaging system is used to view from the top using a cooled scientific CCD camera. For fluorescence probing, we pulse on all of the MOT beams at the maximum power of 35 mW/cm^2 for 100 μs, which is equivalent to a total intensity of $45I_s$, where $I_s = 1.6$ mW/cm^2 is saturation intensity. The fluorescent images are taken with both cameras. For absorption imaging, a vertical, weak probe laser beam is sent through the trapped atoms and directed through the imaging optics to the cooled CCD camera. The probe laser is pulsed on for 100 μs at an intensity of 1 mW/cm^2. For both techniques, the laser frequency and polarization are tuned to drive the $|F = 2, m_F = 2\rangle \rightarrow |F' = 3, m_F = 3\rangle$ transition. To image the atoms in the $F = 1$ state, the repump laser is also pulsed during imaging. The probe techniques are illustrated in Fig. 2.11, and the theory of imaging techniques and quantitative imaging analysis will be given in the next chapter.

2.6 Microwave Source

In addition to manipulating the atoms with laser excitation, we also use microwaves to excite transitions between the ground hyperfine states. Microwave manipulation of the atomic spin states is an important tool in the study of spinor dynamics. Microwave radiation tuned to 6.835 GHz is capable of driving transitions between the $F = 1 \leftrightarrow F = 2$ states. Additionally, we use microwave spectra to measure the magnitude and gradient of the magnetic field in situ. The microwave radiation is generated by the setup shown in Fig. 2.12. Two HP high frequency generators (HP E4422B) are phase locked to a 10 MHz oscillator referred to a signal received from GPS satellites (EndRun Technology Præcise Gfr). The output frequencies and amplitudes of the HP oscillators are set by computer commands, which can be reset every 500 ms. Their outputs are then switched by two fast switches (Mini-Circuits ZYSWA-2-50DR) and then frequency doubled (Marki Microwave D0204LA) before feeding into a preamp (Mini-Circuits ZFL-7G) followed by a 20 W power amplifier (Varian TWT VZC6961K1DFGJ). To prevent microwaves from reflecting back to the frequency dobuler and generating multiple frequencies, a microwave isolator (MIDISCO M3I0408) is inserted between the dobuler and the power combiner (Mini-Circuits ZFSC-2-10G). After the amplifiers, the microwaves are sent to a homebuild cylindrical horn and coupled into the vacuum chamber through a view port. To optimize the coupling efficiency, the diameter of the horn is set at the inner diameter (1.5 inch) of the standard vacuum nipple. From the choice of diameter (3.8 cm) and the microwave frequency (6.8 GHz), all the other dimensions can be calculated using formulas that involve zeros of the Bessel functions and zeros of the derivatives of the Bessel functions (see *e.g.*, Chapter 8 of ref. [67]). In particular, the optimized overall length of the copper antenna, the input coupler length, and the distance between the coupler and the ground reflector (end plate) are found to be 7.5 cm, 1.1 cm, and 1.5 cm, respectively.

2.7 Control Unit

Our experiment is controlled by a combination of synchronized analog and TTL signals. To provide arbitrary analog signals, we use two 8-channel PCI analog output boards (AIO,

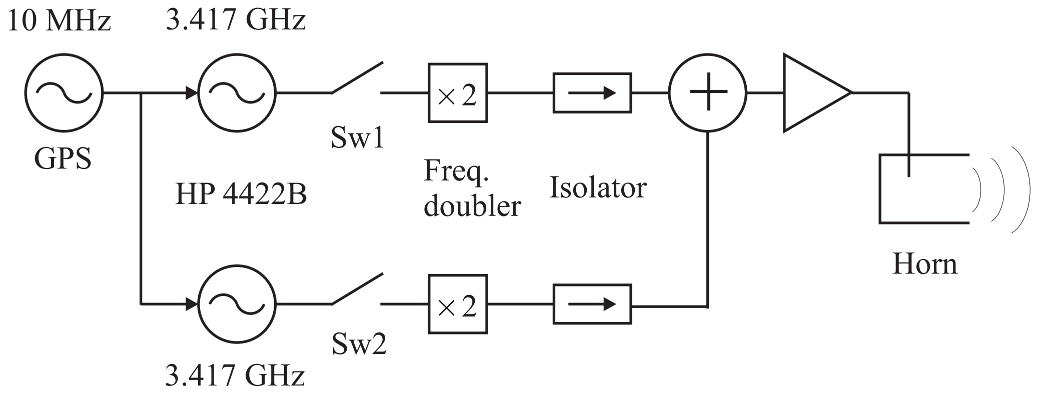

Figure 2.12: Microwave setup. The frequencies and amplitudes of two HP oscillators are set by computer commands. The two switches, Sw1 and Sw2, are controlled by two independent digital signals.

National Instrument 6713) which are controlled by LabView programs (VIs). The TTL signals are mostly generated by TTL pulse generators (SRS DG535 and BNC 500) which are triggered by AIO outputs. Recently, we have replaced most of the TTL pulse generators with a 32-channel PCI digital input/output board (DIO, model number NI-6534). For TTL pulses shorter than 100 μs, high precision pulse generators (SRS-DG535) are still employed.

CHAPTER III

DETECTION AND IMAGE ANALYSIS FOR ULTRACOLD ATOMIC CLOUDS

Trapped ultracold clouds are small, typically only 10's of microns across, and they are isolated in a ultrahigh vacuum chamber. As such, it is not feasible to interrogate the trapped atoms with material probes, such as a thermometer [1]. Laser cooling and magneto-optical trapping rely on the strong interaction of atoms with a near-resonant light. These same interactions are also used to detect atoms and measure dynamical quantities of the atom clouds.

Probing of an ultracold cloud is straightforward via measurements of the optical power radiated from or transmitted through the atomic cloud. These two types of probing techniques are referred to as fluorescence and absorption spectroscopies, respectively. Imaging the radiation on a camera allows measurement of the ensemble properties, such as the spatial and momentum distributions of the atomic cloud. Image analysis for an ultracold atomic cloud is also straightforward, since a trapped ultracold atomic cloud is a very simple and clean system such that its properties can be understood from first principles.

A trapped Bose gas at thermal equilibrium is described by a Boltzmann distribution when the temperature is much higher than the BEC critical temperature, and a Bose distribution when the temperature is close to the critical temperature. At temperatures much lower than the critical temperature, when the trapped cloud contains mostly a Bose-Einstein condensate, its ground state properties and dynamics are well-described by the nonlinear Schrödinger equation, or Gross-Pitaevskii equation.

In this chapter, we present the techniques employed to determine the atomic properties from measured images of the atom clouds. In addition, we present how to extract physical

---

[1] While material probes such as a multichannel plate can be used to detect atoms [74], optical probes are generally simpler and more versatile.

quantities from the acquired images, and how one can derive other physical quantities from these measurements using simple statistical mechanics formula.

3.1 Measurement Techniques for Ultracold Atoms

The atomic clouds are measured using both fluorescence and absorption imaging techniques. The images are recorded with charge-coupled device (CCD) cameras and then downloaded to the computer for subsequent quantitative analysis.

3.1.1 Fluorescence Imaging

Probing ^{87}Rb atoms is relatively easy due to strength of the cycling transition. In addition, it is straightforward to interpret and calibrate the fluorescence signals using a two-level atom model. The photon scattering rate for a two-level atom is given by

$$\gamma_p = \frac{\gamma}{2} \frac{s_0}{1 + s_0 + (2\Delta/\gamma)^2}, \tag{3.1}$$

where s_0, γ, and Δ are the saturation parameter, spontaneous decay rate, and the laser detuning from resonance. Here $\Delta = \omega_L - \omega_0 - \vec{k} \cdot \vec{v}$, where ω_L and ω_0 are the laser and atomic transition frequencies, and $\vec{k}$ and $\vec{v}$ are the wavevector of the laser and the velocity of the atom. The term $\vec{k} \cdot \vec{v}$ represents the Doppler shift; for ultracold atoms, this shift is much smaller than the atomic transition linewidth, and thus can be neglected. The saturation parameter is defined as

$$s_0 \equiv I/I_{\text{sat}}, \tag{3.2}$$

where I and I_{sat} are the laser intensity and the saturation intensity with

$$I_{\text{sat}} \equiv \frac{\gamma}{2} \frac{hc}{\lambda} \frac{1}{\sigma_{eg}}. \tag{3.3}$$

Here λ is the atomic transition wavelength, and $\sigma_{eg} = 3\lambda^2/2\pi$ is the on-resonance absorption cross section. The numerical values of these quantities for ^{87}Rb are listed in the Table A.1. The maximum scattering rate for ^{87}Rb cycling transition is $\gamma/2 = \pi \cdot 5.8 \times 10^6$ s^{-1}.

Fluorescence signals come from the resonantly scattered photons. To maximize the strength of the fluorescent signal, laser beams with high saturation parameter are typically used, and this unavoidably heats the atoms. Assuming that the photons are scattered in random directions and each photon imparts a momentum recoil of v_{rec} to the atom, then the total recoil velocity given to an atom is $\sqrt{N_p/3}\, v_{rec}$, where N_p is the number of photon scattered, and $v_{rec} = h/\lambda m$ is the photon recoil velocity. For ^{87}Rb $v_{rec} = 5.8$ mm/s [57]. This probe-induced recoil velocity will blur the images, with a random displacement of the probed atoms of $\sqrt{N_p/3}\, v_{rec}\, \tau$, where τ is the probe time. Given a typical fluorescent probe time of 100 μs in our experiment, this results in a blurring of 15 μm. Moreover, without perfectly balancing the intensities of the probe beams (MOT lasers in our case), the fluorescence will also cause significant cloud movement and distortion due to radiation pressure imbalance. A further limitation of fluorescence imaging is that only a small number of the scattered photons are detected due to the small collection solid angle [2]. As the number of the atoms decreases the signal will quickly give way to background scattering light and detector noise. Due to these technical drawbacks, fluorescence imaging is only used to diagnose the MOT or the trap loading in our experiments.

In the regime where the optical density (OD) of the atom cloud is 0.1-2, we can conveniently probe atom clouds with an absorption imaging technique.

3.1.2 Absorption Imaging

Absorption imaging for trapped atoms works best when the probe intensity is weak (less than the saturation intensity) and the optical density of the atomic cloud is thin (OD $\leq$ 1) so that the absorption of light is independent of the probe intensity and is linearly proportional to the cloud density. Suppose that a weak laser beam propagates along the z axis and passes through a cloud. Its intensity decreases according to the Lambert-Beer's law (see *e.g.*, [75])

$$\frac{\mathrm{d}I(x,y,z)}{\mathrm{d}z} = -n(x,y,z)\sigma_{eg} I(x,y,z),$$

where n and σ_{eg} are the cloud density and the absorption cross section. The probe beam intensity profile after propagation through the cloud is given by

$$I(x,y) = I_0(x,y)\exp[-\tilde{n}\sigma_{eg}],$$

---

[2] For a simple imaging system, the solid angle $\Omega = r^2/4d^2$, where r is the radius of the imaging lens, and d is the distance between lens and the cloud. In our case, $\Omega = 1/250$.

where $\tilde{n} = \int n(x, y, z)\mathrm{d}z$ is the column density. The optical density of the cloud at the location (x, y) is

$$\sigma_{eg}\tilde{n}(x, y) = -\ln T(x, y), \tag{3.4}$$

where $T(x, y)$ is the relative transmission of the beam. The relative transmission can be measured by comparing the laser beam profiles measured with and without the presence of atoms. Referring to the measured profiles in the above two conditions as the signal and reference images and denoting them as $S(x, y)$ and $S_0(x, y)$, respectively, the relative transmission is simply $T(x, y) = S(x, y)/S_0(x, y)$. Probe laser profiles are generally recorded by a CCD camera, and one needs to take a third background image, $S_b(x, y)$, with no probe beam, and then subtract this background from the signal and the reference images. This way, contamination from stray scattering light, and any background added by the camera electronics can be eliminated. Therefore, in practice the recorded optical density is given by

$$\sigma_{eg}\tilde{n}(x, y) = -\ln \frac{S(x, y) - S_b(x, y)}{S_0(x, y) - S_b(x, y)} = -\ln T(x, y). \tag{3.5}$$

The advantage of this technique is that, since the absorption imaging measures the relative transmission of the laser beam with and without the presence of atoms, distortion of laser beam profiles due to imperfect imaging optics and other factors such as the camera efficiency are cancelled out in the calculation. In addition, the probe laser beam is directed onto the camera CCD chip, and usually its beam size is small compared to the clear aperture of the imaging optics. Therefore, the solid angle is irrelevant, and ideally the probe power can be completely collected.

There are disadvantages in this imaging technique however. First, there are potential diffractive errors for small clouds. Secondly, the absorption imaging is not background free and it works best for optical density 0.1 - 1. The sensitivity of the method is limited by the accuracy to which the relative transmission can be determined. Although this is fundamentally limited by the shot-noise limited signal to noise ratio of the probe beam, in practice it is limited by shot-to-shot variations in the probe beam intensity profile and strength.

3.2 Measurements for Ultracold Gases

The properties of trapped dilute gases are determined by ultracold collisions in the trap, and, in thermal equilibrium, the cloud will obey classical or quantum statistics depending on the temperature regime. Using the kinetic theory of an ideal or weakly interacting gas and only a few measured atomic parameters and physical quantities, the dynamics of the ultracold cloud can be well characterized and understood. To characterize ultracold clouds, it is only necessary to know the atomic s-wave scattering length, and physical quantities such as the number of atoms, temperature, and the trap frequencies, which can be extracted directly from the images of the atomic clouds. Other relevant dynamical variables can then be computed based on these three quantities.

As mentioned in the last two sections, an atomic cloud can be probed with fluorescence or absorption techniques. The cloud can be either probed in-situ or after released from the trap for few milliseconds of time of flight (TOF). The TOF method is important for imaging a cloud that is spatially too small to resolve optically or too dense to measure quantitatively. Additionally, the TOF method is useful for measuring the momentum distribution of the cloud, which can be used to determined temperature.

Number of Atoms The first important measurement in an ultracold atomic experiment is measuring the number of atoms in the trap. For fluorescence imaging with probe laser intensity, I, collection solid angle, Ω, the quantum efficiency of the CCD chip, η, and the electron to camera count conversion rate, κ [3], the total number of the atoms is

$$N = \frac{\kappa}{\gamma_p \tau \Omega \eta} \sum_{\mathrm{pix}} n_{\mathrm{pix}}, \tag{3.6}$$

where n_{pix}, γ_p, and τ are the number of camera counts stored in a CCD pixel, the photon scattering rate as defined in Eq. 3.1, and the probe time respectively.

When a cloud is probed absorptively, the number of atoms is given by

$$N = \int \tilde{n}(x,y)\mathrm{d}x\mathrm{d}y = -\frac{A_{\mathrm{pix}}}{\sigma_{eg}} \sum_{\mathrm{pix}} \ln T_{\mathrm{pix}}, \tag{3.7}$$

---

[3] The quantum efficiency of our cooled CCD camera is $\eta \sim 50\%$ at 780 nm, and the conversion rate is $\kappa \sim 10$ electrons per camera count.

where A_{pix} is the area of each pixel, σ_{eg} is the absorption cross section of the cycling transition, and T_{pix} is the transmission profile defined in the last section.

Temperature The temperature of the gas can be determined by measuring the momentum distribution of the cloud. When a thermal gas is released from the trap, the momentum distribution of the atoms will be converted to a spatial density distribution. For a gas far from the quantum degenerate regime, the momentum distribution will have an isotropic gaussian form due to the equipartition theorem [76]. For an expanded cloud that is much larger than the initial trap size, the measured cloud will provide an accurate determination of the momentum distribution. Then the temperature can be extracted from the width of this Gaussian distribution. Fig. 3.1.a illustrates the time-of-flight images of thermal clouds.

By collapsing a cloud image to a 1D density profile as shown in Fig. 3.1.b, the Gaussian waist can be found as $\sigma = FWHM/(2\sqrt{2\ln 2})$, where FWHM is the full width at half maximum. With this measured Gaussian waist, the temperature can be readily found as

$$T = \frac{m}{k_{\text{B}}}(\frac{\sigma}{t})^2. \tag{3.8}$$

Here, m is the mass of a ^{87}Rb atom, k_{B} is the Boltzmann constant, and t is the free expansion time of the cloud after it is released from the trap. If the initial size of the trapped cloud is too large to be neglected, the cloud temperature can be determined by two images with different drop times;

$$T = \frac{m}{k_{\text{B}}}\left(\frac{\sigma_2^2 - \sigma_1^2}{t_2^2 - t_1^2}\right). \tag{3.9}$$

Here, $\sigma_{1,2}$ are the Gaussian waist at drop time $t_{1,2}$. From Fig. 3.2, it is clear that Eq. 3.9 is a better algorithm for computing the temperature. In addition, one can also measure the cloud size for various drop times, and then fit the cloud expansion rate with a quadratic equation: $\sigma^2 = \sigma_0^2 + \frac{k_{\text{B}}T}{m}t^2$. This way, one can not only find the temperature, T, but also σ_0, which is the cloud waist at $t = 0$.

Trap Frequencies Trap frequencies are measured using a parametric resonance technique [77]. The governing equation for parametric resonance for a parametrically driven

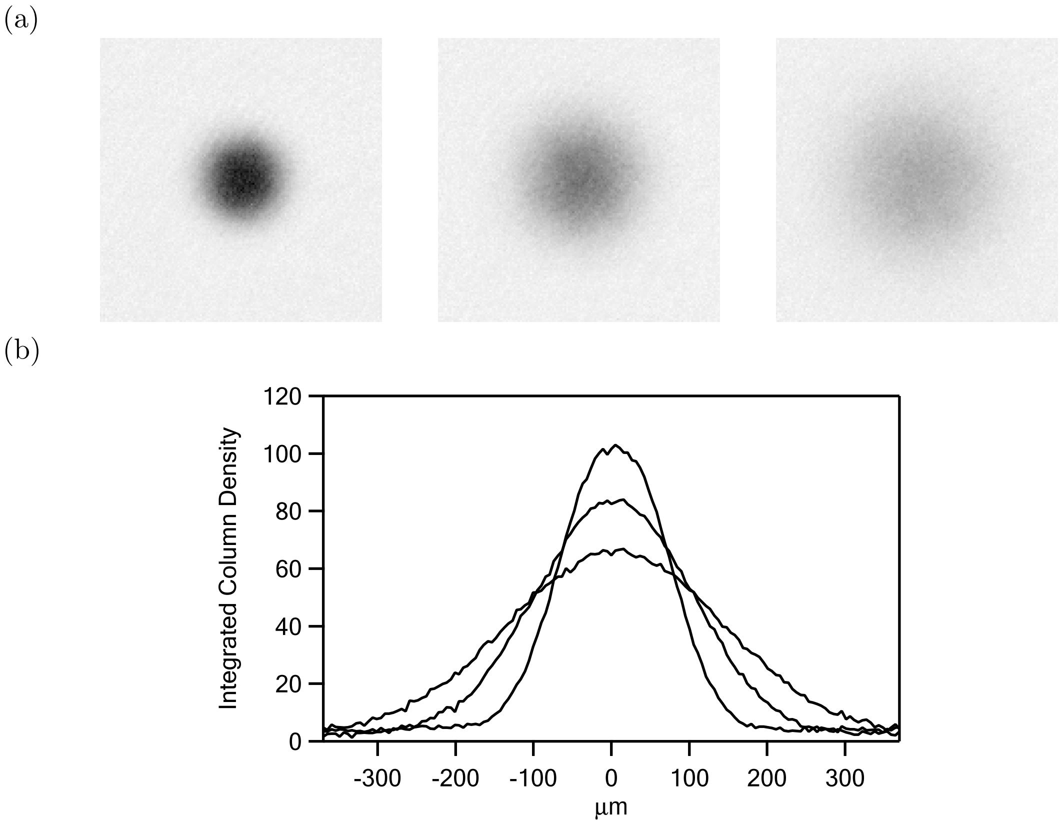

Figure 3.1: Time of flight image of atomic clouds. (a) Absorption images for drop time 2, 3.4, and 4.8 ms from left to right. Here, temperature of the clouds is ~ 2 μK. (b) By integrating the cloud image over the vertical direction, one can obtain a collapsed optical density profile. The three profiles in this plot are the collapsed optical densities for the three images in (a). The size of the clouds can be found by fitting a gaussian distribution to these profiles.

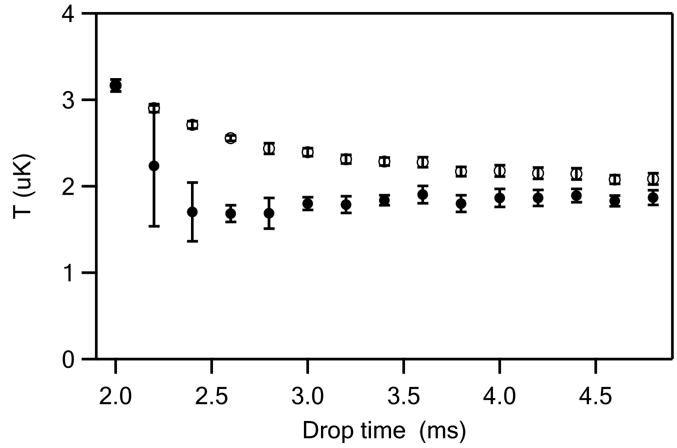

Figure 3.2: A typical temperature measurement. Open circles represent temperatures calculated using Eq. (3.8), and solid circles are the temperatures obtained using Eq. (3.9).

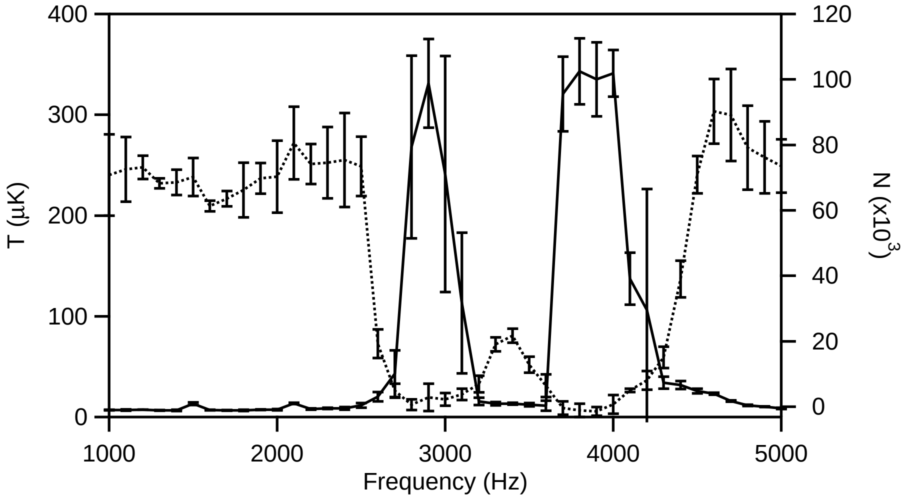

Figure 3.3: Trap frequency measurement by parametric resonance. The cloud is weakly heated at trap frequencies, and are severely heated at twice the trap frequencies. Here the solid line is the temperature, and the dotted line is the number of atoms.

harmonic oscillator is

$$\ddot{x} = \omega^2(1 + \varepsilon \sin \Omega t)x \ , \tag{3.10}$$

where ω is the trap frequency, and ε and Ω are the modulation amplitude and frequency. When the modulation frequency equals $2\omega/n$, where n is an integer, the energy of the oscillator grows exponentially [78]. We can employ this idea to excite/heat the atoms in the trap. The trap frequencies can be modulated by modulating the trap depth, since $\omega \propto \sqrt{U}$, and to modulate the trap depth, we simply modulate the CO_2 laser power. When the cloud is parametrically excited, especially at 2ω, atoms are strongly heated and boiled away. By measuring the temperature and/or the number of atoms left in the trap vs. modulation frequency, one can then determine the trap frequencies. Fig. 3.3 shows typical results of trap frequency measurements. In this particular case, the CO_2 power is ramped down after trap loading to evaporatively cool the cloud to few μK, which is low but still above the BEC critical temperature. Then the CO_2 power is adiabatically ramped back up to 5 W to compress the trap, and immediately amplitude modulated with 10% modulation for 0.5 s. The cloud is then released to measure the temperature and the total number of atoms. As shown in the plot, when the modulation frequency hits twice the trap frequency, the cloud is severely heated.

Density of a Trapped Thermal Cloud We can determine the trapped cloud density from the measured number of atoms, the temperature, and the mean trap frequency. We begin by approximating the optical trap potential to a harmonic potential. The total number, N, and the peak density of the cloud are related as

$$N = \int n_0 \, \mathrm{e}^{-\frac{m\bar{\omega}r^2}{2k_\mathrm{B}T}} \mathrm{d}^3r = n_0(\frac{2\pi k_\mathrm{B}T}{m\bar{\omega}^2})^{3/2}, \tag{3.11}$$

where T, m, and $\bar{\omega}$ are the temperature, mass of ^{87}Rb, and mean trap frequency, $\bar{\omega} = (\omega_x\omega_y\omega_z)^{1/3}$. Solving for the peak density, we find

$$n_0 = N(\frac{m\bar{\omega}^2}{2\pi k_\mathrm{B}T})^{3/2}. \tag{3.12}$$

Collision Rates Ultracold collisions play a major role in determining the properties of the Bose-Einstein condensates. Elastic collisions in trapped gas are also essential for establishing equilibrium and are necessary for evaporative cooling. Efficient evaporative cooling requires that elastic collisions dominate inelastic or other non-evaporative trap loss collisions such as three-body recombination or collisions between the trapped cloud and the residual background gas. In general, higher elastic collision rates will allow faster and more efficient evaporation.

In a thermal cloud, the mean thermal velocity is $\bar{v} = \sqrt{\frac{8k_\mathrm{B}T}{\pi m}}$, and the average relative velocity of two particles is $\bar{v}_\mathrm{rel} = \sqrt{2}\bar{v}$. For low energy collisions, the collision cross section is simply $\sigma_\mathrm{sc} = 2 \times \pi \ (2a)^2$, where a is the s-wave scattering length, and the factor of 2 comes from the indistinguishability of two identical bosons. The two-body elastic collision rate is given by

$$\gamma_\mathrm{el} = n_0 \, \sigma_{sc} \, \bar{v}_{rel} = N(8\sqrt{2}\frac{a^2m}{\pi k_\mathrm{B}})\frac{\bar{\omega}^3}{T}. \tag{3.13}$$

While discussions on ultracold collisions in this thesis and in the majority of the community focus on two-body (elastic) collisions, three-body inelastic collisions become non-negligible when the cloud density is $> 10^{14}$ cm^{-3} and result in trap loss. The three-body collision (loss) rate can be calculated as

$$\gamma_\mathrm{3B} = \Gamma_\mathrm{3B} \int n^3(\vec{r})\mathrm{d}^3r. \tag{3.14}$$

At temperatures much higher than the BEC critical temperature, the cloud density is given by Eq. 3.11, and the three-body collision rate is

$$\gamma_{3\mathrm{B}} = \Gamma_{3\mathrm{B}}^{\mathrm{nc}} \frac{n_0^2 N}{\sqrt{27}}. \tag{3.15}$$

For a condensate with a Thomas-Fermi wavefunction, which is given by Eq. 3.29 in the next section, the three-body collision rate is found to be

$$\gamma_{3\mathrm{B}} = \Gamma_{3\mathrm{B}}^{\mathrm{c}} \frac{8\, n_0^2 N}{21}. \tag{3.16}$$

Here, n_0 is the peak cloud density, and the rate constants for ^{87}Rb thermal clouds and condensates are $\Gamma_{3\mathrm{B}}^{\mathrm{nc}} = 4.3(1.8)\times 10^{-29}$ cm^6/s, and $\Gamma_{3\mathrm{B}}^{\mathrm{c}} = 5.8(1.9)\times 10^{-30}$ cm^6/s, respectively [18]. It is noted that $\Gamma_{3\mathrm{B}}^{\mathrm{nc}}/\Gamma_{3\mathrm{B}}^{\mathrm{c}} \simeq 3!$ due to the higher order coherence in the condensate [18].

Phase Space Density The phase space density, Λ, characterizes the number of atoms occupying a single quantum state, and the onset of quantum degeneracy requires $\Lambda \sim 1$. This important quantity is defined as the particle density in the joint coordinate and momentum space, and the peak phase space density for a trapped gas is given by

$$\Lambda_0 \equiv n_0 \lambda_{\mathrm{dB}}^3, \tag{3.17}$$

where n_0 is the peak spatial density, and $\lambda_{\mathrm{dB}} = h/\sqrt{2\pi m k_{\mathrm{B}} T}$ is the thermal de Broglie wavelength. When the temperature is much higher than the BEC critical temperature such that $\Lambda_0 \ll 1$, the Bose distribution can be approximated by the Boltzmann distribution, and Λ_0 is related to the total number of atoms via the integral:

$$N = \frac{\Lambda_0}{h^3} \int \mathrm{e}^{-\frac{m\bar{\omega}^2}{2k_{\mathrm{B}}T} r^2} \mathrm{e}^{-\frac{p^2}{2mk_{\mathrm{B}}T}} \mathrm{d}^3 r \mathrm{d}^3 p = \Lambda_0 \left(\frac{k_{\mathrm{B}}T}{\hbar\bar{\omega}}\right)^3.$$

Therefore,

$$\Lambda_0 = N \left(\frac{\hbar\bar{\omega}}{k_{\mathrm{B}}T}\right)^3. \tag{3.18}$$

Although this expression is an approximation, it is very useful for estimating the efficiency of evaporative cooling in real time, and it can be used as the figure of merit for tailoring and optimizing the evaporation trajectory.

3.3 Image Analysis for Ultracold Clouds Near BEC Transition Temperatures

When the temperature is very close to the critical temperature of quantum phase transition, the properties of a cloud will deviate from that of a classical gas, and the treatments in the last section based on Boltzmann statistics are insufficient. In this temperature regime, image analysis based on Bose statistics is necessary. For clarity, the relevant physical quantities will be derived from first principle, and the approach here follows closely to ref. [9].

The Bose distribution function is given by

$$n = \frac{1}{\mathrm{e}^{-(\mu-H)/k_\mathrm{B}T} - 1} = \sum_{j=1}^{\infty}(z\,\mathrm{e}^{-H/k_\mathrm{B}T})^j, \tag{3.19}$$

where H is the system Hamiltonian, μ is the chemical potential, and $z = \mathrm{e}^{\mu/k_\mathrm{B}T}$ is the fugacity [4]. The Hamiltonian of an ideal gas confined in a harmonic trap is just that of uncoupled harmonic oscillators,

$$H = \sum_{i=1}^{3}(\frac{p_i^2}{2m} + \frac{m\omega_i^2 r_i^2}{2}), \tag{3.20}$$

where $\omega_{1,2,3}$ are the trap frequencies of the trap.

Total Number of Atoms in Excited States Integrating the Bose distribution function over all phase space yields the total number of atoms in the excited states (thermal atoms):

$$N_\mathrm{th} = \frac{1}{h^3}\int \mathrm{d}^3r\mathrm{d}^3p\sum_{j=1}^{\infty}(z\,\mathrm{e}^{-H(\vec{r},\vec{p})/k_\mathrm{B}T})^j \tag{3.21a}$$

$$= (\frac{k_\mathrm{B}T}{\hbar\bar{\omega}})^3 g_3(z),\ T \geq T_c, \tag{3.21b}$$

where $\bar{\omega}$ is the mean trap frequency, and $g_3(z)$ is the Riemann Zeta function of fugacity z [5]. When the temperature T is below the critical temperature T_c, N_th is less than the total number of atoms in the trap, and the excess atoms are populated in the ground state of

---

[4] In Eq. 3.20 we have used the identity: $\frac{1}{x-1} = \sum\limits_{j=1}^{\infty}(\frac{1}{x})^j, x > 1$.

[5] Riemann Zeta function $g_l(z) \equiv \sum\limits_{j=1}^{\infty}\frac{z^j}{j^l}$

Table 3.1: Thermal and Bose condensed atoms in a harmonically trapped Bose gas.

T	thermal: N_{th}	condensate: N_c
$T \geq T_c$	$g_3(z)(\frac{k_{\mathrm{B}}T}{\hbar\bar{\omega}})^3, z \leq 1$	0
$T < T_c$	$g_3(1)(\frac{k_{\mathrm{B}}T}{\hbar\bar{\omega}})^3 = 1.202(\frac{k_{\mathrm{B}}T}{\hbar\bar{\omega}})^3$	$N - N_{\mathrm{th}}$

the trap — this is the Bose-Einstein condensate. Table 3.1 summarizes these results for the total number of atoms in the excited state (thermal component) and in the ground state (Bose-Einstein condensate) in different temperature regimes.

Density of a Trapped Thermal Gas Carrying out the integral in Eq. (3.21) over the momentum space only, we arrive at

$$N_{\mathrm{th}} = \frac{1}{\lambda_{\mathrm{dB}}^3} \int \mathrm{d}^3 r g_{3/2}(z\,\mathrm{e}^{-\sum\limits_{i=1}^{3} \frac{m\omega_i^2 r_i^2}{2k_{\mathrm{B}}T}}) = \int \mathrm{d}^3 r n_{\mathrm{th}}(\vec{r}), \tag{3.22}$$

where $\lambda_{\mathrm{dB}} = h/\sqrt{2\pi m k_{\mathrm{B}} T}$ is the thermal de Broglie wavelength. By comparison, we find the spatial density is given by

$$n_{\mathrm{th}}(\vec{r}) = \frac{1}{\lambda_{\mathrm{dB}}^3} g_{3/2}(z\,\mathrm{e}^{-\sum\limits_{i=1}^{3} \frac{m\omega_i^2 r_i^2}{2k_{\mathrm{B}}T}}) \; . \tag{3.23}$$

The 2D image of the cloud recorded on the CCD chip will be the integrated density profile over the axial direction of the imaging system, or column density. This column density profile can be easily found as

$$\widetilde{n}_{\mathrm{th}}(r_1, r_2) = \int \mathrm{d}r_3 n_{\mathrm{th}}(r) = \frac{1}{\lambda_{\mathrm{dB}}^3} \sqrt{\frac{2\pi k_{\mathrm{B}} T}{m\omega_3^2}} g_2(z\,\mathrm{e}^{-\sum\limits_{i=1}^{2} \frac{m\omega_i^2 r_i^2}{2k_{\mathrm{B}}T}}) \; . \tag{3.24}$$

Note that this is the column density of the cloud in the trap, and relevant only when the cloud is imaged in-situ.

Time-of-Flight Density Profile of a Thermal Cloud The TOF spatial density of a cloud is related to the original spatial distribution via the following integral,

$$n_{\mathrm{tof}}(\vec{r}, t) = \frac{1}{h^3} \int \mathrm{d}^3 r_0 \mathrm{d}^3 p \frac{\delta^{(3)}(\vec{r} - \vec{r}_0 - \frac{\vec{p}}{m} t)}{\mathrm{e}^{-(\mu - H(\vec{r}_0, \vec{p}))/k_{\mathrm{B}}T} - 1}. \tag{3.25}$$

Assuming that the expansion time $t >> \omega_1^{-1}, \omega_2^{-1}, \omega_3^{-1}$, the TOF density is given by

$$n_{\mathrm{tof}}(\vec{r}, t) = \frac{1}{\lambda_{\mathrm{dB}}^3} \frac{1}{(\bar{\omega} t)^3} g_{3/2}(z\, \mathrm{e}^{-\frac{m}{2k_{\mathrm{B}}T} \frac{r_1^2+r_2^2+r_3^2}{t^2}}) \; . \tag{3.26}$$

Integrating over the direction of optical axis of the imaging system, we obtain the column density,

$$\widetilde{n}_{\mathrm{tof}}(r_1, r_2, t) = A\, g_2(z\, \mathrm{e}^{-\frac{r_1^2+r_2^2}{2\sigma^2}}), \tag{3.27}$$

where $A = \frac{1}{\lambda_{\mathrm{dB}}^3} \frac{1}{(\bar{\omega} t)^3} \sqrt{\frac{2\pi k_{\mathrm{B}} T}{m} t^2}$, and $\sigma^2 = \frac{k_{\mathrm{B}} T}{m} t^2$.

Density and Radii of a Trapped BEC At zero temperature, the dynamics of a trapped BEC are described by the Gross-Pitaevskii (or nonlinear Schrödinger) equation [24]. Within the Thomas-Fermi (T-F) approximation [20, 79], in which the kinetic energy or the quantum pressure is neglected, the density in the trap is given by

$$n_{\mathrm{TF}}(\vec{r}) = \max\left(\frac{\mu - U(\vec{r})}{g}, 0 \right) \; . \tag{3.28}$$

Here $U(\vec{r})$ is the trap potential, μ is the chemical potential, and $g = 4\pi\hbar^2 a/m$ is the two-body interaction strength, where a is the s-wave scattering length. It is readily found that the density of the condensate in a harmonic trap, $n \propto |\psi(r)|^2$, has the form of an inverted parabola [20, 79],

$$n_{\mathrm{TF}}(\vec{r}) = \frac{15N}{8\pi \Pi_i R_{i,c}} \max(1 - \sum_{i=1}^{3} \frac{r_i^2}{R_{i,c}^2}, 0), \tag{3.29}$$

and the column density is

$$\tilde{n}_{\mathrm{TF}}(\vec{r}) = \tilde{n}_c(0) \max(1 - \sum_{i=1}^{2} \frac{r_i^2}{R_{i,c}^2}, 0)^{3/2}, \tag{3.30}$$

where $\tilde{n}_c(0)$ is the peak column density, and $R_{i,c}$ are the radii of the T-F order parameter. Here, $R_{i,c}$ are given by

$$R_{i,c} = \sqrt{\frac{2\mu}{m\omega_i^2}}. \tag{3.31}$$

The chemical potential is required to compute the T-F radii $R_{i,c}$, and it can be calculated using Eq. 3.28 with a harmonic trap potential and the normalization condition for the order parameter, $\int n(\vec{r}) \mathrm{d}^3 r = N$ (see Appendix F). The chemical potential is calculated as

$$\mu = \left(\frac{15\hbar^2 m^{1/2}}{2^{5/2}} N \bar{\omega}^3 a \right)^{2/5} \;, \tag{3.32}$$

where N is the number of atoms, $\bar{\omega}$ is the mean trap frequency, and a is the s-wave scattering length.

Time-of-Flight Density of a BEC The time-of-flight (TOF) images were first used to distinguish Bose-Einstein condensates from thermal clouds [1, 3], and the characteristic anisotropy of the expansion of condenstes released from non-spherical traps remains the standard signature of a condensate. For non-spherical trapping potentials, the direction with tighter confinement will lead to higher momentum and higher expansion rate along that direction. The TOF density profile is a simple rescaling of the in-situ condensate spatial density profile given by Eq. 3.29, and at any given infinitesimal expansion time, the TOF radii expand along a trajectory [80]

$$R_i(t) = \lambda_i(t) R_i(0),\ \ i = 1, 2, 3\,, \tag{3.33}$$

where $\lambda_i(t)$ satisfy

$$\ddot{\lambda}_i(t) = \frac{\omega_i^2(0)}{\lambda_i \lambda_1 \lambda_2 \lambda_3},\ \ i = 1, 2, 3. \tag{3.34}$$

Specifically, for a cigar shape condensate ($\omega_1 = \omega_2 = \omega_\perp \gg \omega_z$), the radii will grow according to [80]

$$R_{c,\perp}(\tau) = R_{c,\perp}(0)\sqrt{1+\tau^2}, \tag{3.35a}$$

$$Z_c(\tau) \simeq Z_c(0)[1 + \epsilon^2(\tau \arctan\tau - \ln\sqrt{1+\tau^2})], \tag{3.35b}$$

where $\tau = \omega_\perp t$ is the scaled expansion time, and $\epsilon = \omega_z/\omega_\perp \ll 1$ is the inverse of the aspect ratio of the trap. These equations can be used to determine the density of a BEC directly from time of flight images.

2D Image Fit for Atomic Clouds To extract the temperature, number of atoms, and other quantities from the images, we fit the images with 2D functions. For $T \gg T_c$ we simply fit a 2D Gaussian to the cloud image. For $T \gtrsim T_c$, it is found that 2D Gaussian fit always underestimates the temperature. We therefore fit a 2D Gaussian to the wings of the cloud image, and then use the fit results as initial conditions for fitting the Bose function given in Eq. (3.27) to the image. For $T < T_c$ the cloud has both a thermal gas and condensate component, so we fit to the sum of Eq. (3.27) and Eq. (3.30). Therefore,

$$\widetilde{n}_{\mathrm{tof,th}}(\vec{r}) = A\,\mathrm{e}^{-\frac{r_1^2+r_2^2}{2\sigma^2}},\; T \gg T_c \tag{3.36a}$$

$$\widetilde{n}_{\mathrm{tof,tot}}(\vec{r}) = A\,g_2(z\,\mathrm{e}^{-\frac{r_1^2+r_2^2}{2\sigma^2}}),\; T \gtrsim T_c \tag{3.36b}$$

$$\widetilde{n}_{\mathrm{tof,tot}}(\vec{r}) = A\,g_2(\mathrm{e}^{-\frac{r_1^2+r_2^2}{2\sigma^2}}) + B\max(1-\sum_{i=1}^{2}\frac{r_i^2}{R_i^2}, 0)^{3/2},\; T \leq T_c \tag{3.36c}$$

where A, z, σ, B, and R_i's are free fitting parameters.

The image fitting is very useful for extracting important physical quantities. However, it is noted that the fitting routines in certain conditions do not converge to a single valued result. Firstly, the fit to the Bose function when $T > T_c$ does not always result in unique values of A, z, and σ. Secondly, it is known that the presence of a condensate causes depletion of thermal atoms at trap center due to atomic interactions [81]. Since the ideal gas ansatz given above does not account for the repulsive interactions between condensate and thermal gas due to the positive scattering length of ^{87}Rb, it will tend to overestimate the number of thermal atoms and underestimate the number of condensed atoms. Thirdly, a bimodial fitting is not robust when one component is significantly smaller than the other. This happens at the onset of the Bose-Einstein condensation, where the BEC component is much smaller than the thermal gas, and for $T \ll T_c$ when the cloud is almost a pure condensate. Nonetheless, the fitting models provide a reasonable approximation to the real physical system. For illustration purposes, a 2D image fit at temperature at $2T_c$ is shown in Fig. 3.4, and a typical bimodal fit to a partially condensed cloud is displayed in Fig. 3.5.

In the studies of large spinor condensates, spin domains are observed to form in different spin components. While the total condensate wavefunction fits well with the Thomas-Fermi form, the wavefunction for each spin component can not be described by a simple Thomas-Fermi form due to domain formation. So, for image fitting to a spinor condensate, we only fit the Bose function with fugacity $z = 1$ to the wings of the thermal component, or

$$\widetilde{n}_{\mathrm{tof}}(r_1, r_2, t) = A\,g_2(\mathrm{e}^{-\frac{r_1^2+r_2^2}{2\sigma^2}}), \tag{3.37}$$

This is done by masking off the central region where the condensate resides. Fig. 3.6

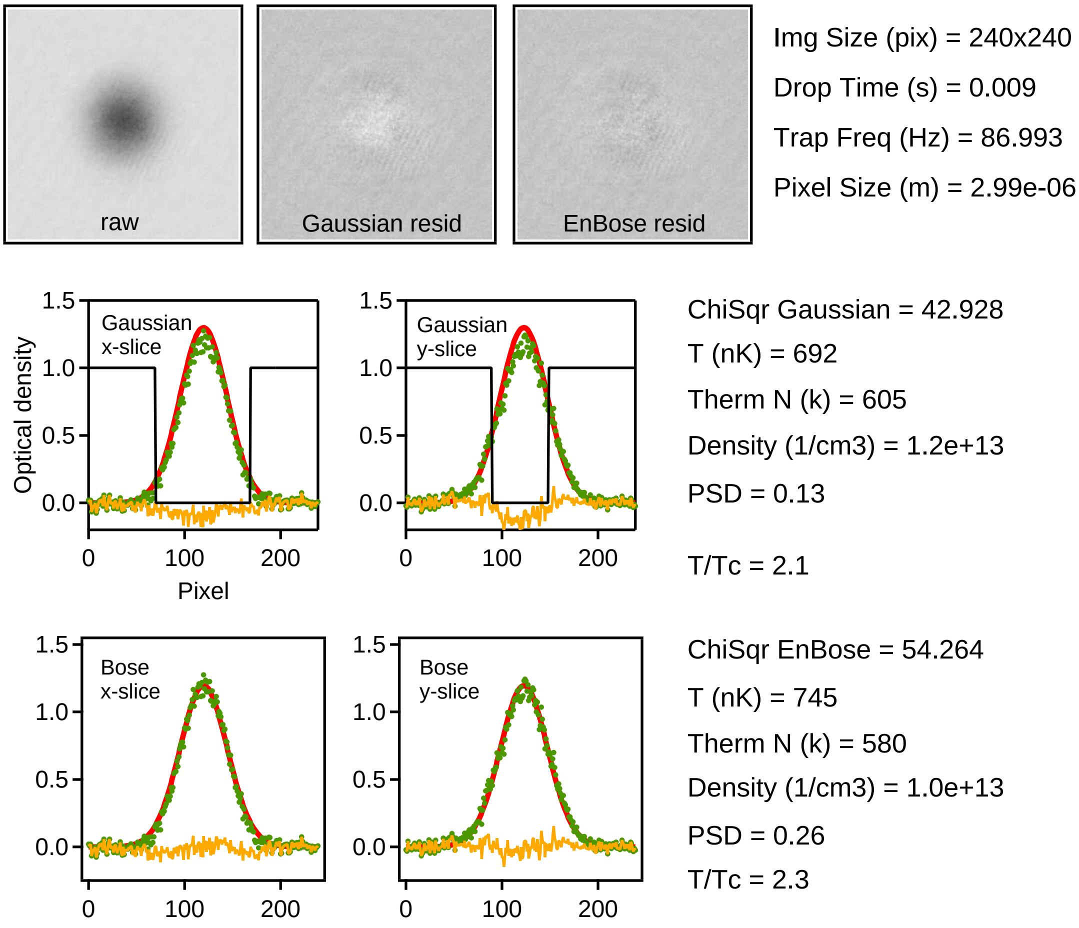

Figure 3.4: 2D image fits for a thermal cloud. The images shown here are the fitting results of the Gaussian fit and Bose fit for the $m_F = -1$ component in a spinor condensate. When the temperature is close to the critical temperature, the Gaussian fit always underestimates the temperature. In addition, the Gaussian ansatz does not fit well to the central part of the cloud. Therefore, this ansatz only fits the tails of the thermal cloud. The fit results are then used as initial conditions for fitting with a Bose distribution. Top images (left to right) are raw image, image with the Gaussian fit subtracted, and image with the Bose fit subtracted, respectively.

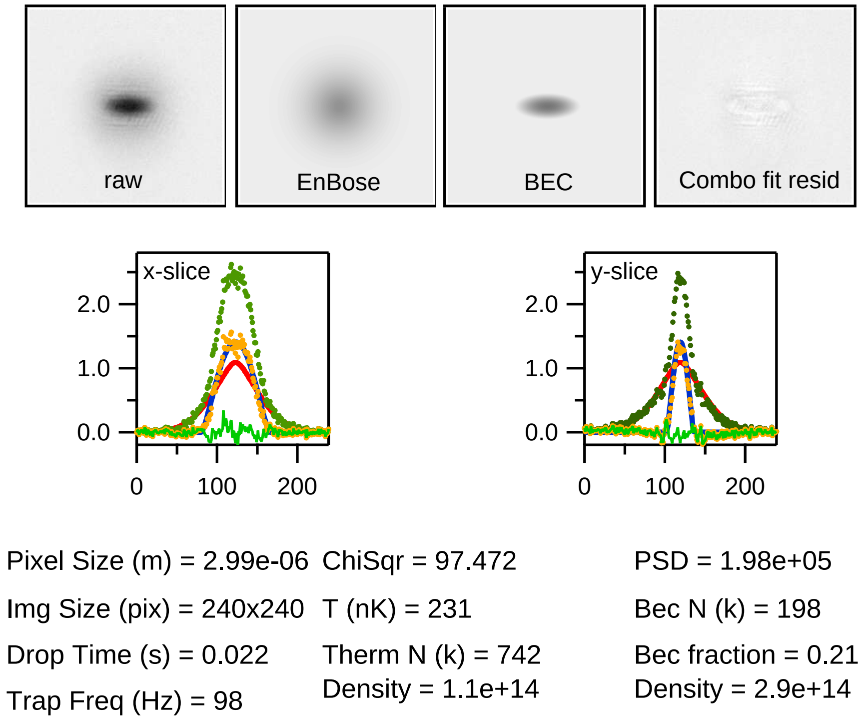

Pixel Size (m) = 2.99e-06
Img Size (pix) = 240x240
Drop Time (s) = 0.022
Trap Freq (Hz) = 98

ChiSqr = 97.472
T (nK) = 231
Therm N (k) = 742
Density = 1.1e+14

PSD = 1.98e+05
Bec N (k) = 198
Bec fraction = 0.21
Density = 2.9e+14

Figure 3.5: Bimodal fit to the cloud below the BEC critical temperature. The images shown here are the fitting results of the bimodal fit results of a thermal-condensate mixture when the temperature is below the critical temperature. The bimodal ansatz is given in Eq. (3.36c). Top images (left to right) are raw image, fitted thermal component, fitted condensate component, and image with both thermal and condensate fits subtracted off from the raw image, respectively.

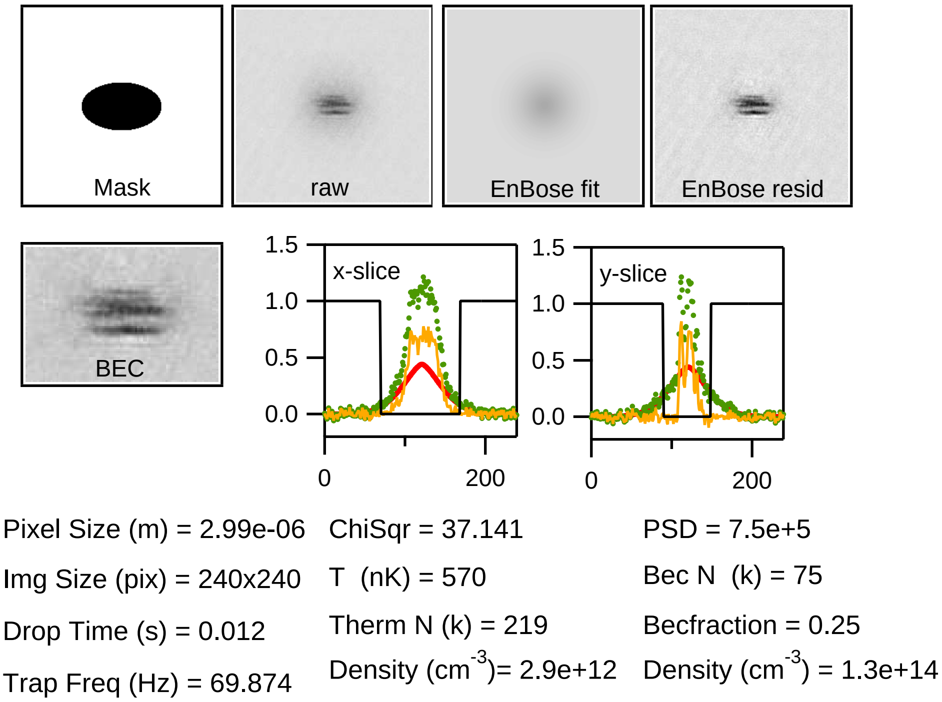

Pixel Size (m) = 2.99e-06

Img Size (pix) = 240x240

Drop Time (s) = 0.012

Trap Freq (Hz) = 69.874

ChiSqr = 37.141

T (nK) = 570

Therm N (k) = 219

Density (cm^{-3})= 2.9e+12

PSD = 7.5e+5

Bec N (k) = 75

Becfraction = 0.25

Density (cm^{-3}) = 1.3e+14

Figure 3.6: Bose fit to wings of the thermal cloud with fugacity $z = 1$. The images shown here are the fitting results of the $|F = 1, m_F = 0\rangle$ spin component. To fit to the wings of the thermal cloud only, we apply a ellipse mask to exclude fitting to the central area where the condensate resides. This fit is useful when the condensate is not of the simple Thomas-Fermi form, which often happens when spin domains developed in a large spinor condensate such as in this particular case. Top images (left to right) are the mask, raw image, thermal component, and image with thermal component subtracted off the raw image (condensate component), respectively.

illustrates the results of a typical fit with the Bose function. Again, the fit results generally depends on the mask shape and size, and the results may vary up to 50% due to change of applying masks.

Phase Space Density (PSD) When the temperature $T \geq T_c$, the peak PSD is given by

$$\Lambda_0 = \lambda_{\text{dB}}^3 n_0 = g_{3/2}(z), \;\; z \leq 1. \tag{3.38}$$

Here, T_c is the critical temperature, and z is the fugacity. In a case where $T >> T_c$, z is much less than 1 and the PSD is approximated as $\Lambda_0 \simeq z$. To compute the PSD, a knowledge of the fugacity or chemical potential is necessary. However, they are often difficult to measure. Recall that when $T >> T_c$ a Bose distribution function is approximated by a Boltzmann

Table 3.2: Phase space density in different temperature regime. Here $z = \mathrm{e}^{\mu/k_{\mathrm{B}}T}$ is the fugacity, and μ is the chemical potential.

T	Λ_0	Λ' (Approx.)
$T \geq T_c$	$g_{3/2}(z)$, $z \leq 1$	$N(\frac{\hbar\bar{\omega}}{k_{\mathrm{B}}T})^3 = g_3(z)$ z
$T = T_c$	$g_{3/2}(1) = 2.612$	
$T < T_c$	N_c	

distribution, then the PSD can be conveniently estimated using Eq. 3.18.

When $T < T_c$, the total number of atoms is greater than the available occupation number in the excited states, and the excess atoms will Bose condense in the ground state. This results in a macroscopic number of atoms sharing a single quantum state, *i.e.*, the ground state. Then the peak PSD is simply $\Lambda_0 = N_c$, where N_c is the number of atoms in the condensate.

Table 3.2 lists the phase space density and its approximation in different temperature regimes, and the numerical error due to the approximation is given in Fig. 3.7. When the temperature $T \gtrsim T_c$, the approximation error can be as large as 60%. Nevertheless, the approximation given by Eq. 3.18 is easy to apply and useful for characterizing evaporative cooling trajectories which will be seen in the next chapter.

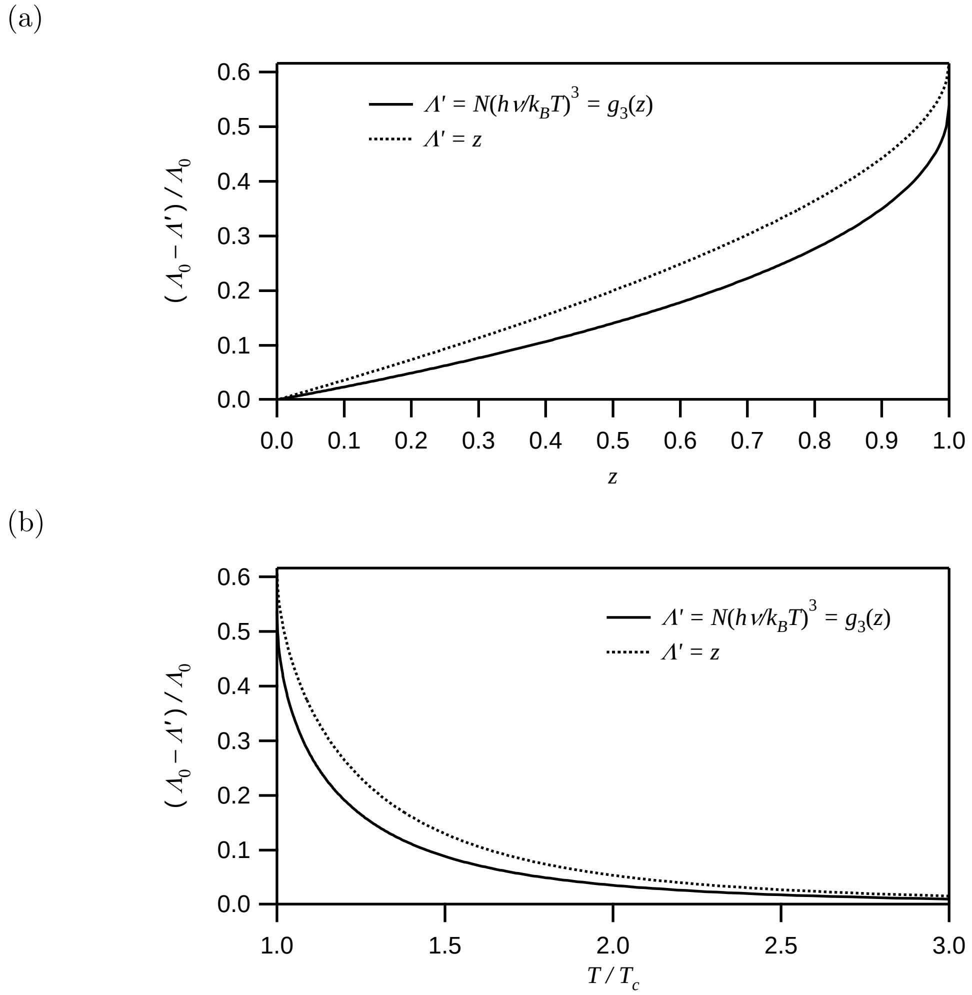

Figure 3.7: Approximation error for the PSD. (a) The approximation error vs. fugacity z. (b) The approximation error vs. T/T_c. Here, $T/T_c = (g_3(1)/g_3(z))^{1/3}$ is a more convenient unit for experimentalists. These plots show that $N(\frac{\hbar\bar{\omega}}{k_B T})^3$ is a better approximation for the PSD. However, when T approaches T_c, the error can be as large as 60%.

CHAPTER IV

ALL-OPTICAL BEC EXPERIMENTS

Given the tremendous impact of BEC research in the last 11 years and the continued growth of the field, it is important to explore different methods for reaching BEC, particularly methods that offer new capabilities, simplicity, or speed. Our group demonstrated such a method by creating a Bose condensate of ^{87}Rb atoms directly in a crossed-beam optical dipole force trap of tightly focused CO_2 laser beams [34]. In the broader scope of research with ultracold degenerate gases, our system stood out for several reasons. First, all-optical BEC provided the first new path to achieving BEC since the first pioneering demonstrations [1, 3, 2], and it was surprisingly simple and an order of magnitude faster than standard BEC experiments. Secondly, optical trapping potentials can be essentially spin-independent and hence offer unique capabilities for trapping atoms and molecules not amenable to magnetic trapping. In particular, all-optical BEC experiments are ideally suited for studying the dynamics of condensates with internal spin, or spinor condensates. Since the realization of our first all-optical BEC in ^{87}Rb [34, 82, 83], several other atoms, Cs [84], Yb [36], Na [85], and (fermionic) ^{6}Li [86] have been condensed in all-optical traps as well. Finally, a rich variety of spatial confinement geometries can be easily engineered in optical traps, including large period one- to three-dimensional lattices in which individual sites can be resolved and addressed [87]. This technical advantage allows optical traps to find applications in testing condensed matter theories [14, 88] and in quantum information science [89, 90, 91, 92]. In this chapter, we give an overview of our all-optical BEC techniques.

4.1 Review of First All-Optical BEC

All-optical methods of reaching the BEC phase transition have been pursued since the early days of laser cooling [93, 94]. Evaporative cooling in optical traps was first demonstrated in 1994, where, starting with only 5000 atoms, a phase space density increase of a factor of 30 was realized [70]. Whereas the first demonstrations of evaporative cooling of alkali atoms in magnetic traps lead quickly to the observation of BEC, the progress in optical traps was slower. A principle challenge faced by all-optical traps was that the small trap volume provided by the focused lasers (typically much less than 1 mm^3) limits the number of atoms that can be loaded in the trap. Also, lowering the trap depth to force evaporation also lowers the trap oscillation frequency and the rethermalization rate. Hence the evaporation rate can slow down prohibitively. Finally, optical traps have historically suffered from excessive heating rates either due to intrinsic spontaneous scattering of photons from the trapping beams or the technical noise of the trapping laser [95, 96]. Best previous efforts on optical trapping beyond the limits set by Doppler cooling yielded atomic phase space densities a factor of 3 away from the BEC transition [73, 97].

Despite the technical challenges, our group successfully realized the first all-optical BEC experiment in 2001 [34]. In this impressive experiment Murray Barrett *et al.* employed a $\mathrm{CO_2}$ laser dipole force trap [98] in a cross trap geometry. Each beam had a maximum power of 12 W, and the beams were focused to a minimum waist $\sim$50 μm. Initially 2×10^6 atoms were loaded at a temperature of 70 μK and densities $> 10^{14}$ atoms/cm^3. Forced evaporative cooling of the atomic sample was achieved by lowering the trap beam powers 50-fold over 2 s. The BEC transition occurred at temperature of $\sim$ 300 nK and beam powers of 300 mW. At the lowest final temperature, mostly pure condensate which contained 30,000 atoms was created [34, 62].

The initial success in achieving BEC in an optical trap hinged on the very high spatial and phase space densities achieved during the loading process. The initial spatial density loaded into the cross dipole trap exceed 10^{14} atoms/cm^3, which is 3 orders of magnitude higher than that of the loading MOT. Given the well-known density limitations in laser cooling due to reabsorption of scattered radiation and photo-associative losses induced by the cooling fields, it is surprising that such high densities could be achieved in an optical trap using only standard sub-Doppler cooling techniques. Although loading of optical dipole traps has been the subject of several experimental [77, 99] and theoretical [100] studies, none of these apply specifically to our configuration.

The next section will be devoted to the studies on CO_2 laser trap loading dynamics. We note that the these studies were begun by Murray Barrett while finishing up his PhD thesis. Since the impressive results carried out by Murray are yet unpublished, and a better knowledge of loading dynamics is essential for developing new trap geometries, we will summarize them in the next section. The understanding of trap loading also led Murray to directly create condensates in 1-D lattice. We will also summarize the 1-D lattice BEC experiment later in this chapter. Finally, we note that while the experimental techniques for the 1-D lattice were developed by Murray, most of the data presented here were taken at a later date by myself.

4.2 Trap Loading Studies

Our BEC experiments employ CO_2 laser optical traps loaded from a standard ^{87}Rb vapor cell MOT [62]. The experiment begins with loading the MOT for 10 s directly from the thermal vapor during which we collect up to 5×10^8 atoms. After loading the MOT, the cooling configuration is changed to achieve sub-Doppler cooling in order to maximize the transfer of atoms to the optical trap. The repump intensity is first lowered to 15 μW/cm^2 for 20 ms, and then the MOT trap beams are detuned to the red of the trapping transition by 140 MHz for 40 ms. At this point the MOT beams are extinguished, and the current in the MOT coils is turned off. In order to optically pump the atoms into the $F = 1$ hyperfine states, the repump light is shuttered off 1 ms before the trap beams are extinguished; the efficiency of the optical pumping to the $F = 1$ state are measured to be $> 95\%$. The CO_2 laser beams are left on at full power throughout the MOT loading and dipole trap loading process. This sub-Doppler cooling scheme is a variation of the temporal dark MOT technique [66], and the timing scheme is illustrated in Fig. 4.1. This cooling step is crucial for efficient loading into the optical trap.

The results of loading the single focused beam trap, the 1-D lattice trap, as well as the cross trap are summarized in the first three columns of Table 4.1 [62]. The 1-D lattice is obtained by retro-reflecting the laser beam, and it produces an array of microtraps separated by half the wavelength (5.3 μm) [77]. While each of these traps provide much higher spatial

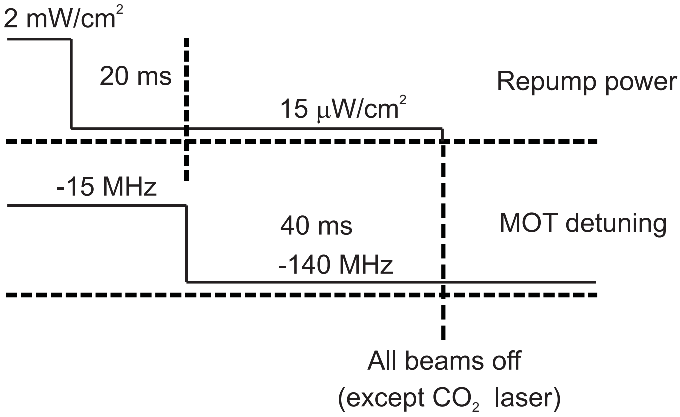

Figure 4.1: Temporal dark MOT technique for trap loading. After we collect $\sim 10^8$ atoms in the MOT, the repump power is ramped down to 15 μW, and the detuning is ramped up to -140 MHz for sub-Doppler cooling. In the end of sub-Doppler cooling, the atoms can be cooled down to 30 μK.

and phase space densities than the MOT, only the direct loading provided by the cross trap offers high enough initial density and phase space density for reaching quantum degeneracy in our experiment. The key to the cross geometry is that it provides a relatively large loading volume (2x greater than the single focus trap) as well as tight confinement in three dimensions, provided the atoms are localized at the intersection region (the 'dimple'). In the case of the single focus trap, the elastic collision rate (which determines the speed of evaporation) is too low to implement significant cooling before excess loss from background vacuum collisions. For the 1D lattice, the collision rate is substantially improved, but with only 4000 atoms initially trapped in each microtrap the phase space density only increases by a factor of 15 before running out of atoms — this is similar to the early evaporative cooling results reported in [70].

Our current understanding of the loading dynamics is that it is not the laser cooling process alone that provides this localization (and corresponding high densities), but rather this results in large part from a rapid thermalization and evaporation of the atoms in the trap following a non-equilibrium loading process from the MOT. To a reasonable approximation, sub-Doppler laser cooling provides a density-limited sample of low kinetic energy atoms. Hence we can imagine that when the laser cooling operates in conjunction with the optical dipole potential, it serves to 'fill' the trap with a quasi-uniform density of atoms with low

Table 4.1: Comparison on Optical Trap Loading. Note that except the number of atoms, other quantities are measurement at thermal equilibrium.

	Single Beam	1-D Lattice (Direct loading)	Cross	1-D Lattice (Transferred)	Single Beam (Large volume)
Trapped atoms	1×10^6	1×10^6 (250 microtraps)	2×10^6	1×10^6 (1 - 4 microtraps)	30×10^6
Temperature (μK)	20	35	75	10	120
Potential depth (μK)	350	230	700	120	800
Trap frequency (Hz)	550	3000	1600	2100	500
Density (cm^{-3})	$> 10^{12}$	10^{13}	$> 10^{14}$	$> 10^{14}$	$> 10^{13}$
Phase space density	> 0.0001	0.0003	0.001 - 0.005	> 0.01	0.0001
Collision rate (s^{-1})	200	800	10,000	10,000	10,000 (trap compression)
Evaporation Time (s)			2	2	2
Bose condensed atoms			30,000	15,000 - 30,000	300,000

Table 4.2: Study the role of redistribution — snap on experiments. Here H-trap is the horizontal trap, and D-trap is the diagonal trap. Note that except the number of atoms, other quantities are measurement at thermal equilibrium, which is about 20 ms after loading.

	H-trap (Load normally)	H-trap (Snap on)	H-trap + delayed D-trap (D Snap on)
Trapped atoms	1×10^6	3×10^5	1×10^6
Temperature (μK)	20	24	30
Potential depth (μK)	350	350	700
Trap frequency (Hz)	550	550	1600
Density (cm^{-3})	$> 10^{12}$	10^{12}	$> 3 \times 10^{13}$
Phase space density	$> 10^{-4}$	$> 10^{-5}$	$> 3 \times 10^{-3}$
Collision rate (s^{-1})	200	50	3500

kinetic energy. When the cooling light is extinguished, the initial distribution then relaxes to an approximate Maxwell-Boltzmann distribution appropriate to the trapping potential through a combination of rethermalization and evaporation, and this relaxation process can raise the density significantly, particularly in strongly deformed traps like the cross trap.

We have performed two simple experiments to verify this mechanism [1], and the results are summarized in Table 4.2. First, instead of laser cooling the atoms into the optical trap, the optical trap is snapped on suddenly after all cooling light has been extinguished, thereby eliminating the role of the laser cooling in trap loading process altogether [101]. Despite the excess energy added to the atoms from the potential energy of the trap, within 100 ms, the optically trapped atoms achieve spatial densities 200 times larger than in the MOT with a phase-space density increase of a factor of 30. In a second experiment, the horizontal single beam trap is first loaded using the standard methods to achieve the properties in the first column of Table 4.2. Then the diagonal cross-beam was suddenly switched on. The atoms quickly ($\sim$ 20 ms) coalesce to the dimple region of the cross with final properties within a factor of 3 of the usual cross trap [101]. As will be described in the next section, a variation of this method can be used to greatly enhance the number of atoms loaded into the microtraps of the 1-D lattice.

---

[1] "The dynamics of neutral atom traps: the role of redistribution," M. D. Barrett, M.-S. Chang, and M. S. Chapman, unpublished.

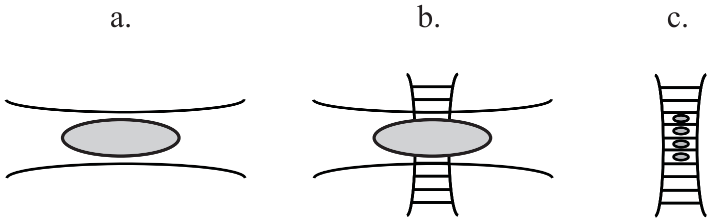

Figure 4.2: Loading atoms into only a few sites in an optical lattice. To transfer atoms from a single-focus trap to a 1-D optical lattice, the lattice is adiabatically turned on while the single-focus trap is adiabatically turned off. The transfer takes 50 ms, and we can transfer nearly 100% of the atoms into only a few lattice sites.

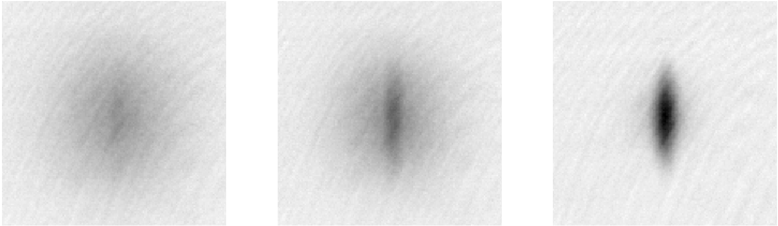

Figure 4.3: Bose-Einstein Condensation in the 1-D lattice. Temperature is lowered across the quantum Phase transition criticality (left to right).

4.3 Bose Condensation in 1D Lattice

Condensates in large period optical lattices have found several important applications due to the potential of engineering controlled coupling between arrays of condensates. A 1-D lattice was used in the first demonstration of Josephson tunneling between lattice wells [12], the generation of number squeezed states [102], demonstration of dynamical tunneling [103], and in transport measurements [104]. In a series of recent experiments with a 3-D lattice, the Munich group has demonstrated a Mott insulator transition [14], and revivals of the condensate wavefunction [105]. In all of these experiments, a sub-micron wavelength optical lattice is employed, and hence the individual lattice sites are not observed. Instead, the coupling between lattice sites is observed as an interference pattern between many phase coherent condensates. The CO_2 laser trap provides a lattice in a much different regime, with a lattice spacing sufficiently large (5.3 μm) to optically resolve the individual microtraps [87]. As we discuss below, it is even possible to isolate only 2 microtraps in the lattice to realize a double well potential.

Our new understanding of the loading process has allowed us to increase the number of atoms trapped in a lattice site by over a factor of 200, and with this, we have succeeded in creating condensates directly in the lattice trap. To increase the number of atoms loaded in the microtraps, we have implemented a loading scheme as shown in Fig. 4.2. A travelling beam loads $\sim 10^6$ atoms from the MOT and serves to 'funnel' a large number of atoms into only a few microtraps when the crossed standing wave trap is turned on later. From these initial conditions, evaporation proceeds readily as with the cross trap, and the BEC transition occurs at a critical temperature, $T_c = 800$ nK with 110,000 atoms and trap oscillation frequencies of $(f_1, f_2, f_3) = (100, 140, 3200)$ Hz. The loading parameters are listed in the fourth column of Table 4.1, and images of evaporation in the lattice through BEC phase transition is shown in Fig. 4.3.

4.3.1 Measurement and Control of The Lattice Sites Occupied

A unique feature of CO_2 lattice is the large, (5.3 μm) spacing of the lattice sites. Our current imaging system lacks sufficient resolution to image the individual microtraps. While this will be upgraded in the future, in the meantime we have developed a technique to measure the site occupancy in the standing wave traps by converting the spatial separation to a separation in momentum space during time-of-flight imaging. This is done by superposing a larger-scale optical harmonic potential along the direction of the standing wave, and releasing the microtraps into this potential for a short duration before final release of the atoms. Each microtrap is initially located at a different elevation of the added potential and is subsequently accelerated towards the bottom of the potential at different rates. When the added potential is also turned off, the microtrapped atoms will separate in space according to their final velocity. The schematic and the time-of-flight (TOF) absorptive images of the atomic clouds are illustrated in Fig. 4.4. With this diagnostic tool, we can have reasonably precise control over the occupation of the microtraps by varying the cloud size in the single focus beam and by changing the lattice site position upon the time of transfer to the lattice. In Fig. 4.5 we demonstrate loading into one to three lattice sites. In the future, being able to control loading in different sites will be a convenient experimental technique for studying the dynamics and interplay of these microtrap condensate arrays.

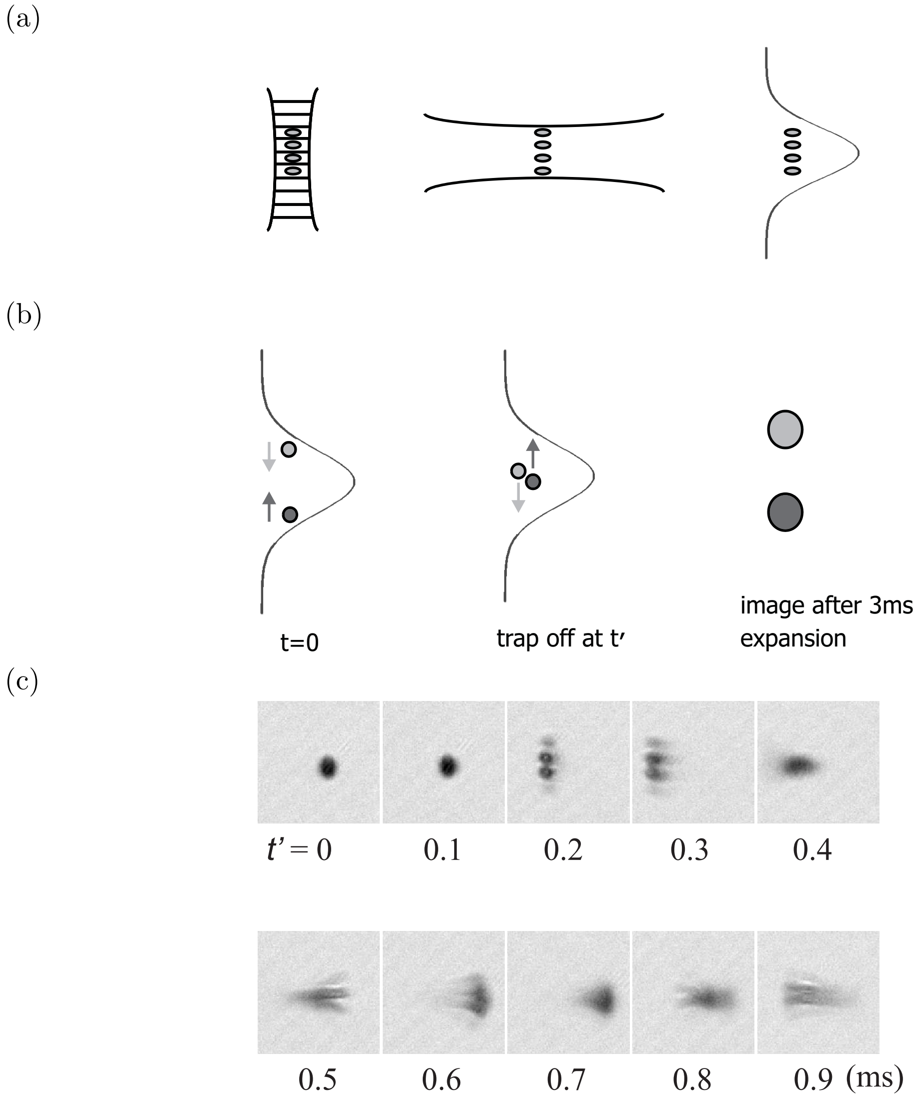

Figure 4.4: Measuring the lattice sites occupation. (a) In order to measure the number of sites that are populated, we transfer the atoms back to the single-focus trap, and allow the clouds to slosh inside a larger potential provided by this trap. With this technique, we can convert the position dependent potential to the kinetic energy of the clouds. (b) The trap is turned off after various amount of slashing time, and each individual thermal clouds can be optical resolved after 3 ms of TOF. (c) Absorptive images of actual measurements. The single-focus trap is oriented 45° with respect to the imaging axis, therefore, we can observe 2-D harmonic motions when the two traps are not perfectly crossed. Meanwhile, this technique also allows us to visually measure the radial trap frequency. In this particular case, the radial trap frequency is measured to be 1.4 kHz.

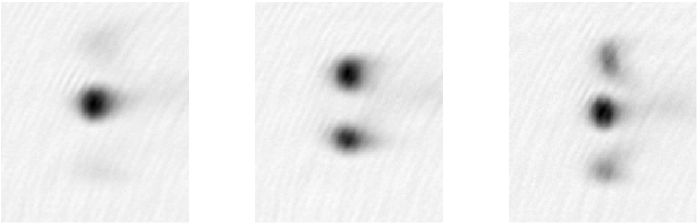

Figure 4.5: Image of the distinct microtraps following 'magnification' provide by additional harmonic confinement. Images show population of 1, 2 and 3 lattice sites (from left to right).

4.3.2 Matter Wave Interference

One of the hallmarks of BEC is the macroscopic quantum coherence of the gas. In a well-known experiment performed by the MIT group [10], this coherence was observed as matter-wave interference by releasing two condensates trapped in an elongated magnetic trap separated by an optical dipole barrier. We have been able to observe interference fringes in time of flight images of our released condensates as shown in Fig. 4.6. The three cases in this figure corresponds to the three cases of site occupation in Fig. 4.5. The fringes for two and three condensates are clearly seen, while for one condensate there is no discernible fringes. The fringe contrast for the cases of two and three condensates are not very high. It is typically less than 20% for two-site interference and even lower for the case of three condensates. In addition, the interference fringe spacing and contrast from three expanding condensates also vary from shot to shot. This is consistent with the fact that the relative phase of the three condensates are random. The low contrast in the two-site interference is in part due to the fact that the fringes are the sum of three fringe patterns of the Zeeman components. As will be seen in later chapters, the phase of a spinor rotates fast in an external magnetic field, nonuniform stray magnetic fields in our vacuum chamber can cause differential phase shifts for the different spin components of the spinors in different lattice sites, and hence results in lower interference fringe contrast. Indeed, as shown in Fig. 4.7 the fringe contrast of two-condensate interference is much higher (80%) when the internal spin state of the condensates are polarized in the $|F = 1, m_F = -1\rangle$ state.

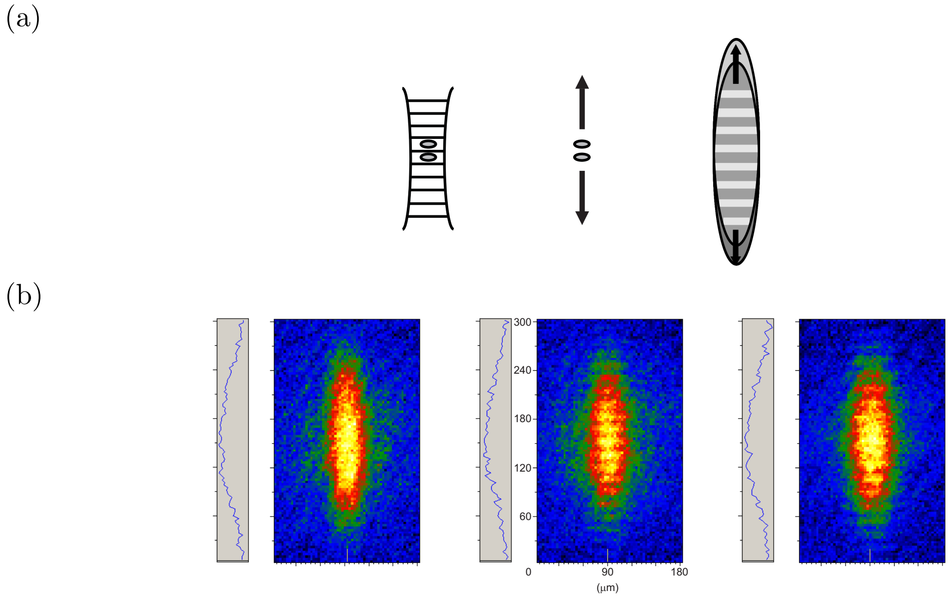

Figure 4.6: Interference of condensates and spatial coherence of matter waves. Condensates are macroscopic coherent matter waves, therefore will interfere when they overlap in space. When few independent condensates created in the optical lattice are overlapped after free expansion, they will interfere and create spatial fringes. (a) Schematic drawing of interference of lattice condensates. (b) The condensates images correspond to the site occupation in Fig. 4.5 (left to right). The the interference fringe spacing are 15 μm for two-site interference (middle) and 18 μm for three-site interference (right). Meanwhile, the fringe contrast for two-slit interference is typically less than 20% while that for the three-slit interference is somewhat lower and varying.

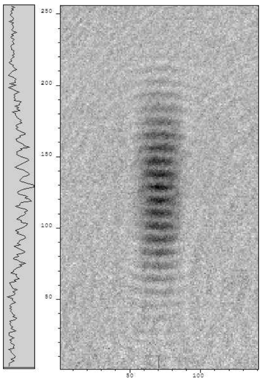

Figure 4.7: Interference of 30,000 atoms in the $|F = 1, m_F = -1\rangle$ state. In this case, the contrast of the interference is 80% and is much higher than in Fig. 4.6. This suggests the phase different among three spin components are different in different sites. The time of flight is 26 ms, and the fringe spacing is measured to be 24 μm. The field of view is 370×680 μm^2.

The spacing resulting from two expanding condensates is given by the de Broglie wavelength of the relative motion of the two independent condensates [10],

$$\lambda_{rel} = \frac{h}{mv_{rel}} \ , \tag{4.1}$$

where the relative velocity is determined by

$$v_{rel} = \frac{d}{\tau_{exp}}. \tag{4.2}$$

Here d is the separation of the condensates, and for our experiment, the spacing of the condensates is 5.3 μm (fixed by the standing wave). Given the expansion time $\tau_{exp} = 26$ ms, the relative velocity is calculated to be 200 μm/s, and the theoretical fringe spacing should be 22.5 μm. The fringe spacing in Fig. 4.7 is measured to be 24 μm, which is in good agreement with the theoretical prediction.

4.4 Bose Condensation in a Single Focus Trap

The key to reaching Bose condensation in an all-optical trap is efficient loading in a tight confining potential for subsequent evaporative cooling. This understanding has led us to create condensates in a cross trap and in a 1D lattice with an improved loading scheme. The tight confinement in the cross trap and 1D lattice microtraps can lead to high densities and high collision rates, however, the tight confinement will also cause a small trap volume.

This trap volume limitation has limited the initial number of atoms loaded into the trap, and eventually limited the final condensate size to 30,000 atoms in both of the cross and 1-D lattice our optical traps. Therefore, a larger trap volume is desired for creating larger stable condensates. A large-waist single focus trap is an ideal candidate as it is the simplest trap geometry, and it provides relatively large trap volume. As shown in the first column of Table 4.1, however, the initial loading number and collision rate in our single focus trap are not sufficient to reach quantum degeneracy. In a recent experiment by Gennini *et al.*, a CO_2 laser was strongly focused to a beam waist of 27 μm [82] from which a condensate was created directly in the single focus trap. This tight trap loaded 4×10^6 atoms with initial density of 1×10^{13} cm^{-1}, and phase space density of 1×10^{-4}. A condensate of 12,000 atoms was created in their single-focus trap after 7 s of forced evaporation.

In a single focus trap, the trap volume scales strongly with the beam waist, or $V \propto w_0^4$, where w_0 is the beam waist at trap location. Meanwhile, mean trap frequency scales as $\bar{\omega} \propto w_0^{-7/3}$. Realizing a tight and large volume single focus optical trap seems contradictory at first glance. However, we have learned from the 1D lattice condensate experiment that large loading volume for efficient loading and tight confining potentials for efficient evaporative cooling can be separated in time. Therefore, by varying the beam waist w_0 in real time, it is then possible to optimize both efficient loading and high collision rate in a single focus trap. In particular, under adiabatic compression which is often true in an optical trap due to its relatively high trap frequencies compared to the speed of compression, the density and the elastic collision rate scale as $n \propto w_0^{-4}$ and $\gamma_{\text{el}} \propto \ w_0^{-5}$, respectively.

The beam waist of a focused Gaussian beam is given by the formula, $w_0 = \lambda\ f/(\pi R)$, where λ, f, and R are the wavelength, focal length of the lens, and input beam radius respectively. Therefore, the beam waist can be varied by changing the R and/or f. We chose to change the input beam size of the gaussian beam, for it can be easily achieved via a zoom lens telescope. This trap compression technique was first developed by Weiss's group in a crossed YAG laser dipole trap [83], and we adopted this technique to compress our single focus trap. As shown in Fig. 4.8.a, the optical trapping volume is maximized by minimizing the CO_2 beam diameter on the input side of the final lens (L3). The trap

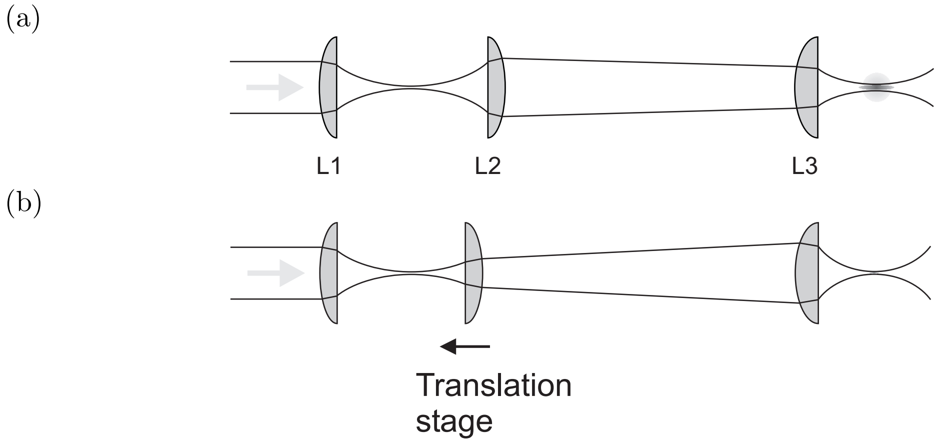

Figure 4.8: Loading and dynamics compression in a single focus trap. (a) A CO_2 laser is slightly converging after passing through a telescope formed by L1 and L2. This results in a small beam radius on the input side of L3 and a large beam waist at trap location (focus). (b) After trap loading is finished, the trap is compressed by increasing the beam diameter radius at L3. This is accomplished by ramping L2 toward L1. Note that the focus length of L3 is 3.8 cm, and this lens is fixed inside the vacuum chamber.

is compressed by increasing the beam diameter at L3, which is achieved by ramping L2 as shown in Fig. 4.8.b.

To estimate the focus spot size at the trap location, we use simple ray tracing formula for a paraxial gaussian beam [106]. We measure the trap frequencies for different L2 locations, and, with the known CO_2 laser power, the spot size at focus can be calculated. It is noted that our telescope is not a zoom lens beam expander, which would be preferable but more complicated. Due to this reason, the trap location will also move when the focus spot size is changed, which can also be estimated via the simple ray tracing formula. The ray tracing predictions and the measurement results are shown in Fig. 4.9.b and 4.9.c. The measured beam size at the trap location deviates from the prediction when the trap size is small, possibly because the spatial mode of our laser is not a perfect Gaussian mode. Indeed, our CO_2 laser power is ramped by a high power acousto-optic modulator, and the spatial mode after the AOM is somewhat distorted. The displacement of the trap location does not fully agree with the prediction of the ray tracing either, and we suspect this deviation is due to the astigmatism of the CO_2 laser beam after the AOM.

We begin by collecting up to 5×10^8 cold atoms in a simple vapor cell ^{87}Rb magneto-optical trap (MOT), which is overlapped with a large volume single focus trap, formed

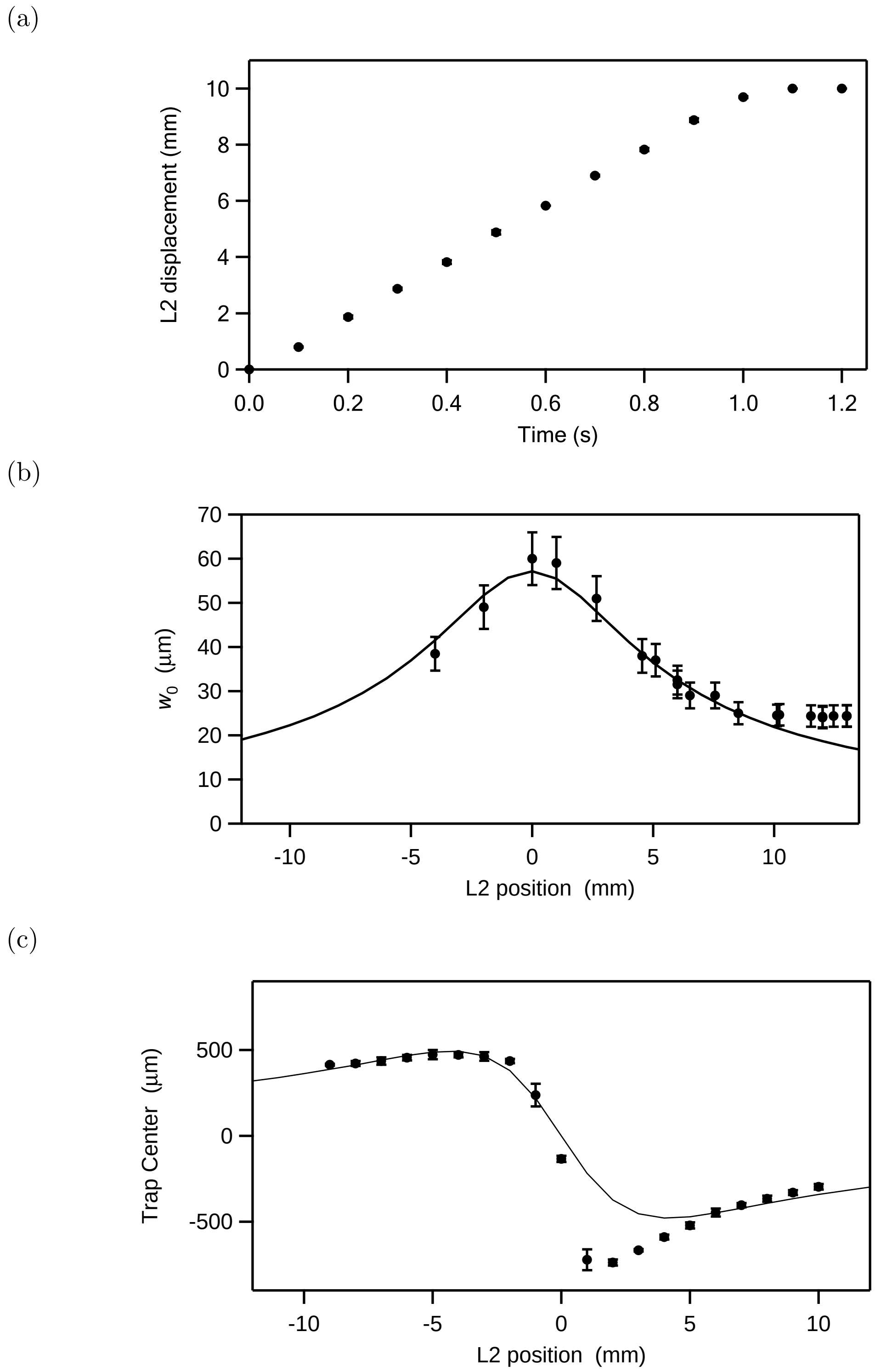

Figure 4.9: Geometrical parameters for dynamical trap compression. (a) shows the measured position of Lens 2 (L2) vs. time for 10 mm displacement at a velocity of 10 mm/s and acceleration of 60 mm/s^2. (b) shows the focused trap beam waist vs. L2 position. (c) shows the trap location displacement vs. L2 position. In Fig. (b) and (c), the solid curves are the ray tracing predictions, and the solid circles are the measurement data. The beam waists are calculated from the measured trap frequencies.

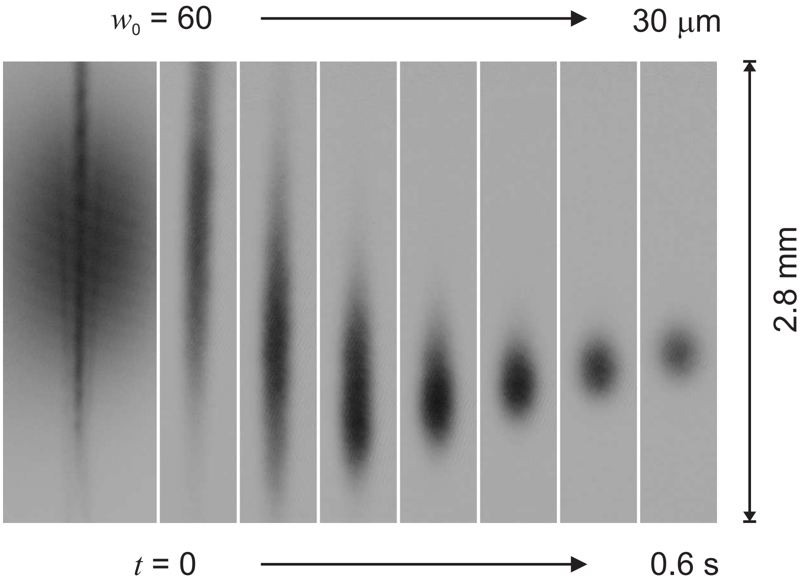

Figure 4.10: Fluorescence images of trap loading and dynamical trap compression. A high power CO_2 laser is weakly focused to form a large volume dipole trap overlapping with the MOT. When the MOT is turned off, the trap is quickly compressed. The trap compression occurs in 600 ms, with a compression factor of 16. Note that, during the compression, a very efficient cooling density enhancement is observed. In order to reduce the optical density upon probing, during compressions, the cloud is allow to expand for longer times before probing.

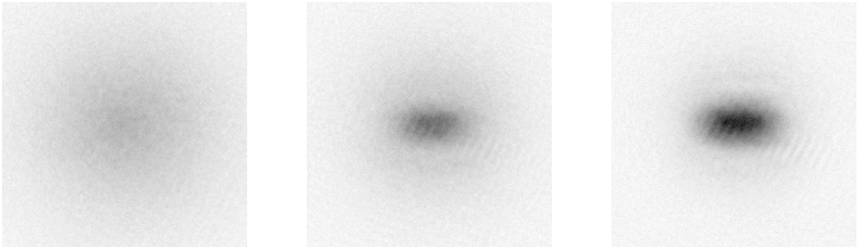

Figure 4.11: Growth of BEC in the single-focused trap vs. final CO_2 laser power. At lowest final power, 40 mW, a mostly pure condensate of 300,000 atoms is created in the optical trap.

by a 70 W CO_2 laser focused to a waist of 60 μm. Up to 3.7×10^7 atoms are loaded into the optical trap, at a density of 4×10^{13} cm^{-3}. Once the atoms are loaded into the trap, the effectiveness of the evaporative cooling is determined by the ratio of elastic collision within trapped atoms versus other bad collisions such as collisions with untrapped background residual gas molecules. It is therefore important to achieve high elastic collision rate in a short time. In order to accomplish that, the trap is compressed immediately after loading by smoothly changing the laser focus to a final waist of 30 - 26 μm in less than 1 s. The images of clouds under compression is shown in Fig. 4.10. Given the trap volume $V \propto w_0^4$, our trap volume is compressed by a factor of 16 over 600 ms. To simultaneously force evaporation, the laser power is ramped down during the compression. After 1.8 s of forced evaporation and at final power of 40 mW, a mostly pure condensate containing up to 3×10^5 atoms is created. The loading parameters of this trap are listed in the last column of Table 4.1, and images showing growth of condensates in this trap are illustrated in Fig. 4.11. This technique not only retains the simplicity and speed of our previous methods, but also produces condensates 10 times larger than the cross and 1D lattice traps.

We have also studied the evaporation dynamics for different trap compression and CO_2 power ramping timing schemes. Fig. 4.12 shows a typical chosen ramp of laser power and compression vs. time. In this particular evaporation trajectory, the evaporation data are presented in Fig. 4.13 to Fig. 4.14. In Fig. 4.13, we find that the compression increases the elastic collision rate up to $> 10^4$ s^{-1} in less than 100 ms. In Fig. 4.14 the phase space density (PSD) is observed to increase by more than two orders of magnitude during this compression, leading to a value of the PSD, $\Lambda \simeq 1/30$. In the meantime the number of atoms is only reduced by less than one order of magnitude. This is a very favorable condition for achieving quantum degeneracy via subsequent forced evaporation.

The figure of merit for an evaporation trajectory is the increase of the PSD per particle loss. To better characterize the efficiency of this trajectory, we plot both the temperature and the PSD against the number of atoms. In Fig. 4.15.a, we see that the temperature follows a simple power law with the number of atoms, $T \propto N^\gamma$ after initial compression. The value of γ is measured to be 2.1, and this value stays constant during forced evaporation

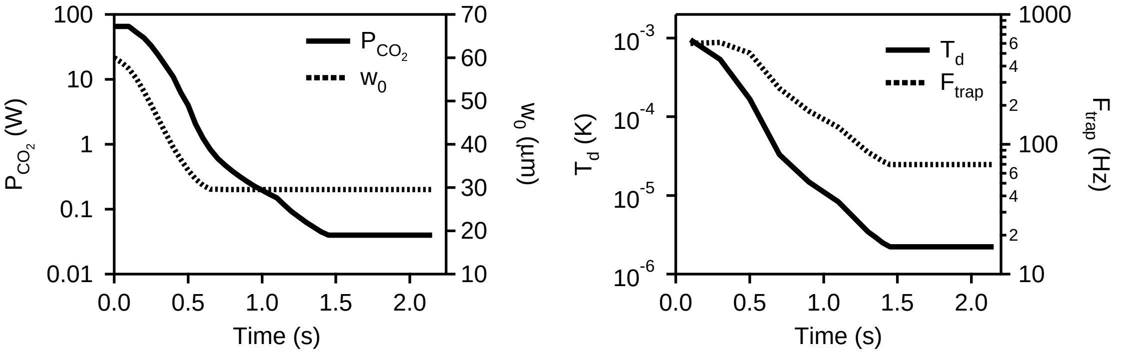

Figure 4.12: CO_2 laser power and beam waist vs. time. An evaporation trajectory can be tailored by varying the ramp of CO_2 laser power (P_{CO_2}) and beam waist (w_0). The left plot shows a typical ramp, and the right plot shows the corresponding trap depth (T_D) and mean trap frequency (F_{trap}).

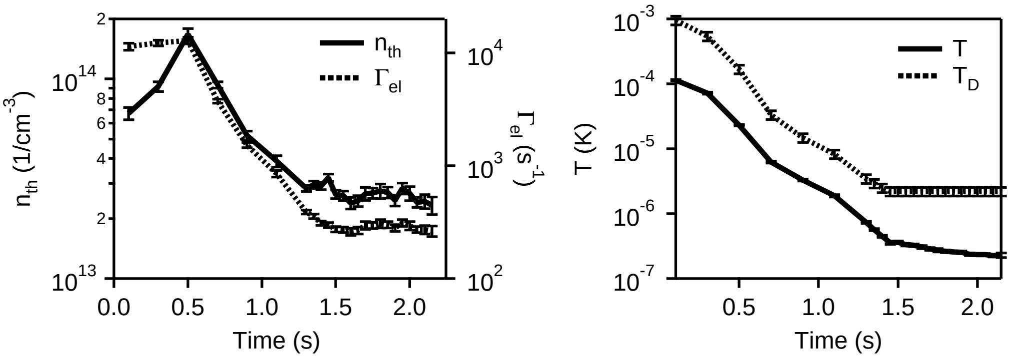

Figure 4.13: Density and elastic scattering rate vs. time. (Left) The trap compression leads to thermal cloud density (n_{th}), which further leads to high elastic collision rate (Γ_{el}) and efficient evaporative cooling. (Right) In the meantime, the fast dynamics enables a cloud to reach thermal equilibrium very quickly; temperature of the cloud basically follows the trap depth with a scaling factor $\eta = T_D/T$, where $\eta \sim 10$. As can be seen The trapping power stop ramp at 1.45 s, and without further ramping down the power, the temperature quickly reaches a plateau.

(a)

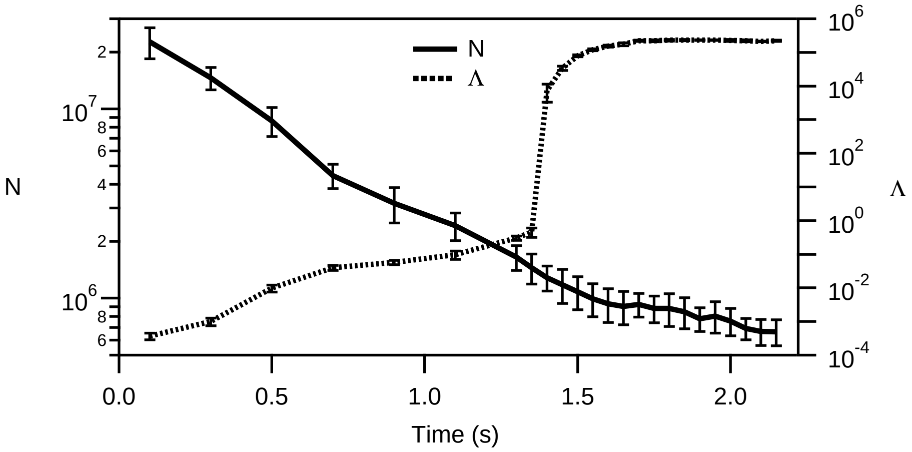

Figure 4.14: Number (N) and phase space density (PSD, Λ) vs. time. The PSD increases sharply from 10^{-4} to 5×10^{-2} in the first 600 ms during which the trap compression and evaporation are taken place simultaneously. Condensate starts to appear at 1.5 s, and the number of Bose condensed atoms quickly reach a plateau of $\leq 300,000$ atoms at 1.8 s. Here, by definition, the PSD equals to the number of condensed atoms after the condensate emerges.

until the end of the power ramp. In Fig. 4.15.b, the PSD (Λ) also follows a simple power law relationship with the number of atoms, or $\Lambda \propto N^{\rho}$. In the first regime where the elastic collision rate is $> 10^4$ s^{-1}, the increase of PSD does not cause much loss of particles, and the exponent $\rho_1 = -5.2$, which is close to the theoretical limit of a simple ergodical evaporation model with $\rho = 1 - \gamma(\xi + 3/2) = -5.3$, where $\xi = 3/2$ for 3D harmonic traps [107, 59, 24]. After the compression is finished, $\rho = -2.8$, which is somewhat smaller.

Our studies show that while the evaporation trajectory varies depending on the chosen compression and power ramping scheme, evaporative cooling is relatively robust, and the final number of Bose condensed atoms appeared to be relatively constant. The typical number of condensed atoms is $\sim 1\%$ of that initially loaded in the trap.

To summarize this chapter, we have extended the all-optical trapping technique to two new trap geometries: a large-period 1D lattice and a large volume single-focus trap. The common feature of the three trap geometries (including cross trap) are that they all achieve efficient loading and tight confinement. These two conditions lead to highest spatial densities ($> 10^{14}$ cm^{-3}) and high elastic collision rates ($> 10^4$ s^{-1}), which further lead to efficient evaporation with a typical evaporation time of less than 2 sec. In the 1D lattice geometry,

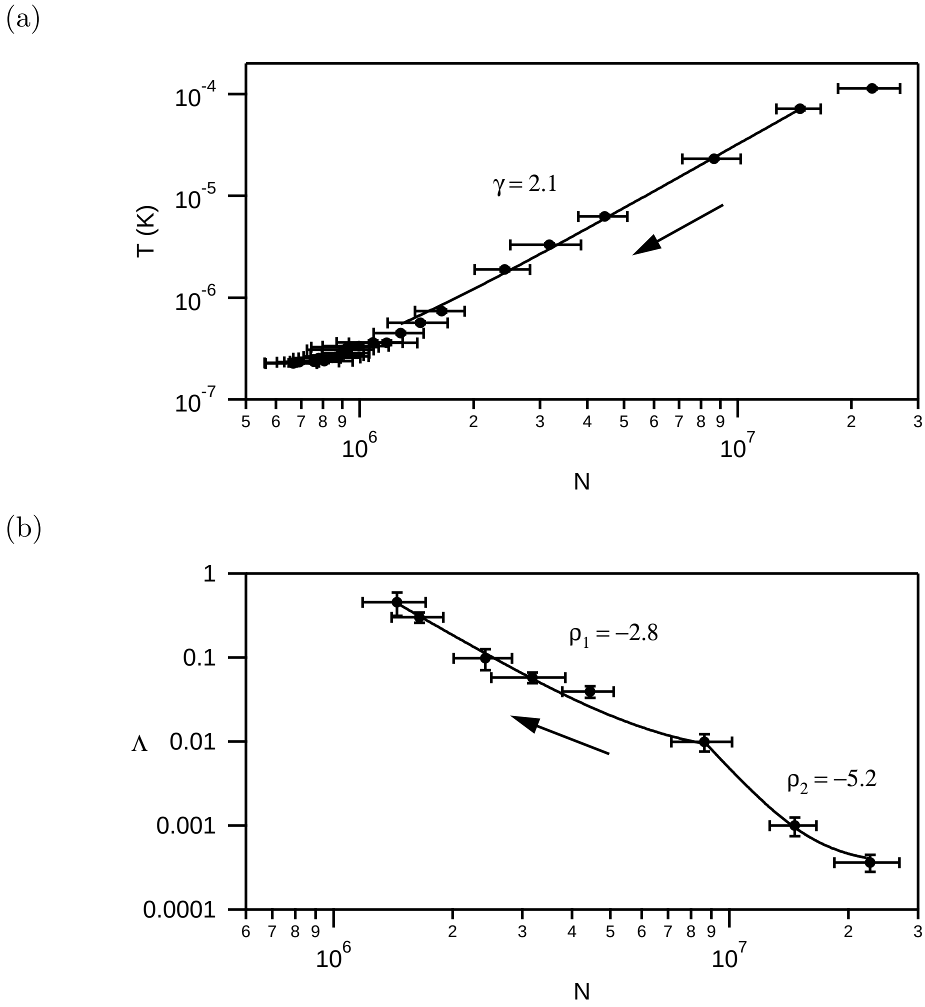

Figure 4.15: Number and phase space density (PSD) vs. number of atoms. (a) Fit the trajectory with a power law model, $T = N^{\gamma}$, we find $\gamma = 2.1$. (b) Similarly, fit the trajectory with $\Lambda = N^{\rho}$, we find the dynamics fall into two parameter regimes, $\rho = -5.2$ and $\rho_2 = -2.8$. Both arrows indicate the direction of time. Note that the error bars for the temperature are too small to be resolved here.

interference between two independently trapped condensates are observed.

CHAPTER V

SPINOR CONDENSATE THEORY

Atomic Bose-Einstein condensates with internal spin degrees of freedom, so-called spinor condensates, offer a new form of coherent matter with complex internal quantum structures. Spinor condensates exhibit rich quantum dynamics due to the vector properties of the condensate order parameter and the nonlinear spin-spin interactions.

Most current experiments employ magnetic trapping techniques in which the spin degree of freedom is frozen, and BEC experiments in this type of trap mostly involve only one spin component. Therefore, the order parameter of a one-component condensate is a scalar, and its dynamics are restricted to the motional degrees of freedom, described by the scalar Gross-Pitaevskii equation given in Eq. 1.1.

Stimulated by the early experiments by the JILA and MIT groups, and by the theoretical work by Ho [39] and Ohmi and Machida [40], spinor condensates have been the subject of many studies. Early experimental investigations of multi-component condensates have been explored by utilizing two coupled hyperfine states in ^{87}Rb [108, 109, 25, 110], and by $F = 1$ spinor condensates of Na by transferring spin polarized BEC made in magnetic traps into far-off resonant optical traps [35]. The MIT group subsequently studied the ground state properties of the spinor condensates and observed ground state domain structures [42], metastable domains [52], and quantum spin tunneling [53].

The progress of spinor condensate theories is also impressive, and theoretical work has covered ground state structure [39, 40, 111, 54, 112], quantum/coherent spin mixing [54, 113, 114, 115, 116, 117], spinor vortices [39, 40, 118], spin textures and domains [42, 119], spin squeezing and entanglement [120, 121], and many other topics.

Here we focus on spin-1 condensates composed of the three spin components, $m_F = 0, \pm 1$ of the $F = 1$ hyperfine ground state (hereafter, denoted as $m_{0,\pm 1}$ states). At the microscopic level, the interactions in spinor Bose gases are determined by two-body, s-wave collisions.

The mean-field interaction energy is $V(r) = \delta(r)(c_0 + c_2\vec{F}_a \cdot \vec{F}_b)$ [39, 40], where r is the distance between two atoms a and b, and c_0 and c_2 characterize the strength of the scalar and spin-dependent interactions respectively. These two mean-field interaction coefficients, c_0 and c_2, are simple functions of the scattering lengths $a_{F=0}$ and $a_{F=2}$.

For the $F = 1$ hyperfine spinor in ^{87}Rb, the spin-dependent mean-field energy $|c_2|n$ is only 200 pK [55, 56] for typical densities, $n \sim 10^{14}$ cm^{-3}, which is much smaller than both the scalar mean-field energy and the estimated temperature of the gas, $\sim$ 50 nK. Nonetheless, the small spin-dependent mean field couplings are non-negligible and lead to qualitatively different ground state structures depending on the sign of c_2, being ferromagnetic ($c_2 < 0$) for ^{87}Rb [55, 56, 44, 45] or anti-ferromagnetic ($c_2 > 0$) for ^{23}Na [42, 122]. Moreover, these spinor interactions yield a rich variety of coherent and incoherent phenomena including coherent spinor mixing, spin squeezing and entanglement [54, 120], spin domain formation, and spinor vortices.

In this chapter, the microscopic theory for spinor condensates will be briefly reviewed. The theoretical approach in this chapter follows closely to ref. [39, 123, 54].

5.1 Microscopic picture

The atomic interactions in spinor condensates are dominated by two-body s-wave collisions. The microscopic picture of an ultracold collision of two identical bosonic spinors is illustrated in Fig. 5.1. When two atoms approach each other, their spins will temporarily couple together to form a total spin, and the two atomic spins precess around this total spin during the collision. After the collision, the two spins decouple and the atoms move away from each other. For two identical spin-f particles, the total spin is given by $\vec{\mathbf{F}} = \vec{\mathbf{f}}_1 + \vec{\mathbf{f}}_2$, and the allowed total spins are $F = 2f, 2f-1, \cdots, 0$. However, due to the symmetry (anti-symmetry) required by identical bosons (fermions), only $F =$ even (odd) channels are allowed for bosons (fermions), when the total spatial wavefunction of the two atoms is symmetric. Here we focus on spin-1 condensates, thus the allowed collision channels are $F = 2, 0$, and two atomic parameters are required to describe the interactions, i.e., s-wave scattering lengths, $a_{F=2}$ and $a_{F=0}$ for total spin 2 and 0 channels.

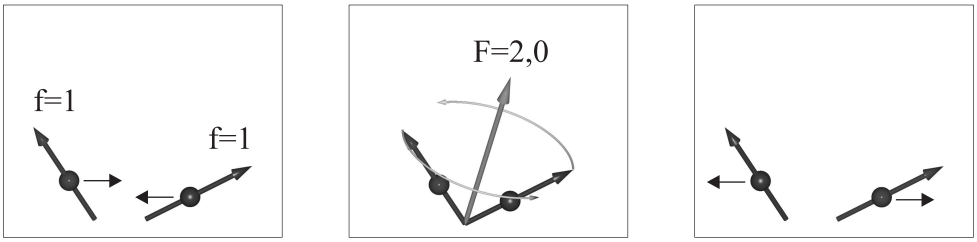

Figure 5.1: Intuitive picture of atomic interactions in spinor condensates: binary collision of spin-1 bosons. (Left) Two spin-1 bosons approach each other. (Center) The atomic spin of two bosons couple to form a total spin, and then the bosons precess around this total spin during the collision. The total spin can be $F = 2, 0$. (Right) Two bosons break apart after collision is finished.

By projecting the joint space of two spin-1 bosons, $\sum_{m_f} |f = 1, m_f\rangle \otimes \sum_{m_f} |f = 1, m_f\rangle$, to the joint space of the irreducible total spin spaces, $\sum_{m_F} |F = 0, m_F\rangle \otimes \sum_{m_F} |F = 2, m_F\rangle$, the binary interaction can be decomposed into contributions from the different total spin channels,

$$V(\vec{r}_1 - \vec{r}_2) = \delta(\vec{r}_1 - \vec{r}_2) \sum_{F=0}^{2f} g_F \mathbf{P}_F. \tag{5.1}$$

The coupling strength g_F is

$$g_F = \frac{4\pi\hbar^2 a_F}{m}, \tag{5.2}$$

where a_F is the s-wave scattering length for total spin-F channel, and m is the atomic mass. The projection operator P_F is

$$\mathbf{P}_F \equiv \sum_{m_F=-F}^{F} |F, m_F\rangle\langle F, m_F|. \tag{5.3}$$

For identical bosons, the allowed total spins are $F = even$ (see Appendix B), and the projection operators satisfy the following closure relationship:

$$\mathbf{1} = \sum_{F=0,even}^{2f} \mathbf{P}_F = \mathbf{P}_0 + \mathbf{P}_2 + \cdots . \tag{5.4}$$

Meanwhile, the spin-spin coupling of two spin-f bosons can be found using the identity:

$$\vec{\mathbf{f}}_1 \cdot \vec{\mathbf{f}}_2 = \frac{\mathbf{F}^2 - \mathbf{f}_1^2 - \mathbf{f}_2^2}{2} = \frac{F(F+1) - 2f(f+1)}{2}. \tag{5.5}$$

Here $\vec{\mathbf{f}}_1$, $\vec{\mathbf{f}}_2$, and $\vec{\mathbf{F}}$ are dimensionless.

Applying the identity operator leads to

$$\vec{\mathbf{f}}_1 \cdot \vec{\mathbf{f}}_2 = (\vec{\mathbf{f}}_1 \cdot \vec{\mathbf{f}}_2)\mathbf{1} = \sum_f \vec{\mathbf{f}}_1 \cdot \vec{\mathbf{f}}_2 \mathbf{P}_F = \sum_F \lambda_F \mathbf{P}_F, \tag{5.6}$$

where $\lambda_F = \frac{F(F+1)-2f(f+1)}{2}$. For spin-1 condensates,

$$\mathbf{1} = \mathbf{P}_0 + \mathbf{P}_2, \tag{5.7}$$

and

$$\vec{\mathbf{f}}_1 \cdot \vec{\mathbf{f}}_2 = \mathbf{P}_2 - 2\mathbf{P}_0. \tag{5.8}$$

By the aid of the above two identities and Eq. (5.1), the binary interactions for identical spin-1 bosons can be expressed as

$$\begin{aligned} V(\vec{r}_1 - \vec{r}_2) &= \delta(\vec{r}_1 - \vec{r}_2) \sum_{f=0}^{2} g_f \mathbf{P}_f && (5.9a) \\ &= \delta(\vec{r}_1 - \vec{r}_2)(g_0 \mathbf{P}_0 + g_2 \mathbf{P}_2) && (5.9b) \\ &= \delta(\vec{r}_1 - \vec{r}_2)(c_0(\mathbf{P}_0 + \mathbf{P}_2) + c_2(\mathbf{P}_2 - 2\mathbf{P}_0)) && (5.9c) \\ &= \delta(\vec{r}_1 - \vec{r}_2)(c_0 + c_2 \vec{\mathbf{f}}_1 \cdot \vec{\mathbf{f}}_2). && (5.9d) \end{aligned}$$

Here c_0 and c_2 are density- and spin-dependent interactions, c_0 and c_2, with

$$c_0 = \frac{g_0 + 2g_2}{3} = \frac{4\pi\hbar^2}{m}\bar{a}, \tag{5.10}$$

and

$$c_2 = \frac{g_2 - g_0}{3} = \frac{4\pi\hbar^2}{m}\frac{\Delta a}{3}. \tag{5.11}$$

In the above expressions $\bar{a} = (a_{F=0} + 2a_{F=2})/3$ is the mean s-wave scattering length, and $\Delta a = a_{F=2} - a_{F=0}$ is the scattering length difference.

The total Hamiltonian for a spin-1 condensate is

$$\begin{aligned} H &= \sum_{i=1}^{N} \frac{p_i^2}{2m} + U(r_i) + \sum_{i<j} V(\vec{r}_i - \vec{r}_j) && (5.12a) \\ &= \sum_{i=1}^{N} \frac{p_i^2}{2m} + U(r_i) + \sum_{i<j} \delta(r_i - r_j)(c_0 + c_2 \vec{\mathbf{f}}_i \cdot \vec{\mathbf{f}}_j). && (5.12b) \end{aligned}$$

Here, $U(\vec{r})$ is the total external potentials, which includes the optical trapping potential and the Zeeman energy due to external magnetic fields.

An immediate important feature of a spinor system is that the spin-spin interaction is invariant under rotation in spin space. This rotation symmetry leads to a vectorial order

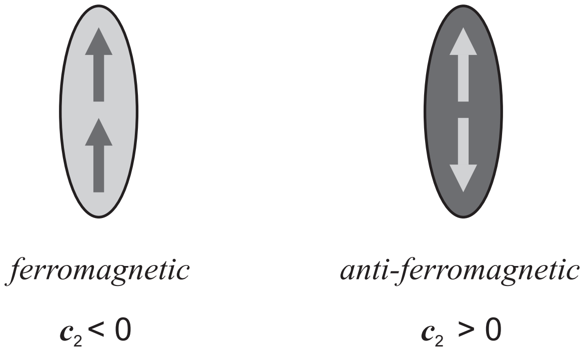

Figure 5.2: Magnetic nature of spin-1 condensates.

parameter [39]. Secondly, although typically $|c_2| \ll c_0$ due to that $a_{F=2} \simeq a_{F=0}$ [56, 42], it is responsible for coupling different Zeeman states. Indeed, it is this coupling that leads to spinor dynamics such as spin mixing and spin domain formation. Finally, the sign of c_2 determines the ground state structure, as well as the dynamical properties of the spinor condensates.

As illustrated in Fig. 5.2, spin-1 condensates are divided into two categories depending on the sign of c_2. When $c_2 < 0$, maximizing $\vec{\mathbf{f}}_i \cdot \vec{\mathbf{f}}_j$ and consequently minimizing H requires that spinors are all polarized in the same direction, which is equivalent to $|f = 1, m_f = 1\rangle$ state under spin rotation. Therefore, it is said to be ferromagnetic. In contrast, when $c_2 > 0$, the ground state is said to be anti-ferromagnetic, since spinors align in opposite directions, which is a singlet state [54, 39, 111].

5.2 Second Quantized Hamiltonian for Spin-1 Condensates

It is natural to describe this many-body system in the second quantized formalism. Additionally, as will be seen immediately, simplification of spinor dynamics due to rotational symmetry can be better appreciated in the second quantized formalism. In terms of the field operators of three Zeeman states, $(\mathbf{\Psi}_1, \mathbf{\Psi}_0, \mathbf{\Psi}_{-1})$, the most general spin-1 Hamiltonian is given by [39][40]

$$\begin{aligned}\mathbf{H} &= \int \mathrm{d}^3r \mathbf{\Psi}_i^\dagger(\vec{r})(-\frac{\hbar^2\nabla^2}{2m}\delta_{ij} + U_{ij}(\vec{r}))\mathbf{\Psi}_j(\vec{r}) \\ &\quad + \frac{g_{ij,kl}}{2}\int \mathrm{d}^3r_1\mathrm{d}^3r_2\mathbf{\Psi}_i^\dagger(\vec{r}_1)\mathbf{\Psi}_j^\dagger(\vec{r}_2)\mathbf{\Psi}_k(\vec{r}_2)\mathbf{\Psi}_l(\vec{r}_1)\delta(\vec{r}_1 - \vec{r}_2). \qquad (5.13)\end{aligned}$$

Here, δ_{ij} is the Kronecker delta function, and U_{ij}'s are the external potentials. The U_{ij}'s allow nonzero coupling between different Zeeman states, such as the coupling between two Zeeman states by radio frequency (RF) waves. The indices $\{i, j, k, l\}$ run through all three Zeeman states, $\{1, 0, -1\}$, and the sum over repeated indices is implied. The coefficients $g_{ij,kl}$ are the coupling constants for collision channels $\{k, l\} \to \{i, j\}$, and in the most general case, there are $(2f + 1)^4 = 3^4 = 81$ $g_{ij,kl}$'s for spin-1 condensates. This large number of independent g's, however, can be greatly reduced as the collisions are symmetric under exchange of particles ($g_{ij,kl} = g_{ji,kl}$) and time-reversal ($g_{ij,kl} = g_{kl,ij}$). This value is then reduced to $(l^2 + l)(l^2 + l + 2)/8$, where $l = 2f + 1$ (see Appendix B). For spin-1 systems, the number of independent g's is 21, which is still a large number. However, due to the spin rotational symmetry, the number of free parameters can be ultimately reduced to only two atomic parameters, the s-wave scattering lengths for total spin-2 and spin-0 collision channels, $a_{F=2}$ and $a_{F=0}$. Recall the results from the last section, simply express Eq. (5.12) in the 2nd quantized format, and Eq. (5.13) is immediately reduced to

$$\begin{aligned}
\mathbf{H} &= \int \mathrm{d}^3 r \boldsymbol{\Psi}_i^\dagger(\vec{r})[-\frac{\hbar^2\nabla^2}{2m}\delta_{ij} + U_{ij}(\vec{r})]\boldsymbol{\Psi}_j(\vec{r}) \\
&\quad +\frac{c_0}{2}\int \mathrm{d}^3 r \boldsymbol{\Psi}_i^\dagger(\vec{r})\boldsymbol{\Psi}_j^\dagger(\vec{r})\boldsymbol{\Psi}_j(\vec{r})\boldsymbol{\Psi}_i(\vec{r}) \\
&\quad +\frac{c_2}{2}\int \mathrm{d}^3 r \boldsymbol{\Psi}_i^\dagger(\vec{r})\boldsymbol{\Psi}_j^\dagger(\vec{r})\vec{\mathbf{f}}_{jk}\cdot\vec{\mathbf{f}}_{il}\boldsymbol{\Psi}_k(\vec{r})\boldsymbol{\Psi}_l(\vec{r}). \qquad (5.14)
\end{aligned}$$

Here, c_0 and c_2 are the density- and spin-dependent coupling strengthes for spinors defined in Eq. (5.10) and (5.11), and $\vec{\mathbf{f}}_{jk} \cdot \vec{\mathbf{f}}_{il} = (\mathbf{f}_\alpha)_{jk}(\mathbf{f}_\alpha)_{il}$, where $(\mathbf{f}_\alpha)_{jk}$ are the matrix elements for three Cartesian, traceless spin-1 Pauli matrices,

$$\mathbf{f}_x = \frac{1}{\sqrt{2}}\begin{bmatrix} 0 & 1 & 0 \\ 1 & 0 & 1 \\ 0 & 1 & 0 \end{bmatrix}, \mathbf{f}_y = \frac{i}{\sqrt{2}}\begin{bmatrix} 0 & -1 & 0 \\ 1 & 0 & -1 \\ 0 & 1 & 0 \end{bmatrix}, \mathbf{f}_z = \begin{bmatrix} 1 & 0 & 0 \\ 0 & 0 & 0 \\ 0 & 0 & -1 \end{bmatrix}. \qquad (5.15)$$

The second and third integrals in Eq. (5.14) represent the nonlinear atom-atom interactions, and they constitute the interaction Hamiltonian,

$$\mathbf{H}_{int} = \frac{1}{2}\int \mathrm{d}^3 r\{c_0(\boldsymbol{\Psi}_i^\dagger\boldsymbol{\Psi}_j^\dagger\boldsymbol{\Psi}_j\boldsymbol{\Psi}_i) + c_2(\boldsymbol{\Psi}_i^\dagger\boldsymbol{\Psi}_j^\dagger(\vec{\mathbf{f}}_{jk}\cdot\vec{\mathbf{f}}_{il})\boldsymbol{\Psi}_k\boldsymbol{\Psi}_l)\}. \qquad (5.16)$$

Table 5.1: Table of two-body interaction strengths. Upper table lists the intra- and inter-state particle exchange collisions. Lower table lists the spin changing or spin mixing collisions.

$g_{ij,ji}$	m_1	m_0	m_{-1}
m_1	$c_0 + c_2$	$\frac{c_0+c_2}{2}$	$\frac{c_0-c_2}{2}$
m_0	$\frac{c_0+c_2}{2}$	c_0	$\frac{c_0+c_2}{2}$
m_{-1}	$\frac{c_0-c_2}{2}$	$\frac{c_0+c_2}{2}$	$c_0 + c_2$

$g_{1-1,00}$	c_2
$g_{00,1-1}$	c_2

We can express this interaction Hamiltonian in terms of three spin components explicitly (see Appendix C),

$$\begin{aligned}\mathbf{H}_{int} &= \frac{1}{2}\int \mathrm{d}^3r\{(c_0+c_2)\mathbf{\Psi}_1^\dagger\mathbf{\Psi}_1^\dagger\mathbf{\Psi}_1\mathbf{\Psi}_1 + c_0\mathbf{\Psi}_0^\dagger\mathbf{\Psi}_0^\dagger\mathbf{\Psi}_0\mathbf{\Psi}_0 + (c_0+c_2)\mathbf{\Psi}_{-1}^\dagger\mathbf{\Psi}_{-1}^\dagger\mathbf{\Psi}_{-1}\mathbf{\Psi}_{-1} \\ &\quad +2(c_0+c_2)\mathbf{\Psi}_1^\dagger\mathbf{\Psi}_0^\dagger\mathbf{\Psi}_0\mathbf{\Psi}_1 + 2(c_0-c_2)\mathbf{\Psi}_1^\dagger\mathbf{\Psi}_{-1}^\dagger\mathbf{\Psi}_{-1}\mathbf{\Psi}_1 + 2(c_0+c_2)\mathbf{\Psi}_0^\dagger\mathbf{\Psi}_{-1}^\dagger\mathbf{\Psi}_{-1}\mathbf{\Psi}_0 \\ &\quad +2c_2\mathbf{\Psi}_{-1}^\dagger\mathbf{\Psi}_1^\dagger\mathbf{\Psi}_0\mathbf{\Psi}_0 + 2c_2\mathbf{\Psi}_0^\dagger\mathbf{\Psi}_0^\dagger\mathbf{\Psi}_{-1}\mathbf{\Psi}_1\}. \qquad (5.17)\end{aligned}$$

In this interaction Hamiltonian, the first three terms represent the intra-state collisions, or the self-scattering, the following three terms represent the inter-state collisions or the cross-scattering, and the last two terms stand for the spin mixing, which provide a way to relax to the spinor ground state under the presence of dissipation when the initial spin populations are not in their minimal energy configuration. The coupling strength coefficients are tabulated in Table 5.1.

5.3 Spinors In Magnetic Fields

Is is important to understand the interactions between a spinor condensate and external magnetic fields. Since spin interactions are magnetic interactions, external magnetic fields will compete with, or even dominate the internal spin interactions. First, an external magnetic field will break rotational symmetry along the axis defined by that field [39]. A homogeneous field will change the total Zeeman energy of a spinor condensate and subsequently alter its ground state spin configuration. A homogeneous field will also cause spinors to undergo Larmor precessions around the z axis, which results in fast rotation of spinor's phase and affects phase sensitive dynamics. An inhomogeneous field will exert magnetic forces on spinors and can cause phase separation of different spin states. In addition, field inhomogeneities will give rise to spatial dephasing of coherent spinor dynamics. Finally, AC magnetic fields can cause diabatic spin flips in a low bias field.

In a static B field, the Zeeman energy of the spin states is given by

$$E_Z = \begin{bmatrix} E_1 & 0 & 0 \\ 0 & E_0 & 0 \\ 0 & 0 & E_{-1} \end{bmatrix} \tag{5.18}$$

Typically, the spin-dependent interactions are $E_{\text{int}}/h < 10$ Hz for a typical density of 10^{14} cm^{-3}. In principle, to observe spinor dynamics, the external Zeeman effects introduced by the external field should be much less than 10 Hz, which requires zeroing the B field to micro-Gauss regime. However, due to the conservation of magnetization, which will be explained in the next few paragraphs, one can still observe interesting spinor dynamics in the milli-Gauss to Gauss regime.

The mean-field global ground state for ferromagnetic (anti-ferromagnetic) spinors is $|F = 1, m_F = 1\rangle$ ($|F = 1, m_F = 0\rangle$) state [39]. If a spinor condensate forms with a non-equilibrium spin configuration and a net magnetization, $M = \rho_1 - \rho_{-1}$, where $\rho_{\pm 1}$ are the fractional population of $m_F = \pm 1$ states, then the condensate can only relax to its global ground state via spin non-conserved collisions. This is, however, not allowed because the fundamental atomic collisions conserve the total spin (angular momentum), which is clearly shown in Eq. (5.17). Therefore, in a spin-independent trap, the total magnetization of a spinor condensate should be a conserved quantity.

The non-spin mixing collisions in the interacting Hamiltonian do not cause a change of populations in different spin states, and therefore will not change the Zeeman energy of the condensate in a B field. In contrast, spin changing collisions (spin mixing) will cause change of spin populations and the total magnetic energy. The spin-changing collisions read

$$2|m_F = 0\rangle \longleftrightarrow |m_F = 1\rangle + |m_F = -1\rangle. \tag{5.19}$$

The change of magnetic energy per particle in this reaction process going to the right is $\delta = (E_1 + E_{-1} - 2E_0)/2 > 0$. This energy difference therefore energetically favors the direction of the arrow going to the left. Due to the conservation of magnetization, δ essentially cancels the linear Zeeman effect, $\eta = (E_{-1} - E_1)/2$, resulting in a much smaller Zeeman effect. According to the Breit-Rabi formula, or Eq. (2.1), $\delta \simeq g_J^2 \mu_\mathrm{B}^2 B^2/16E_\mathrm{hfs}$, where g_J, μ_B, B, and E_hfs are the Landé g-factor for electron, Bohr magneton, magnetic field, and hyperfine splitting. For ^{87}Rb $\delta \simeq B^2 \times 71.6$ Hz/G^2, and δ vs. B field is plotted in Fig. 5.3(a). In a field between 0.001 and 1 G, δ is 4 to 6 orders of magnitude smaller than η as shown in Fig. 5.2(b). In a typical field of 100 mG, $\delta \simeq$0.7 Hz, which is small compared to the spinor energy ($\lesssim$ 10 Hz). Indeed, it is the conservation of magnetization that leads to cancellation of linear Zeeman shifts and allows observation of spinor dynamics in a field regime much higher than a few micro-Gauss.

5.4 Coupled Gross-Pitaevskii equations for spin-1 condensates

The dynamics of spinor condensates are governed by the coupled spin-1 Gross-Pitaevskii (GP) equation for the three spin states. These coupled equations of motion for spin-1 fields can be derived by the Heisenberg equation of motion,

$$i\hbar\frac{\partial \mathbf{\Psi}_\alpha}{\partial t} = [\mathbf{\Psi}_\alpha, \mathbf{H}],\ \alpha = 1, 0, -1. \tag{5.20}$$

Substituting Eq. (5.14) into Eq. (5.20), and after some calculation, the coupled equations of motion for spin-1 fields are given by

$$i\hbar\frac{\partial \mathbf{\Psi}_\alpha}{\partial t} = (\frac{-\hbar^2}{2m}\nabla^2 + U_\alpha)\mathbf{\Psi}_\alpha + c_0\mathbf{\Psi}_i^\dagger\mathbf{\Psi}_i\mathbf{\Psi}_\alpha + c_2\mathbf{\Psi}_j^\dagger\vec{\mathbf{F}}_{\alpha k}\cdot\vec{\mathbf{F}}_{jl}\mathbf{\Psi}_l\mathbf{\Psi}_k,\ \alpha = 1, 0, -1. \tag{5.21}$$

Here U_α is the external potentials including the trapping potential and the Zeeman energies, and we assume U_α is diagonal.

In the mean-field limit in which the ground state is macroscopically occupied, one can replace three spinor field operators with a 3-component vectorial order parameter for this ground state and ignore the contribution from excited states (due to quantum fluctuations),

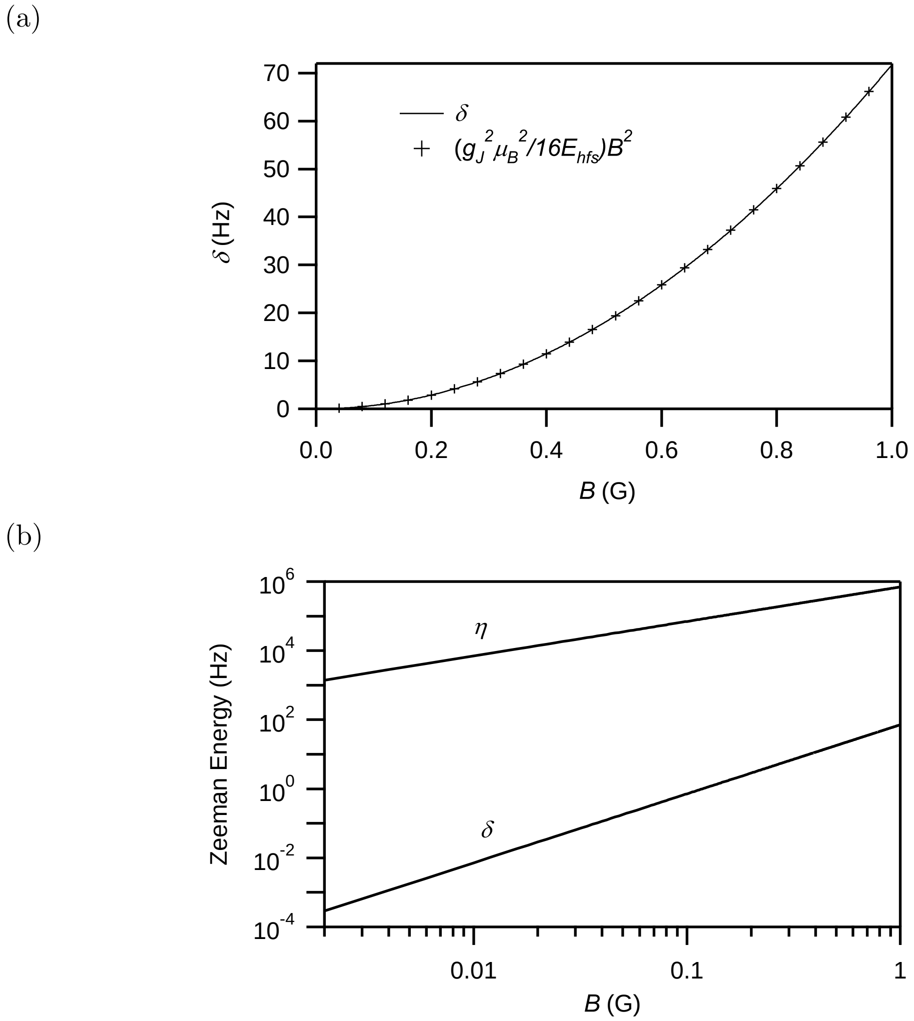

Figure 5.3: Zeeman effects in low fields. (a) Quadratic Zeeman effect vs. B. In low fields, δ is proportional to B^2. (b) Comparison of linear and quadratic Zeeman effects in low fields.

i.e.,

$$(\psi_1, \psi_0, \psi_{-1})^T = \langle(\mathbf{\Psi}_1, \mathbf{\Psi}_0, \mathbf{\Psi}_{-1})^T\rangle, \tag{5.22a}$$

$$(\psi_1^*, \psi_0^*, \psi_{-1}^*)^T = \langle(\mathbf{\Psi}_1^\dagger, \mathbf{\Psi}_0^\dagger, \mathbf{\Psi}_{-1}^\dagger)^T\rangle. \tag{5.22b}$$

Then the three coupled Gross-Pitaevskii equations for spin-1 order parameters are given by

$$i\hbar\frac{\partial\psi_1}{\partial t} = \mathcal{L}_1\psi_1 + c_0 n\psi_1 + c_2(n_1 + n_0 - n_{-1})\psi_1 + c_2\psi_{-1}^*\psi_0\psi_0, \tag{5.23a}$$

$$i\hbar\frac{\partial\psi_0}{\partial t} = \mathcal{L}_0\psi_0 + c_0 n\psi_0 + c_2(n_1 + n_{-1})\psi_0 + 2c_2\psi_0^*\psi_1\psi_{-1}, \tag{5.23b}$$

$$i\hbar\frac{\partial\psi_{-1}}{\partial t} = \mathcal{L}_{-1}\psi_{-1} + c_0 n\psi_{-1} + c_2(n_{-1} + n_0 - n_1)\psi_{-1} + c_2\psi_1^*\psi_0\psi_0, \tag{5.23c}$$

where $\mathcal{L}_{\pm1,0} \equiv (\frac{-\hbar^2\nabla^2}{2m} + U_{\pm1,0})$, $n = n_1 + n_0 + n_{-1}$ is the total density, and $n_i = |\psi_i|^2$ is the density for each spin component.

The penultimate term in Eq. (5.23a-c) results in the cross-phase modulation, which drives spatial dynamics that can ultimately lead to spin domain formation. The last term in Eq. (5.23a-c) represent the coherent spin mixing, which can result in oscillations of the spin populations when the spinor condensate is not in the spinor ground state. These two processes occur with the same time scale (typically < 10 Hz for ^{87}Rb), and they are both very sensitive to external magnetic fields and field gradients represented in $E_{\pm1,0}$ [42, 111, 124, 44, 45, 125, 117]. Therefore, the two dynamics are generally inseparable, and the interplay of the two processes reveal a rich coupling between the internal and external degrees of freedom of the condensate components which resulting in a variety of observed phenomena including spin mixing [42, 44, 45], spin domain formation [42], and spin textures [118, 126].

5.5 Single-Mode approximation

Although the internal and external dynamics are generally inseparable, under certain conditions they can be decoupled. In particular, when the available spin interaction energy is less than that required to create spatial spin structures in the condensates, then the external dynamics will be suppressed. This occurs when the spin healing length $\xi_s = h/\sqrt{2m\,|c_2|\,n}$

is larger than the size of the condensate. In this case, then ψ_1, ψ_0 and ψ_{-1} share the same spatial wave function and allows separation of spatial dynamics and the internal spinor dynamics. This is known as the single-mode approximation (SMA) and leads to considerable simplification of Eq. (5.23).

Under SMA, the vectorial order parameter can be written as

$$\vec{\psi}_i(\vec{r}) = \sqrt{N}\phi(\vec{r})\mathrm{e}^{-i\mu t/\hbar}\vec{\zeta}(t), \tag{5.24}$$

where N is the total number of atoms, $\phi(r)$ is the common spatial mode function, μ is the chemical potential, and $\vec{\zeta} = (\zeta_1, \zeta_0, \zeta_{-1})^T$ is the internal state vector with $|\vec{\zeta}|^2 = 1$. The mode function $\phi(\vec{r})$ satisfies the normalization condition $\int |\phi(\vec{r})|^2 \mathrm{d}^3 r = 1$, and its dynamics is determined by the spin-independent Hamiltonian, $H_s = -(\hbar^2/2m)\nabla^2 + U + c_0 n$, as discussed in ref. [54, 114, 127].

Substituting the single-mode spinor wavefunctions into the Gross-Pitaevskii equations to eliminate the spatial dynamics via $H_s\phi(\vec{r}) = \mu\phi(\vec{r})$, and integrating over coordinate space, we arrive at the coupled spinor equations,

$$i\hbar\dot{\zeta}_1 = E_1\zeta_1 + c\left[(\rho_1 + \rho_0 - \rho_{-1})\right]\zeta_1 + \zeta_0^2\zeta_{-1}^*, \tag{5.25a}$$

$$i\hbar\dot{\zeta}_0 = E_0\zeta_0 + c\left[(\rho_1 + \rho_{-1}\right]\zeta_0 + 2\zeta_1\zeta_{-1}\zeta_0^*, \tag{5.25b}$$

$$i\hbar\dot{\zeta}_{-1} = E_{-1}\zeta_{-1} + c\left[(\rho_{-1} + \rho_0 - \rho_1)\right]\zeta_{-1} + \zeta_0^2\zeta_1^*\ , \tag{5.25c}$$

where $c = c_2 N \int |\phi(\vec{r})|^4 \mathrm{d}^3 r$ is the averaged (integrated) spin mean-field for the whole condensate, and $\rho_i = |\zeta_i|^2$ is the fractional population of ith spin state.

The normalization condition, $\sum_{i=1}^{3} \rho_i = 1$, and conservation of magnetization, $M = \rho_1 - \rho_{-1}$, can be used to further simplify Eq. (5.25). Indeed, Eq. (5.25) can be reduced by transforming $\zeta_{\pm 1} \rightarrow \zeta_{\pm 1}\exp\left[-i(E_0 \mp \eta)t/\hbar\right]$ and $\zeta_0 = \zeta_0 \exp\left[-iE_0 t/\hbar\right]$ with $\zeta_i = \sqrt{\rho_i}\mathrm{e}^{-i\theta_i}$. Under the constraints and this transformation, the internal spinor dynamics take on a particularly simple form, and are determined by just two dynamical variables, $\rho_0(t)$, the fractional population of the m_0 state, and the relative phase of the spinor components

$\theta = \theta_1 + \theta_{-1} - 2\theta_0$:

$$\begin{aligned}
\dot{\rho}_0 &= \frac{2c}{\hbar}\rho_0\sqrt{(1-\rho_0)^2 - M^2}\sin\theta, && (5.26)\\
\dot{\theta} &= -\frac{2\delta}{\hbar} + \frac{2c}{\hbar}\left[(1-2\rho_0) + \frac{(1-\rho_0)(1-2\rho_0) - M^2}{\sqrt{(1-\rho_0)^2 - M^2}}\cos\theta\right], && (5.27)
\end{aligned}$$

where $\eta = (E_{-1} - E_1)/2$ and $\delta = (E_1 + E_{-1} - 2E_0)/2$ are the linear and quadratic Zeeman shifts. These two equations represent a classical nonlinear pendulum, with the total energy (Hamiltonian)

$$E = c\rho_0\left[(1-\rho_0) + \sqrt{(1-\rho_0)^2 - M^2}\cos\theta\right] + \delta(1-\rho_0). \tag{5.28}$$

It is noted that Eq. (5.26) and (5.27) can also be derived by $\dot{\rho}_0 = -(2/\hbar)\partial E/\partial\theta$ and $\dot{\theta} = (2/\hbar)\partial E/\partial\rho_0$. These coupled equations also represent a type of nonlinear Josephson oscillator and point to the equivalency of spin mixing in a spin-1 condensate to Josephson systems realized in superconductors [128] and other superfluids [46, 47, 129, 12, 109, 130, 131, 104]. The non-linearity of these equations provides a rich manifold of dynamical trajectories that can be accessed experimentally by choice of initial populations and phases of the spin components and the strength of the applied magnetic field. Experimental studies of the coherent spin mixing described here will be presented in Chapter 7.

CHAPTER VI

OBSERVATION OF SPINOR DYNAMICS IN F=1 AND F=2 BOSE CONDENSATES

In this chapter, we describe our experimental investigation of the spin dynamics and ground state properties of ^{87}Rb spinor condensates in an all-optical trap, starting with well-characterized initial conditions in a known magnetic field. We focus on the $F = 1$ case and confirm the predicted ferromagnetic behavior. We observe evidence of population oscillation between different spin states during the spin mixing and observe reduced magnetization fluctuations, pointing the way to future exploration of the underlying spin squeezing and spin entanglement predicted for the system [132]. We also create $F = 2$ spinors using a microwave excitation and measure a decay of the condensate with a time constant of 250 ms. Despite the short lifetime, spin mixing of the spin-2 condensates is observed within 50 ms.

Depending on the scattering lengths in different angular momentum channels, $F = 1$ spinor condensates can be either ferromagnetic or anti-ferromagnetic [39], and the corresponding ground state structure and dynamical properties of the two cases are very distinct. While the Na $F = 1$ spinor is anti-ferromagnetic, the ^{87}Rb F = 1 spinor is ferromagnetic in nature [55][56]. Hence, our all-optical route to BEC provides an excellent opportunity for initial exploration of ferromagnetic spinor quantum gases.

6.1 Formation of Spinor Condensates

An optical trap can be essentially spin independent for large enough detunings and is ideally suited for the studies of spinor condensates. The spin degrees of freedom are unconstrained in an optical trap, and therefore spinor condensates can naturally form in the optical trap. To observe spinor condensates, we perform time-of-flight expansion in a Stern-Gerlach type

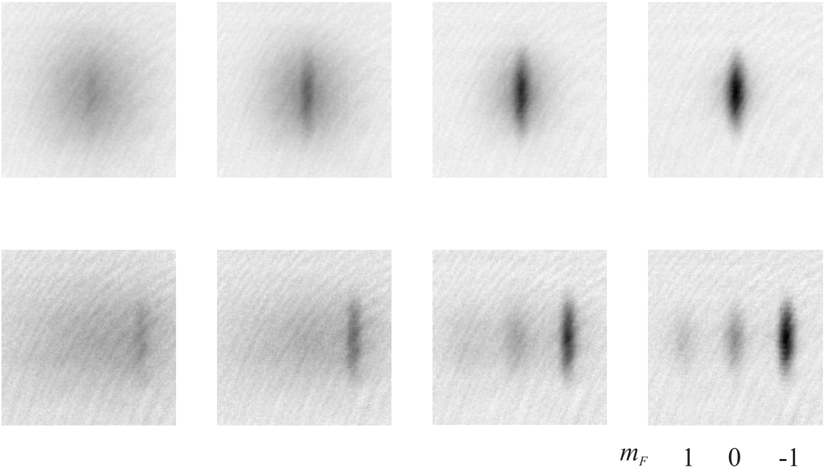

Figure 6.1: Bose-Einstein condensation of spinors. Time-of-flight absorptive images with (bottom) and without (top) Stern-Gerlach (SG) field. As seen in the bottom raw, when the final temperature is lowered (left to right), the largest spin component start to condensate first, and the smallest spin component reaches the phase transition temperature last.

gradient magnetic field. A typical result is shown in Fig. 6.1 for spin components at different temperatures. As evidenced by the images, the three spin components condense at different temperatures due to different thermal populations, with the $m_F = -1$ component condensing first, followed by the $m_F = 0$ component and lastly the $m_F = 1$. The magnetization produced in our all-optical condensates is due to the unbalanced spin populations loaded from the MOT. We have verified this by following the evaporation of all three spin states in the single focus trap. To probe each spin state individually, we first selectively excite a spin state to the $F = 2$ state using microwaves tuned to 6.834 GHz, and then absorptively probe the cloud without repump laser. For low temperatures, $T \sim T_c$, we can use a Stern-Gerlach field to separate the three spin states and simultaneously measure all three states by absorption imaging.

The evaporation data shown in Fig. 6.2 reveal that the relative total (thermal + BEC) populations of three spin states stay relatively constant over the entire evaporation. The thermal cloud is demagnetized by transferring the magnetization to the condensate [133]. This is a straightforward consequence of the Bose statistics. When the temperature is below the BEC critical temperature, atoms macroscopically occupy the ground state, leaving a "saturated" classical (thermal) gas in the excited states. The number of the atoms in the

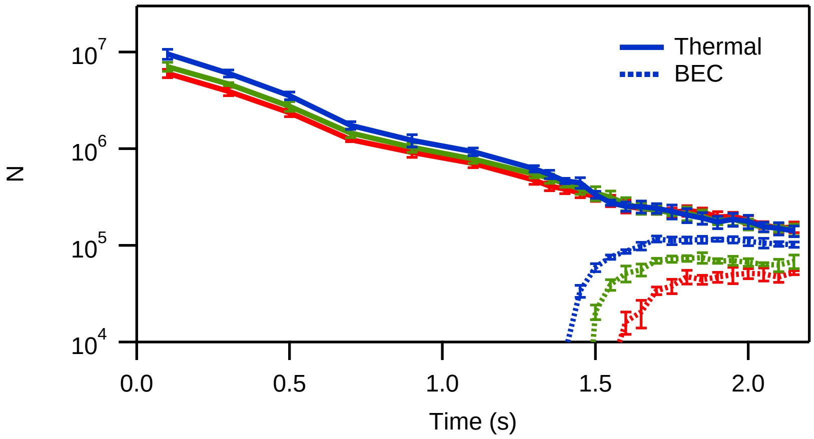

Figure 6.2: Bose-Einstein condensation of spin-1 condensate. Here the solid lines and the dotted lines represent the thermal clouds and BECs, and RGB colors represent the $m_F = 1, 0, -1$ components, respectively.

excited states is given by

$$N_{th} = 1.202 \left(\frac{k_B T}{\hbar \omega} \right)^3 .$$

When the three spin states are non-interacting or weakly interacting, the thermal atoms for three spin components will be the same, since they share the same temperature at thermal equilibrium. This equal population of thermal atoms then leads to a non-magnetized thermal gas. This is observed in Fig. 6.3 after all three spin components are Bose condensed. Theoretical studies showed that in a spinor system, interesting phenomena known as double-condensation and even multi-condensation can occur in a spin-1 system due to the conservation of magnetization [134, 135]. Observation of these phenomena will require the spinor condensate to be in the ground state spin configuration [134, 135]. However, this ground spinor population configuration is not generally observed in our loading MOT. Therefore, verification of these predicted phenomena is subject to future explorations.

We have developed techniques to control the relative spin populations of the atomic clouds. To control spin populations in spinor condensates, we apply different magnetic field gradients during the evaporation process. To create a pure condensate in the $|F = 1, m_F = 0\rangle$ state, we apply a field gradient of 28 G/cm during the final 1 s of evaporation. To create an equally mixed $m_F = -1, 0, 1$ condensate, a smaller gradient (14 G/cm) is applied. Evaporation of spinors through BEC critical temperatures in different magnetic

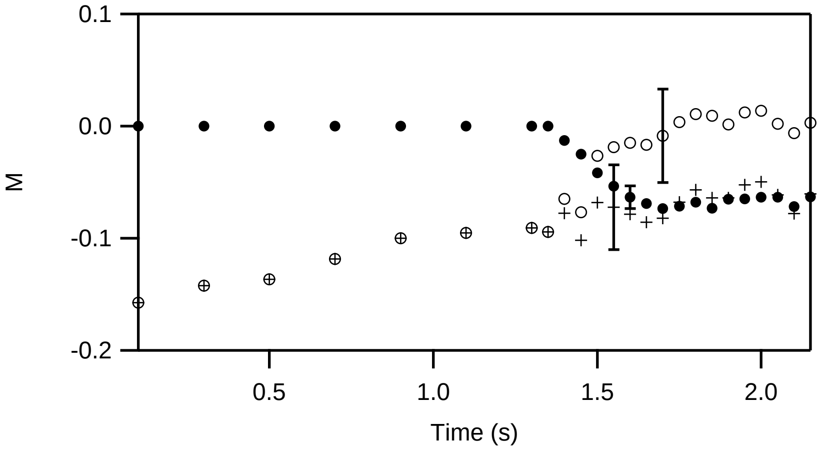

Figure 6.3: Magnetization transfer from thermal atoms to spinor condensate. The cross, solid circles, and open circles are the magnetization of the whole cloud, the BEC component, and the thermal component respectively. In addition, the error bars given here are typical. The thermal component is not strictly zero after Bose condensation. We suspect that the fluctuations on the magnetization of the thermal component are due to the uncertainty of the bimodal fit introduced in Chapter 3.

field gradients are displayed in Fig. 6.4. We can also create a pure $m_F = -1$ condensate by applying a 28 G/cm gradient in the early stage of evaporative cooling. Pure spinor condensates with different spin configurations are illustrated in Fig. 6.5.

In addition to varying the spin populations via magnetic field gradients, we can also apply microwaves tuned to the $F = 1 \leftrightarrow F = 2$ transitions as shown in Chapter 2 to manipulate the spin states. Using this technique, we can remove atoms in a spin state by pumping them to the $F = 2$ state during the evaporation. In the $F = 2$ states atoms possess internal energy of about 6.835 GHz or equivalently 328 mK, which is much larger than the trap depth of our optical trapping potential (< 1 mK). The internal energy can be converted to kinetic energy via inelastic collisions in the $F = 2$ manifold, which will result in loss of those atoms. As will be seen in Section 6.3, the lifetime of $F = 2$ manifold is measured to be 250 ms, and the population of those spin states can be reduced to $< 2\%$ in 1 s. Any residual atoms in the $F = 2$ manifold should not significantly affect the spinor dynamics in the $F = 1$ manifold. Finally, we can create coherent superpositions of condensates in different spin states using microwave pulses. We can transfer a fraction of the atoms in one spin state in the $F = 1$ manifold to another spin state in the $F = 2$ manifold with a short

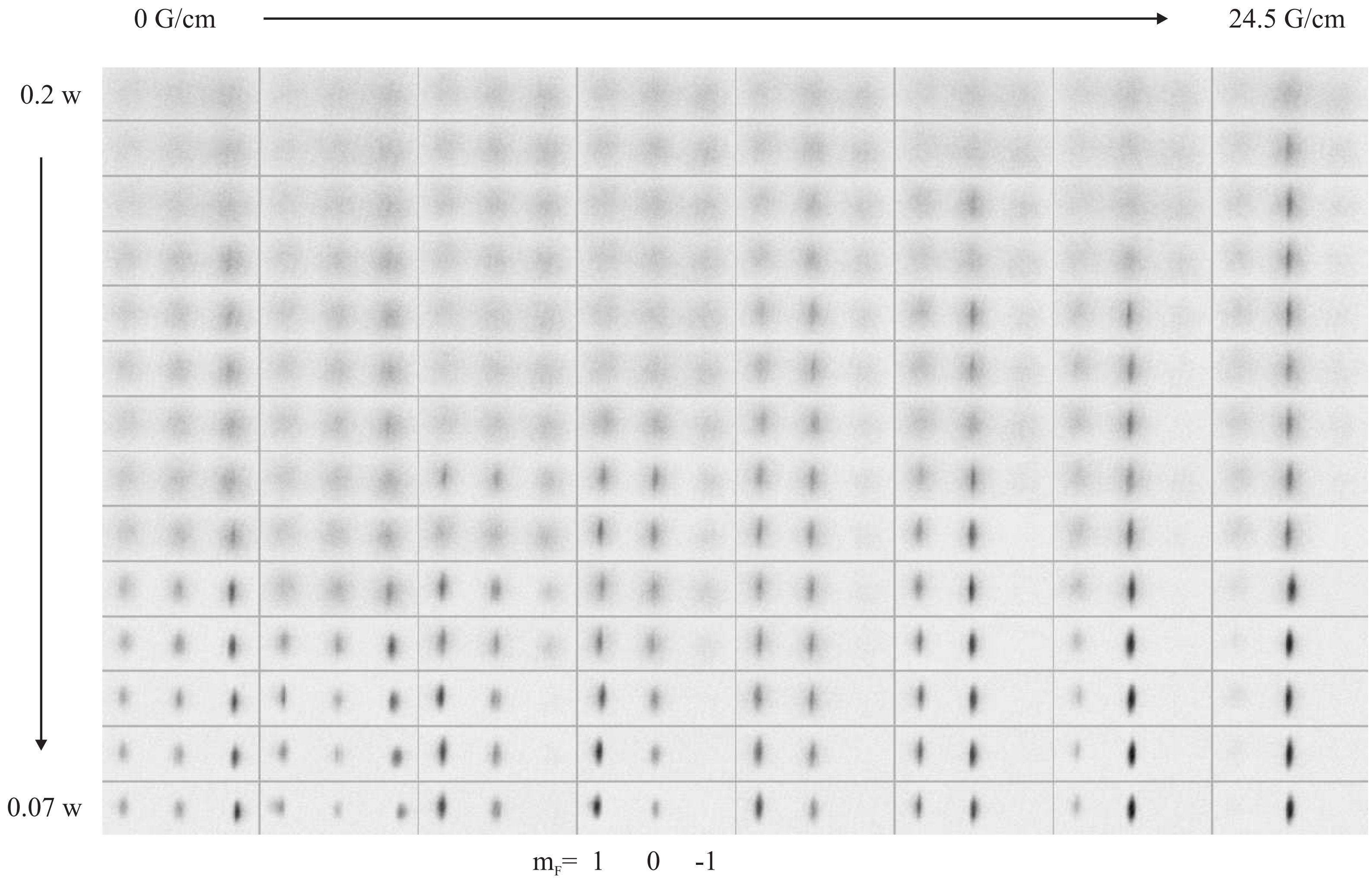

Figure 6.4: Evaporation of spinors in different field gradients.

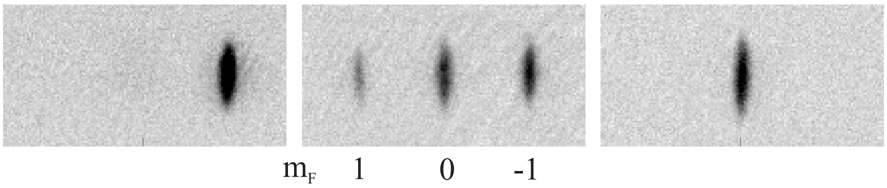

Figure 6.5: By applying different magnetic field gradients at different stages of evaporation, we can create pure condensates of a particular spin or mixtures, which consists of 30,000 to 15,000 atoms as seen above. Each absorptive image is taken after 6 ms of free expansion, and a weak Stern-Gerlach field is applied during the first 2 ms of expansion to separate three spin components spatially. The field of view of each image is 420 × 210 μm.

microwave pulse ($< 50\ \mu$s), and then immediately transfer those atoms back to another spin states in the $F = 1$ manifold by the second short microwave pulse. This technique enables us to prepare a coherent superposition of different spin states in the $F = 1$ manifold.

To summarize this section, we have studied Bose condensation of ^{87}Rb $F = 1$ spinors and showed that the net magnetization is inherited from the MOT. We have demonstrated control of internal spin states of the spinor condensates created directly in the optical traps. Our capability of controlling initial spin populations via evaporation in inhomogeneous magnetic fields and microwave transitions provides well-defined initial conditions for further investigations of the spinor ground state structure as well as the spinor dynamics.

6.2 Spinor Ground State

The mean-field ground states of spin-1 condensates have been calculated by several groups for both zero magnetic field [39, 114] and finite field cases (Appendix E) [42, 112] . Ho showed that if c_2 is negative (positive), the spinor displays ferromagnetic (anti-ferromagnetic) behavior [39]. For the case of $F = 1$ ^{87}Rb, c_2 is calculated to be $-3.58(57) \times 10^{-14}\text{Hz} \cdot \text{cm}^3$ [56]. Hence the ground state of ^{87}Rb should be ferromagnetic [55]. For a typical density of $n = 4 \times 10^{14}$ cm^{-3} in our 1-D lattice traps, the ferromagnetic energy $|c_2|n$ is only 14 Hz [42], and hence, observation of the low field ground state, $|F = 1, m_F = 1\rangle$, requires that the first order (linear) Zeeman shift $E_Z = m_F B \times$ (700 Hz/mG) be smaller than $|c_2|n$, and hence requires zeroing the magnetic field B to much less than 20 μG, typically requiring a magnetically shielded environment.

As discussed in the previous chapter, at large fields (up to ~500 mG in our case), the ferromagnetic interactions can still play a dominant role in determining the spin ground state due to constraints imposed by angular momentum conservation. If we start with a non-equilibrium spin mixture, the system will relax to the minimal energy state via spin exchange collisions, and for the $F = 1$ manifold, the only processes that conserve angular momentum are

$$2|m_F = 0\rangle \rightleftharpoons |m_F = 1\rangle + |m_F = -1\rangle. \tag{6.1}$$

In this field regime, the effect of the anti-ferromagnetism (ferromagnetism) is to lower (raise) the energy of the m_0 spinor component relative to the average energy of the $m_{\pm 1}$ components [42], which drives the reaction in Eq. 6.1 to the left (right). Hence, the extent to which this reaction is driven provides an unambiguous distinction between the ferro- and anti-ferromagnetic cases. At higher fields, these effects compete with the second order (quadratic) Zeeman shift, $(E_{+1}+E_{-1}-2E_0)/2 \simeq B^2\times$ (72 Hz/G^2) [42], which tends to drive the reaction to the left (to the m_0 state) for fields $B \gtrsim 500$ mG. Although evidence of the ferromagnetism of ^{87}Rb was already provided by the observed spin mixtures in our initial all-optical BEC demonstration (which were measured at ~100 mG) [34, 136], here we present systematic studies of the spin mixing, starting with non-equilibrium initial conditions and following its time evolution for different magnetic fields.

Our experiments employ the all-optical BEC technique described in Chapter 4 [34]. For the first part of this work, we employ a large period (5.3 μm) 1-D lattice made by a CO$_2$ laser standing wave [136] which provides a strongly anisotropic ‘pancake’ shape trap, allowing clear distinction between thermal clouds and condensates. The lattice is loaded by transferring atoms from an orthogonal travelling wave trap. We create condensates in only one lattice site by adjusting the trap power during transfer. The condensates contain $30,000$ atoms in a single lattice site with measured trap frequencies $2\pi(120, 120, 2550)$ rad/s, and no observable thermal component. The density in the optical trap is estimated to be 4.3×10^{14} cm^{-3}, and the Thomas-Fermi condensate radii are (7.6, 7.6, 0.36) μm. The $1/e$ lifetime of the condensates in our optical trap is about 3 s as shown in Fig. 6.6.

To study the spin mixing dynamics, we begin with pure $m_F = 0$ condensates as the initial condition, which are created in a field gradient of 28 G/cm. After condensation, the

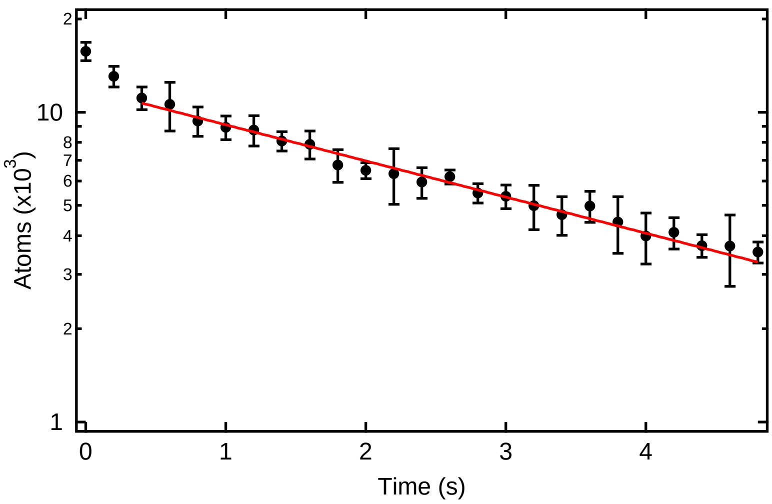

Figure 6.6: Lifetime of the condensates in the 1D optical lattice. Typical condensate lifetime in the 1D lattice is ∼ 3 s. In the case illustrated here, it is measured as ∼ 3.7 s following an initial fast decay.

field gradient is turned off, and a variable magnetic bias field is adiabatically ramped up in 10 ms. This field can be directed either along the tight (axial) or weak (radial) axes of the confinement potential. The condensate is then allowed to evolve for a variable amount of time, and then the spin populations are measured using absorptive imaging following 6 ms of free expansion. To spatially separate the spin components, a weak Stern-Gerlach field is applied during the first 2 ms of expansion. Typical results for 2 s of spin mixing are shown in Figure 6.7. We note from these three images taken under identical conditions that there is significant variation on the degree of mixing from run to run of the experiment. However, in each case, the magnetization appears to be conserved. Generally, the components of the spin mixtures are identical in shape to the original cloud to within our imaging resolution. Occasionally one or more of the components will appear to have either a thermal component or a distorted shape.

We have measured the spin mixing for different evolution times following preparation of the $m_F = 0$ condensates. Fig. 6.8 shows the time evolution of relative spin populations in different B fields. The time to reach equilibrium of the spin mixing is typically less than 600 ms, and this time decreases slightly with increasing magnetic field. Fig. 6.9 shows the average time evolution of ρ_0 and M for 50 repeated measurements. First, we note that the

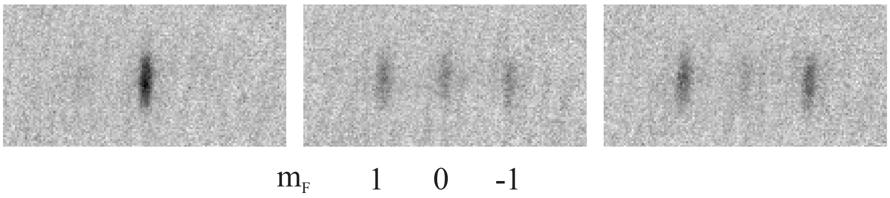

Figure 6.7: Spin mixing of spinor condensates in the optical trap. The mixing process starts with a pure $m_F = 0$ condensate in the optical trap. Three separate measurements of the spin state are shown after 2 s of spin mixing.

magnetization, M, is conserved throughout the mixing to within a few percent. Although the data does suggest a drift of M below zero by a small amount -3.5±2% (the uncertainty here and error bars in the data are purely statistical), the deviation, if any, is comparable to our uncertainties in measuring populations (~3%), limited by the absorptive imaging technique. Secondly, there is an almost ten fold reduction in the statistical noise of the magnetization relative to that of the total population, which varies 17% from shot to shot. This suggests that the fluctuations of ρ_1 and ρ_{-1}, which are coupled from the mixing processes in Eq. (6.1), are quantum correlated. These correlations underly theoretical predictions for spin squeezing and entanglement in the system [132]. Thirdly, the relaxation of ρ_0 to the steady state value is not monotonic but instead shows a damped oscillation at 4 Hz. Such oscillations are a natural outcome of coherent spinor mixing and will be discussed in greater detail in Chapter 7.

The behavior of the mean-field ground state of spinors in magnetic fields can be understood from the energy contour given by Eq. 5.28, $E = c\rho_0 \left[(1-\rho_0) + \sqrt{(1-\rho_0)^2 - M^2}\cos\theta\right] + \delta(1-\rho_0)$. Here ρ_0 is the fractional population of m_0 state, M is the magnetization, and θ is the spinor phase defined in the previous chapter. The energy contour of ferromagnetic and anti-ferromagnetic spinors for $M = 0$ are shown Fig. 6.10. In zero magnetic field, the ferromagnetic ground state is $\rho_0 = 1/2$, $\theta = 0$, and the anti-ferromagnetic ground state $\theta = \pi$, however, ρ_0 is not uniquely determined in (0, 1) [137]. When the field is not zero, the anti-ferromagnetic ground state reduced immediately to $\rho_0 = 1$, while in the ferromagnetic case, ρ_0 will gradually increase as B field increases. This gives a clear signature for distinguishing ferromagnetic and anti-ferromagnetic spinors.

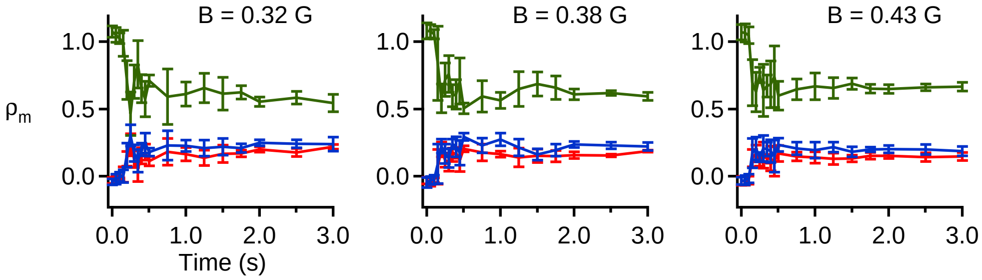

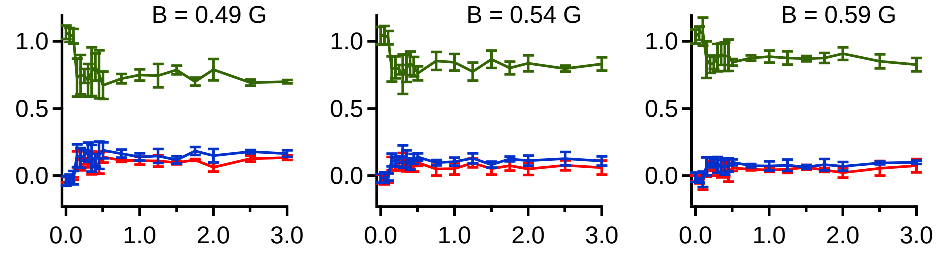

Figure 6.8: Plots of the relative spin populations vs. time in different magnetic fields. Here RGB colors represent the relative population of $m_F = 1, 0, -1$ states.

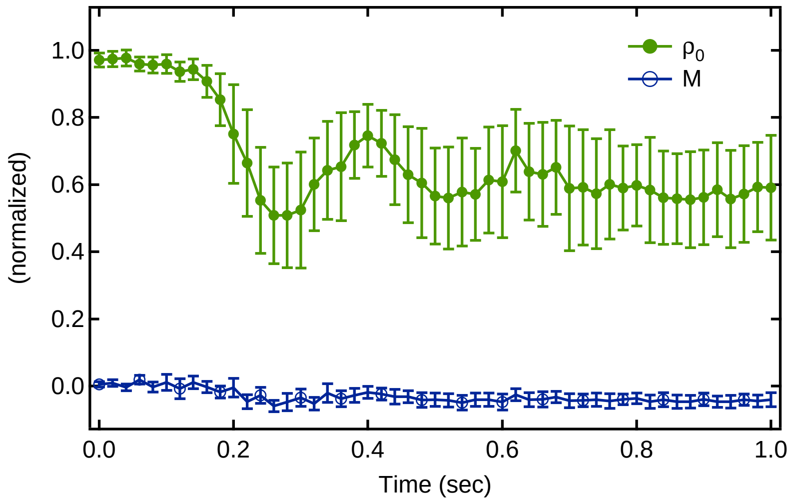

Figure 6.9: Plot of the fraction in the m_F=0 state n_0 and magnetization M (open circle) vs. time. In this measurement, M is determined to be 0.5±0.8% initially and -3.5±2% after mixing. Note that there is a 8.5-fold reduction on the fluctuation of M compare to that of the total population (which is measured to be 17%). Clear population oscillations of n_0 are seen, and the fluctuation in n_0 is 6.6 fold of that of M. This data was taken at a bias field of 100 mG

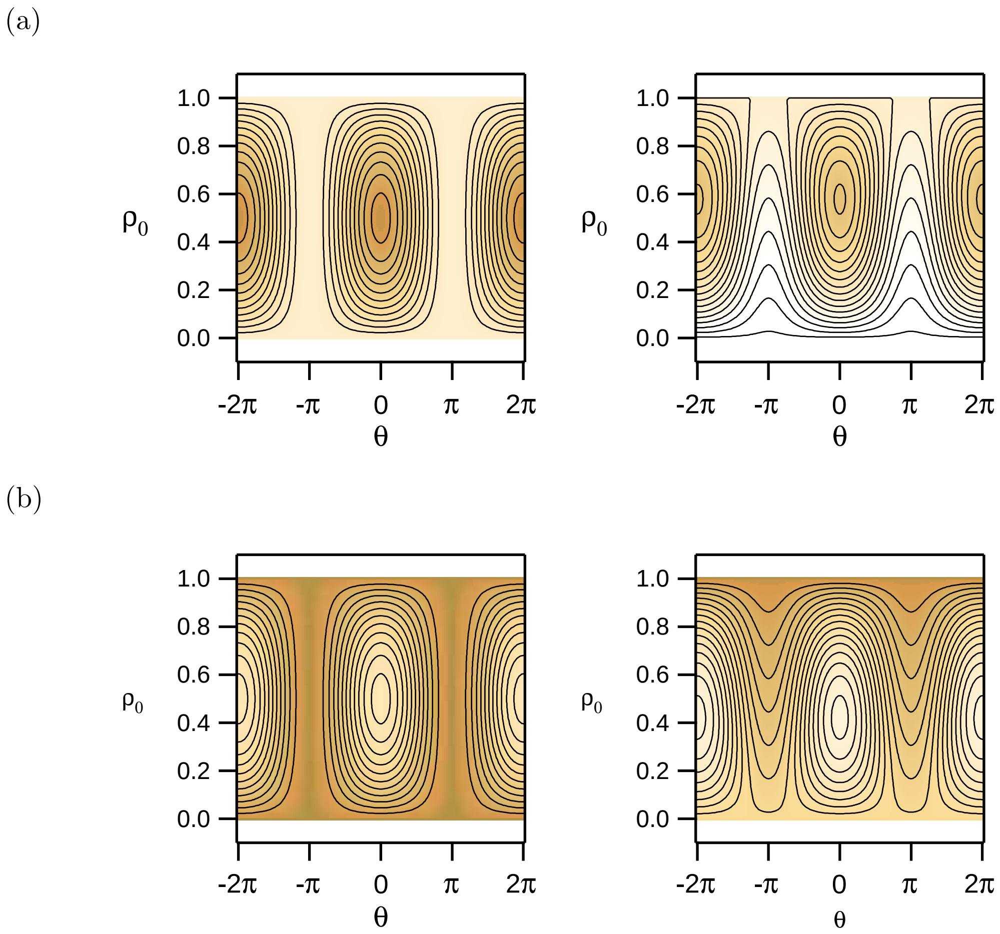

Figure 6.10: Energy contour for spinors. (a) Energy contours for ferromagnetic spinors ($c_2 < 0$) with total magnetization $M = 0$. (b) Energy contours for anti-ferromagnetic spinors ($c_2 > 0$) with total magnetization $M = 0$. Left column: $B = 0$. Right column: $B = 100$ mG. Here ρ_0 is the fractional population of m_0 state, and θ is the spinor phase defined in previous chapter. For ferromagnetic spinors, the ground state at $B = 0$ is $\rho_0 = (1 - M^2)/2$ with $\theta = 0$. For anti-ferromagnetic spinors, the ground state at $B = 0$ is a singlet state, and therefore ρ_0 is undefined, and fluctuate in (0, 1). This happens at $\theta = \pi$.

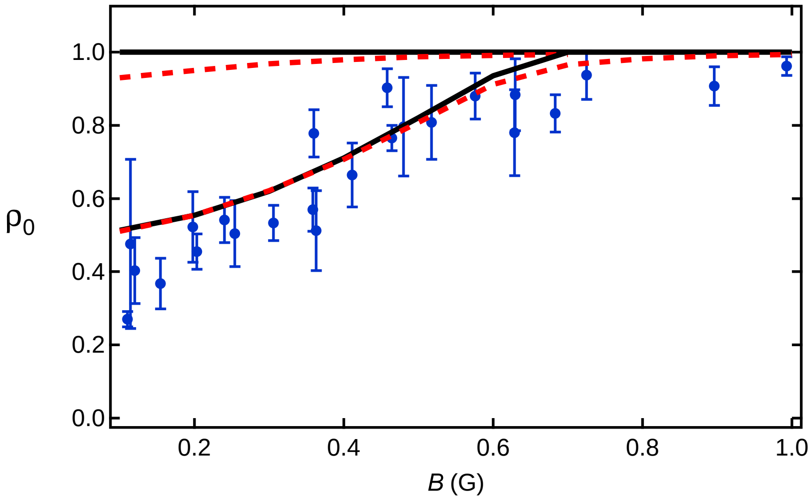

Figure 6.11: Plot of ρ_0 vs. magnetic field after 3 s of spin mixing. The upper curves are the theoretical predictions for the anti-ferromagnetic case, while the lower curves are for the ferromagnetic case. The solid curves are the predictions with zero magnetic field gradient. The dashed curves are the predictions with a gradient of 20 mG/cm applied, which is the measured upper bound in our trap.

To make a comparison with theoretical predictions [112], we measure the degree of mixing for different applied magnetic fields. Fig. 6.11 shows the results of spin mixing for 3 s, in which ρ_0 is plotted vs. the applied field. Also shown in this figure are theoretical curves for both the anti-ferro- and ferromagnetic cases in a magnetic field with and without a small (20 mG/cm) gradient [112]. As evidenced by the data, the spin mixing agrees with the ferromagnetic predictions and is inconsistent with the anti-ferromagnetic prediction. When the field is larger than 700 mG, the quadratic Zeeman effect completely dominates the spin interaction, and the condensates remain in the $m_F = 0$ state. Note that magnetic fields are applied either along tight trap or weak trap axes; however, no significant difference in the measurements is observed.

We also measured spin mixing for fields less than 100 mG but found that our results at these low fields varied significantly from day to day. We suspect they were affected by the stray AC magnetic fields present in the chamber [1]. These fields are capable of driving off-resonant rf-transitions between the Zeeman sub-levels. We observed this directly by creating a $F = 1, m_F = -1$ condensate (for which there is no spin mixing due to conservation of magnetization) and measuring the final spin population. For magnetic fields greater than 100 mG, the magnetization remains conserved, while at lower fields, the $m_F = -1$ atoms are quickly pumped by the AC fields (within 100 ms for fields <10 mG) to other Zeeman states. In addition, in low fields atoms could also undergo diabatic spin flips when the Stern-Gerlach separation is performed at the end of each spinor experiment run.

Mean-field theory predicts that the spinor phase is $\theta = \theta_1 + \theta_{-1} - 2\theta_0 = 0$ for ferromagnetic ground state. We attempted to directly measure the phase relationship between the spinor components [114] by performing an interference experiment between two spinor condensates created in adjacent lattice sites. In the absence of dephasing mechanisms, we would expect to see clear interference fringes in time-of-flight measurements both before and after spin mixing. In the measurement shown in Fig. 6.12, clear interference fringes were visible initially, while fringes were typically not observed after mixing. It is quite possible however that the observed dephasing of the interference pattern was caused by small field variations between two sites due to a stray magnetic field gradient (< 20 mG/cm) [2].

6.3 Observation of Spin-2 Dynamics

In the studies in previous sections, we have used microwave tuned to $F = 1$ and $F = 2$ transitions to measure the magnetic field. This microwave transition also allows to to study $F = 2$ spinors. To do that, we coherently excite the pure $F = 1, m_F = 0$ condensates to $F = 2, m_F = 0$ using microwave fields tuned to 6.8 GHz. Additionally, by controlling the bias field, the microwave frequency, and the initial Zeeman state in the $F = 1$ manifold,

---

[1] Outside the chamber, magnetic field is monitored by a 3-axis fluxgate magnetometer. The AC magnetic field is measured to be $10 - 15$ mG, and they are mainly 60 Hz and 300 Hz noises from powered equipments nearby. Inside the chamber the B field is measured by microwave spectroscopy synchronized with 60 Hz line signal, and we found the frequency shift at different phases of a 60 Hz cycle is equivalent to a AC field of ≤ 5 mG

[2] To determine magnetic fields at the trap location, we employ microwave spectroscopy on the field sensitive $F = 1 \rightarrow F = 2$ hyperfine transitions which is sensitive to within 2 mG. Furthermore, the field gradient is determined to be <20 mG/cm by measuring fields at different trap locations.

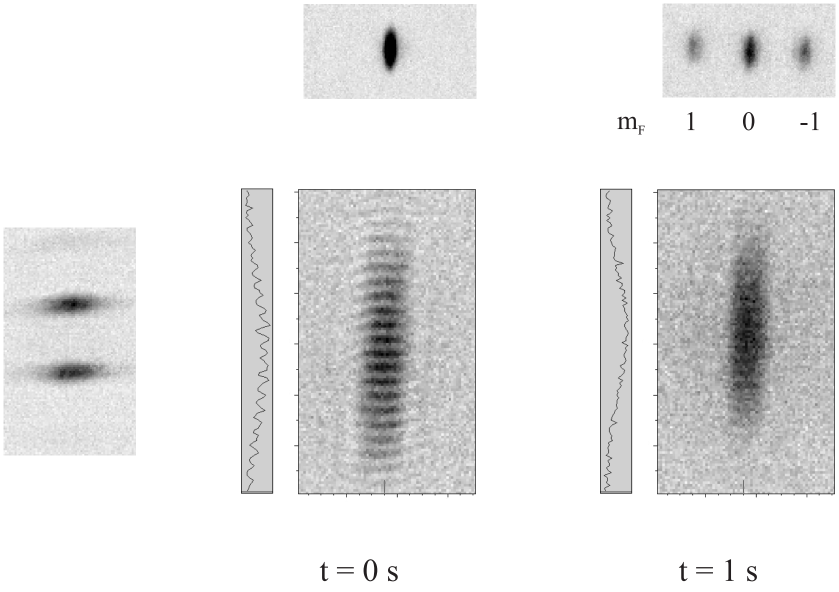

Figure 6.12: Interference of two spinor condensates before and after spin mixing. At time zero, interference of two pure m_0 condensates created in two adjacent lattice sites presents clear interference fringe. After spin mixing for 1 s in a field of 100 mG, fringes are typically not observed.

we can pump the condensate to any Zeeman sub-level of the excited hyperfine manifold. The $|F = 2, m = 0\rangle$ condensate is observed to decay as shown in Fig 6.13(a). Following an initially rapid decay, it decays exponentially with a time constant of 250 ms. Despite the short lifetime in the excited hyperfine manifold, we still observe spin mixing within 50 ms, and magnetization conservation is also observed during the mixing, as shown in Fig. 6.13(b).

In summary, we have observed spin mixing of ^{87}Rb spinor condensates in $F = 1$ and $F = 2$ hyperfine manifolds in an optical trap. The observed equilibrium spinor configurations of the lower manifold confirms that $F = 1$ ^{87}Rb is ferromagnetic. The magnetization was conserved within the measurement errors during the entire spin mixing process. The reduced noise of magnetization suggests quantum correlation of the spin dynamics, which underlies spin squeezing and spin entanglement.

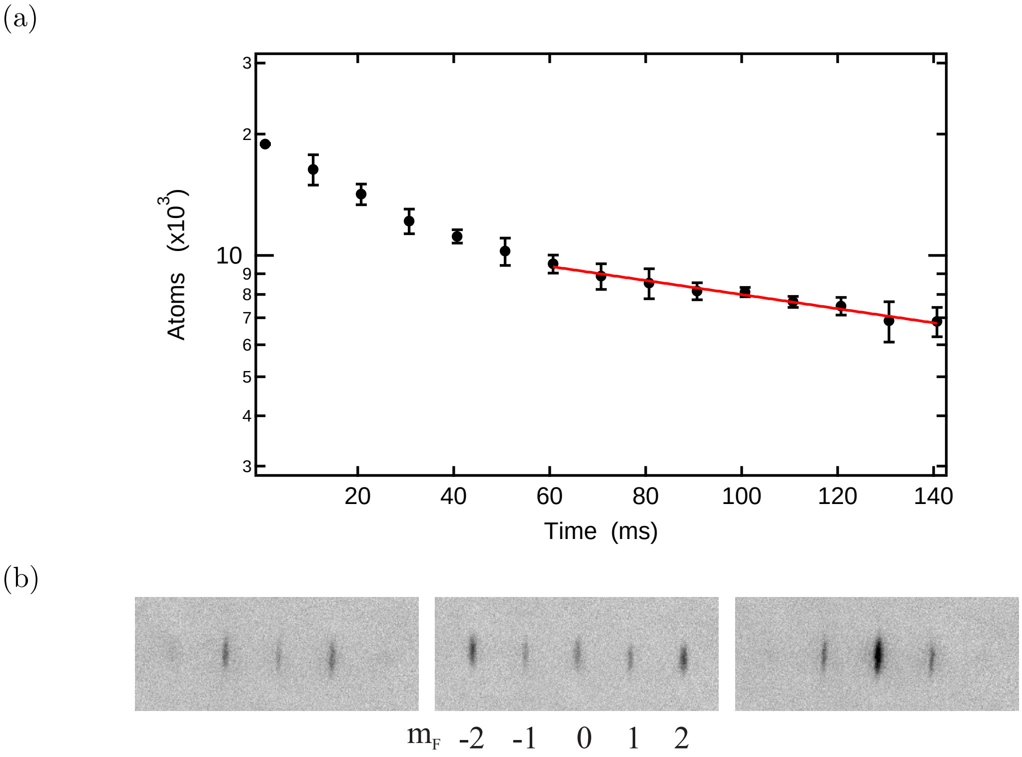

Figure 6.13: (a) Lifetime measurement of $F = 2$ spinor condensates. Following a rapid decay initial decay, the population decays exponentially with a time constant of 250 ms. (b) Spin mixing of the $F = 2$ spinor condensates in the optical trap. These images represent three identical measurements after 50 ms of spin mixing. Note that the magnetization is conserved.

CHAPTER VII

COHERENT SPINOR DYNAMICS

In this chapter, we describe our observation of coherent spin-mixing collisions. Collisions in a thermal gas are perceived as random or incoherent as a consequence of the large numbers of initial and final quantum states accessible to the system. In a quantum gas, e.g. a Bose-Einstein condensate or a degenerate Fermi gas, the phase space accessible to low energy collisions is so restricted that collisions become coherent and reversible.

Collisional coherence is an important theme in quantum degenerate gases. For single component condensates, such as spin-polarized atomic condensates confined in a magnetic trap, the coherence of the collisional interactions has been well-established in early measurements of condensate mean-field energy [138] and correlations [18] as well as in demonstrations of matter-wave interference [10] and superfluid behaviour [25, 26, 27]. Collisional coherence in more complicated systems has led to remarkable results, including reversible atom-molecule formation across a Feshbach resonance for both bosonic and fermionic [139, 140] atoms, and coherent collisions in optical lattices [14, 12].

In this chapter we show that the collisional coherence extends to the internal spin degrees of freedom of a spin-1 Bose gas by observing coherent and reversible spin-changing collisions in spin-1 condensates. In a spin-1 condensate, two atoms with spin states m_1 and m_{-1} can coherently and reversibly scatter into final states containing two atoms with spin component m_0 and vice-versa (Fig. 7.1a). Spin mixing has been observed in both $F = 1$ and $F = 2$ condensates in the last chapter [42, 44, 45, 125]. Experiments so far have revealed mostly incoherent relaxation of initially non-equilibrium spin populations to lower energy configurations from which the sign of the spin interaction parameter c_2 was determined. Although strongly-damped oscillations in spin populations were observed in our initial experiments discussed in Chapter 6 and by others [44, 125], their interpretations are limited due to the fact that the initial spin configurations in these experiments were metastable, and evolution from these states is noise-driven [42, 44, 45, 125]. Nonetheless, from these observations, as well as studies of spin domain formation, it was possible to determine the magnetic nature of the ground states.

7.1 Initiation of Coherent Spin Mixing

In the mean-field limit, condensates are described by coherent states, and coherent spin mixing is simply a process of atomic four-wave mixing, which can be seen in Eq. (5.23). The spin mixing rate is proportional to the product of the amplitudes of the order parameters, and in most cases it requires presence of all three spin components. To better demonstrate the coherent spin mixing, we start with a non-stationary spin configuration. Under the single-mode approximation (SMA), the internal state of a coherent superposition of m_0 and m_{-1} condensates can be expressed as $\vec{\zeta} = (0, \zeta_0, \zeta_{-1})$. With this initial condition, the spin mixing rate at time zero is nonzero, and it is given by $i\hbar\dot{\zeta_1} = c\zeta_0^2\zeta_{-1}^*$ according to Eq. (5.25). Indeed, the m_1 component is generated from a nonlinear wave mixing of the other two components, which are macroscopically occupied at time zero, and it is this initial configuration that deterministically initiates the spin mixing. If one starts with a pure m_0 or a mixture of m_1 and m_{-1} condensates, the initial mixing rate should be zero according to Eq. (5.25), and it would take much longer time to build up the spin mixing rate. In these cases, technical noise is more likely to play a role in the initiation of spin mixing. This can explain the exceptionally large noise on the spin population oscillation amplitude presented in Fig. 6.9.

To investigate the coherent dynamics of this system, we begin with ^{87}Rb condensates created in the single focus trap. The condensates created in this optical trap are generally in a mixture of all $F = 1$ spin states and reveal complicated spatial domains. To create a well-characterized initial condition, we apply a magnetic field gradient during the evaporative cooling [45], which results in pure $m_F = -1$ condensate containing 150,000 atoms. This state is stable against both local and global spin dynamics due to the conservation of angular momentum. The trap frequencies are 2π(190,170,17) rad/s, and the condensate density and the Thomas-Fermi (T-F) radii are estimated to be 2.1×10^{14} cm^{-3} and (3.2,3.6,36) μm

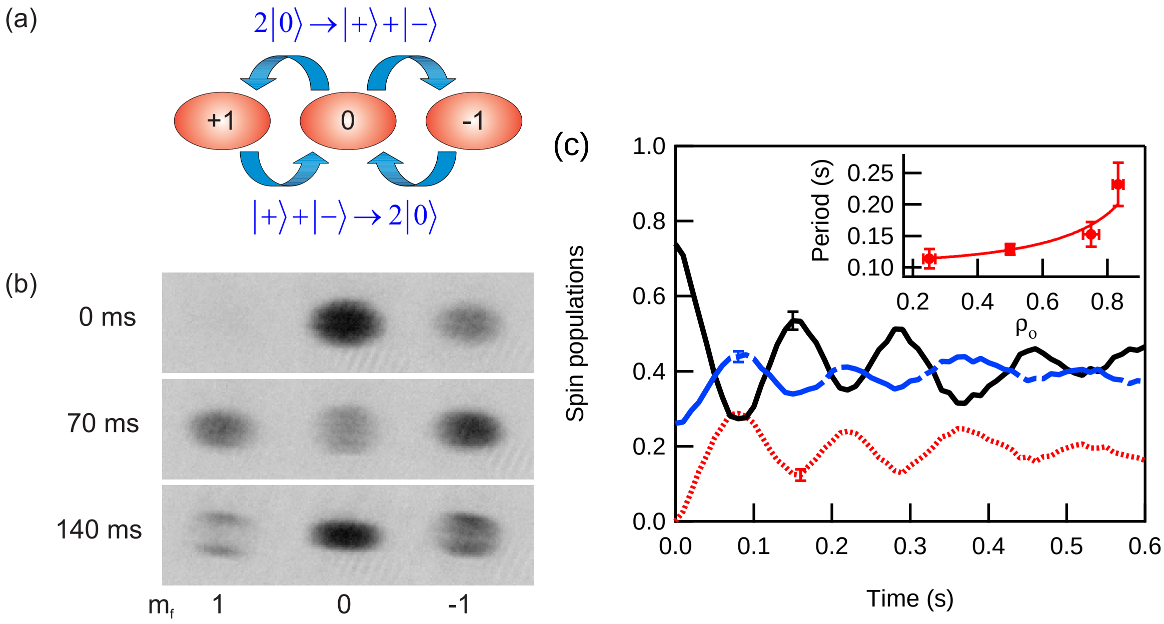

Figure 7.1: Coherent spin mixing of spin-1 Bose condensate in an optical trap. Coherent spin mixing producing oscillations in the populations of the $F = 1$, $m_F = 0, \pm 1$ spin states of ^{87}Rb condensates confined in an optical trap starting from a superposition of condensate spin components at $t = 0$ that is subsequently allowed to evolve freely. a) Schematic indicates fundamental spin mixing process. b) Absorptive images of the condensates for different evolution times. In this example, the initial relative populations are $\rho_{(1,0,-1)} \simeq (0, 3/4, 1/4)$. The condensates are probed 18 ms after release from the trap, and, to separate the spin components for imaging, a weak magnetic field gradient is applied for 3 ms during expansion of the condensates. The field of view is 600 μm × 180 μm. c) Spin populations vs. evolution time for the same initial population configuration showing four clear oscillations. The damping of the oscillations is due to the breakdown of the single mode approximation readily apparent in the $t = 140$ ms absorptive image. Here the dotted, solid, and dot-dashed lines represent the populations in $m_F = 1$, 0 and -1 states. Inset shows the measured oscillation period versus the initial population of the 0 state for different initial superpositions of $m_F = 0$, -1 states, which compares well with the theoretical prediction [114]. The (typical) error bars shown are the standard deviation of three repeated measurements.

respectively. The lifetime of the condensate is measured to be 3 s. Coherent spin state superpositions are created from the pure $m_F = -1$ condensates by applying a sequence of phase-coherent microwave pulses tuned to $F = 1 \leftrightarrow F = 2$ transitions. The pulses are applied at a field of 420 mG to separate out the transitions between the different Zeeman sub-levels. Following the pulse sequence, the magnetic field is ramped from 420 mG to 15 mG in 10 ms. Typical pulse lengths are 20 μs for a $F = 1 \leftrightarrow F = 2$ pulse. Following this state preparation, the condensate is allowed to freely evolve in the optical trap. A typical evolution is shown in Fig. 7.1c for an initial spin configuration of $\rho_{(1,0,-1)} \simeq (0, 0.75, 0.25)$. Up to four distinct oscillations are observed in this example before the spin populations damp to a steady state. These oscillations demonstrate the coherence of the spin mixing process.

The oscillations are observed to damp with a time constant of 250 ms, and the damping coincides with the appearance of spatial spin structures apparent in the images in Fig. 7.1b. These structures indicate the invalidation of the SMA underlying Eq. (5.23) and lead to a complicated interplay of the internal and external dynamics that ultimately transfers the internal spin energy into spatial domain structures [114]. Detailed studies of these domain structures will be presented in the next chapter.

7.2 Measuring c_2

We have measured the spin oscillation frequency for different initial spin populations. These data are shown in the inset of Fig. 7.1c. and show good agreement with theoretical predictions, $c\sqrt{1-\rho_0^2}$ [114, 117] which can be derived from Eqs. (5.26-5.27). These measurements provide a direct determination of the magnitude of the spin interaction energy [54], $|c|/\hbar = 2\pi \times 4.3(3)$ rad/s for the case shown here. These oscillation frequencies at low magnetic field do not determine the sign of c (c_2), however it was established by studies of the nature of the ground state in the last chapter [44, 45] that $c_2 < 0$ for the $F = 1$ manifold of ^{87}Rb. As we shall see in Fig. 7.4, the negative sign of c_2 is reconfirmed in the present study. This value of c, combined with the measured condensate density, $n = 2.1(4) \times 10^{14}$ cm^{-3}, determined from the rate of the condensate expansion during time-of-flight shown in Appendix F, permits determination of c_2, or equivalently, the difference in scattering lengths, $a_2 - a_0 = -1.4(3)a_B$, where the Bohr radius $a_B = 0.529$ Å. This is the first direct measurement of this important quantity, and our value agrees with the theoretical determination of $a_2 - a_0 = -1.40(22)a_B$ derived from photoassociative spectroscopic and Feshbach resonance data [55, 56].

7.3 Controlling Coherent Spin Mixing

The observed spin-mixing is an internal state analogue to Josephson oscillations in weakly connected superconductors [128]. To exploit this analogy, we demonstrate control of the coherent spinor dynamics using phase and population engineering. The large amplitude oscillations observed in Fig. 7.1c are in the nonlinear regime of Eqs. (5.26-5.27). It is also possible to access the linear regime more typical of the standard Josephson effect by tuning the parameters of the system. In particular, for large applied magnetic fields such that $\delta \gg c$ and appropriate initial populations, the phase evolution is dominated by the quadratic Zeeman effect of the external field. For these conditions, the system exhibits small oscillations in direct comparison to the AC-Josephson oscillations [1], and Eqs. (5.26 - 5.27) reduce to

$$\begin{aligned} \rho_0(t) &\simeq A\delta^{-1}\sin\theta, && (7.1)\\ \dot{\theta}(t) &\simeq -2\delta/\hbar, && (7.2) \end{aligned}$$

where the oscillation amplitude A is determined by the initial populations.

We have observed these oscillations as shown in Fig. 7.2 for different applied magnetic fields. Up to 12 fast oscillations are observed at the highest fields that were studied, where the time scale of the internal spinor dynamics is better separated from the time scale for the formation of spatial spin structures. As seen in Fig. 7.3, the frequency of the measured oscillations vs. the magnetic field matches within 10% of the prediction $\Omega = 2\delta$, while the δ^{-1} scaling for the amplitude is seen only for higher fields, due to the invalidity of the SMA

---

[1] The equation of motion for the AC-Josephson effect in weakly-linked superconductors are $I(t) = I_c \sin\theta$, and $\dot{\theta}(t) = 2eV/\hbar$, where V is the applied electric voltage, e is the charge of the electron, and I_c is the superconducting current [141].

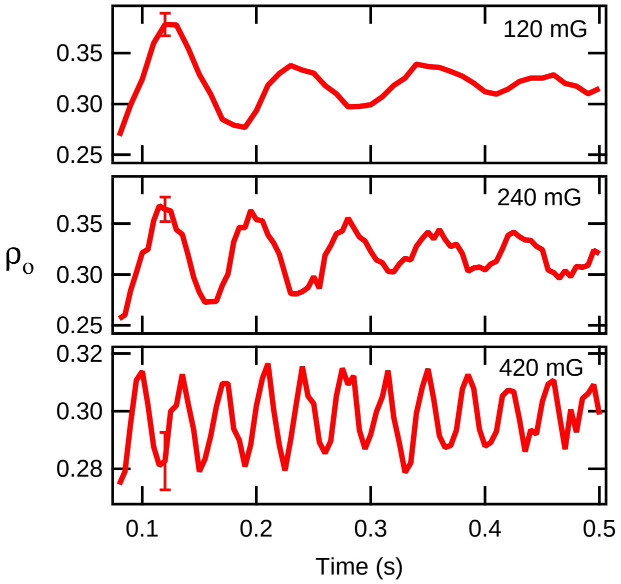

Figure 7.2: Coherent spin mixing vs. magnetic field. An initial non-equilibrium spin population configuration of $\rho_{(1,0,-1)} \simeq (0, 1/2, 1/2)$ is created and allowed to evolve in a field of 15 mG for 70 ms to allow for maximum spin mixing. At this point, the magnetic field is ramped to different levels. Subsequently, the system displays small amplitude oscillations analogous to the AC Josephson effect, $\rho_0(t) \propto \delta^{-1} \sin 2\delta t$. The typical error bars shown are the standard deviation of three repeated measurements.

for larger amplitude oscillations in low fields. The conditions for the validity of the SMA will be studied in the next chapter. In the future, being able to tune the system to the linear regime provides a path to study many analogous effects previously observed in Josephson systems such as Shapiro levels [142, 128, 124, 131] by including a time-varying component to the applied magnetic field.

7.4 Coherence of the Ferromagnetic Ground State

Beyond controlling the system via the initial conditions, the dynamical evolution of the system can be controlled in real time by either changing spin populations and/or changing the spinor phase θ. We demonstrate that we can coherently control the dynamical evolution of the spinor by applying phase shifts. In particular we drive the systems to the ferromagnetic spinor ground state using this technique. In this experiment, an initial non-equilibrium spin configuration is created and allowed to evolve for a fraction of an oscillation until $\rho_0(t)$ reaches the ground-state ratio $\rho_{0,gs} = (1-M^2)/2$ [114, 112]. At this point, the system is not

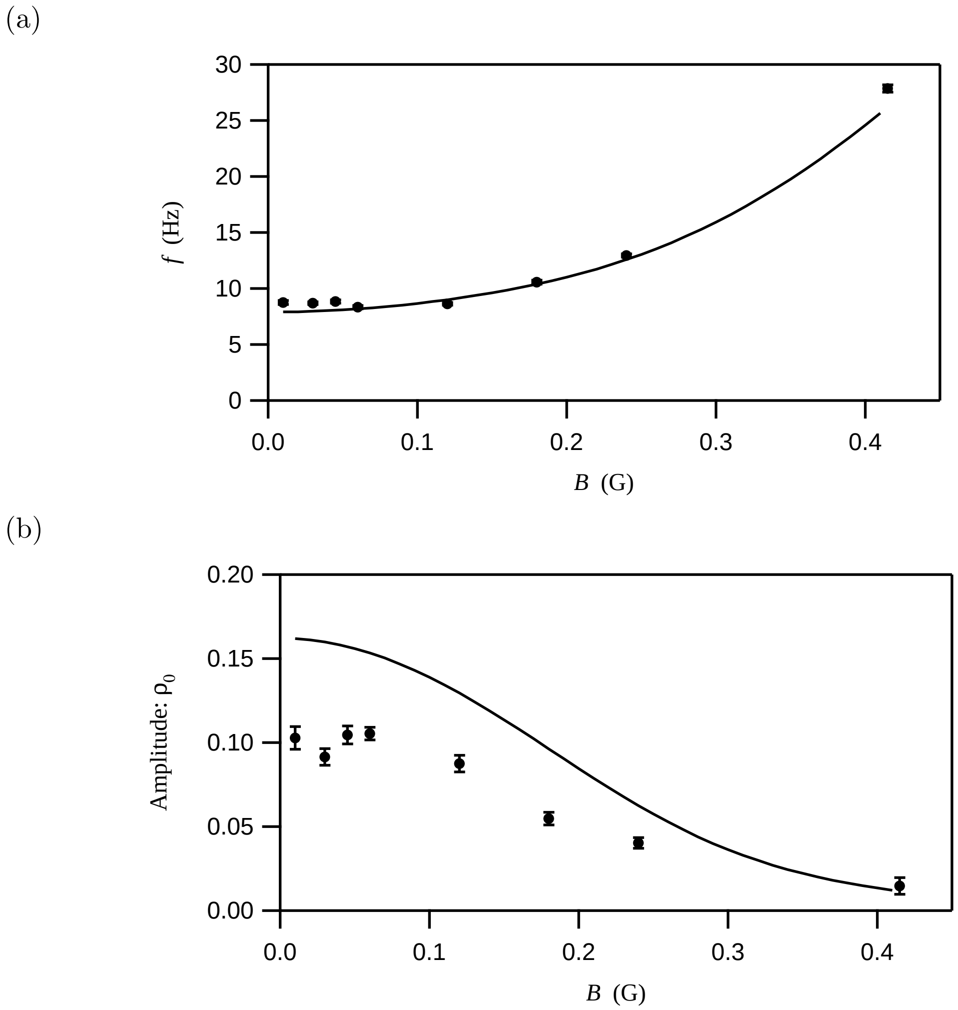

Figure 7.3: Spin mixing vs. B field. Solid curves are the theoretical predictions. The deviation between the theoretical prediction and the measurements on the oscillation amplitudes in low fields is due to that the internal spinor energy used to drive spin mixing are coupled out to spatial degrees of freedom to drive spatial dynamics.

in the ground state because $\theta \neq (\theta_{gs} = 0)$ (and it is still oscillating!) At this moment, we briefly pulse on a magnetic field of 0.6 G to apply a phase shift to the spinor, $\Delta\theta = \int \delta(t)\mathrm{d}t$. The evolution of the system is recorded in Fig. 7.4a for different pulse durations. We find that for particular applied phase shifts, the spinor condensate is brought to its ground state, evidenced by the subsequent lack of population oscillation. For other applied phase shifts, the system is driven to different points in the phase space of the system, for which the subsequent evolution of the system is dramatically different and exhibits oscillations.

It is possible to reconstruct the dynamical trajectories of the system using the measured $\rho_0(t)$, along with the known applied phase shifts and the equations of motion, Eqs. (5.26-5.27). Although the damping evident in the measurement is due to the spatial dynamics coupled to the internal spin mixing dynamics, a phenomenological phase damping term may be added to Eq. (5.27) to represent the spatial varying spin mixing rate which is responsible for damping the population oscillation. The reconstructed trajectories show qualitative agreement with the measurements in the time domain. The trajectories are plotted on the phase space diagram of the system (Fig. 7.4b). Also shown in the figure are the contours of equal energy of the spinor given by Eq. (5.28). The trajectories clearly show that the system tends to damp to the minimum energy points (i.e. the ferromagnetic spinor ground state), which is $\rho_0 \simeq 3/8$, $\theta_{gs} = 0 \mod (2\pi)$ for $M = 1/2$, $c < 0$ and $\delta \approx 0$. For the case of anti-ferromagnetic interactions, such as in ^{23}Na, $c > 0$, the energy contours differ only in sign, and the system would instead relax to $\rho_0 = 1$, $\theta_{gs} = \pi \mod (2\pi)$ within the validity of the SMA [114, 112].

To demonstrate explicitly the coherence of the spinor ground state, we impart a second phase shift to the system at later times to displace the system to a different point in phase space. As anticipated, the second phase shift is found to re-initiate the spin mixing dynamics (Fig. 7.4c) when $\Delta\theta \neq 0 \mod (2\pi)$. We have used this technique to determine the ground state spinor decoherence time by measuring the amplitude of the subsequent oscillations for different delay times of the second pulse. The spinor decoherence time is found to be 3 s, and is shown in Fig. 7.5. This decoherence time is approximately the lifetime of the condensate and is much longer than the damping time (< 0.3 s) of spin population oscillations, which

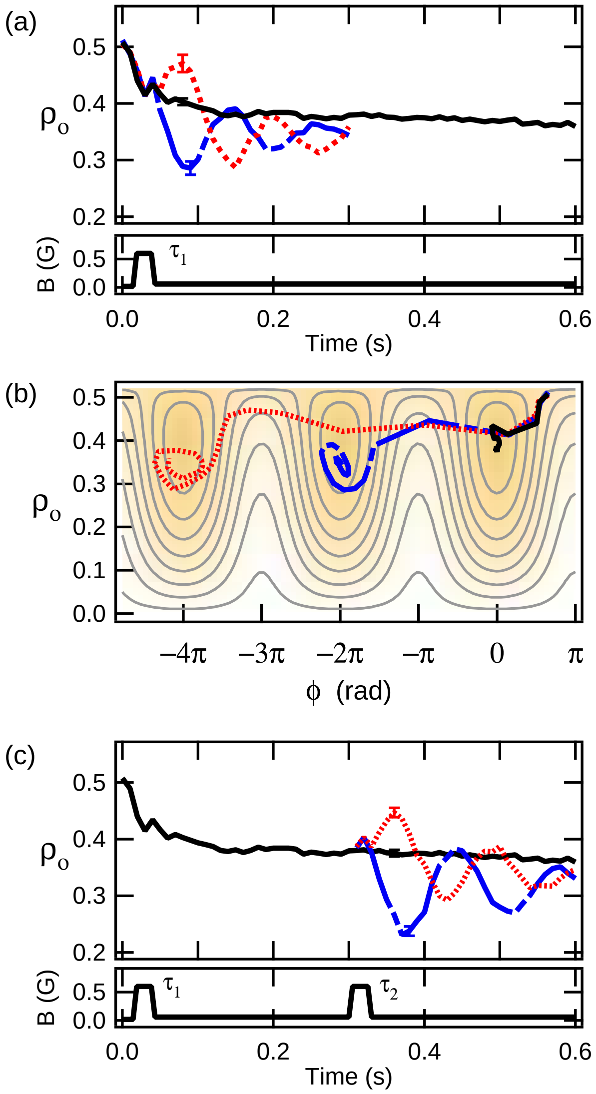

Figure 7.4: Coherent control of spinor dynamics. a) An initial spin configuration of $\rho_{(1,0,-1)} \simeq (0, 1/2, 1/2)$ is allowed to evolve in a field of 15 mG for 14 ms at which point the populations reach the values corresponding to the ferromagnetic ground state at this magnetization: $\rho_{(1,0,-1)} \simeq (1/16, 3/8, 9/16)$. Then, a pulse of 600 mG field is applied to shift the spinor phase. The dashed, solid and dotted curves represent pulse widths of $\tau_1 = 20$, 24.4 and 30 ms respectively. For certain applied phase shifts, the coherent spin mixing can be halted. This occurs for $\tau_1 = 24.4$ ms corresponding to phase shift $\Delta\theta = -2.5\pi$ and for $\tau_1 = 5.3$ ms corresponding to $\Delta\theta = -0.5\pi$. b) Reconstructed dynamical trajectories of the system determined by fitting the experiment data to Eq.(5.26-5.27) including a phenomenological phase damping term. The free parameters of the fit are the damping coefficient and the unknown (but reproducible) initial spinor phase resulting from the state preparation that depends on the applied microwave pulse width and the duration in the upper hyperfine manifold. The contours show curves of equal energy. c) To investigate the spin coherence of the ground state spinor created by the first pulse with $\tau_1 = 24.4$ ms, a second pulse is applied at 300 ms to reestablish the oscillations. The solid, dashed and dotted curves corresponds to $\tau_2 = 0$, 10 and 20 ms respectively. The typical error bars shown are the standard deviation of three repeated measurements.

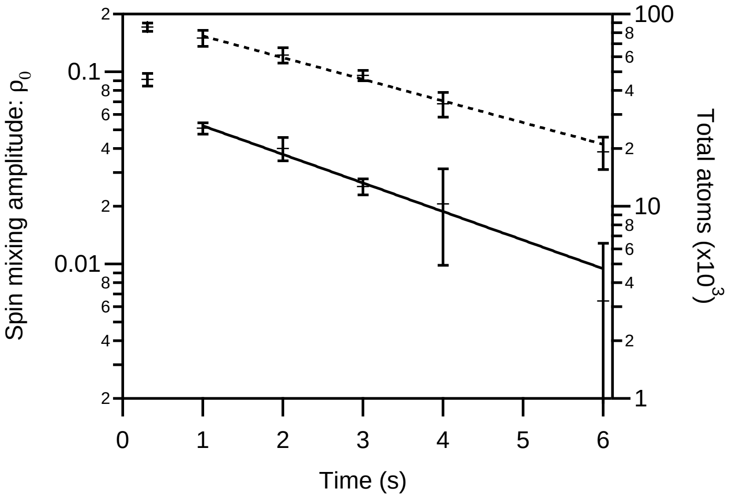

Figure 7.5: Decoherence time of the spinor condensates. The lifetime of the condensate is measured to be 3.8 ± 0.5 sec, while the decoherence time of the spinor is 2.9 ± 0.5 sec. Since the amplitude presents a fast decay initially, the first point is exclude from the fit. We suspect the initial fast decay on the spin mixing amplitude is due to partial spatial separation of m_1 and m_{-1} component which will be shown in Chapter 8.

is is in the time scale of the spatial dynamics ($\sim c_2 n$).

As noted, the damping of the spin oscillations coincides with the appearance of spin wave-like spatial structures in the spinor wave function (see images in Fig. 7.1b). Hence it is clear that the SMA is not strictly valid for our system. These waves derive their energy from the internal (spin) degrees of freedom, and it is this energy transfer that ultimately damps the spin mixing. On the other hand, if the spinor condensate is driven to its ferromagnetic ground state, as shown in Fig. 7.4b, there is no internal (spin) energy available for the motional degrees of freedom, and spatial spin structures cannot form. Indeed in this case, the three spin components are observed to have the same spatial wave function and appear to be miscible. The details of this study will be shown in Chapter 8

The observation of coherent spinor dynamics in a ferromagnetic spin-1 system described here paves the way for a host of future explorations. These systems are predicted to manifest complex quantum correlated states exhibiting entanglement and squeezing, and in general, it will be very interesting to explore the regime of small atom number < 1000, where sub-shot noise effects should become important [54]. Viewing the spin-mixing dynamics as a type of internal Josephson effect, many future explorations and manipulations of the system can be envisaged following along the path of superconducting weak-links. Finally, the coupling of the internal dynamics to the spatial wave function can be avoided in future experiments by either decreasing the condensate radii relative to the spin healing length ξ_s and/or operating at high magnetic fields where the time scales for mixing and damping are better separated. On the other hand, the coupling of the internal and external degrees of freedom in this system provide a new system for exploring nonlinear atom optical phenomena such as spatial-temporal dynamics of four-wave mixing [143].

Coherence spin-mixing have also been demonstrated in a Mott state of atoms on a lattice [144]. Their experiment involves a system of many copies of two atoms in each lattice site. On the other hand, our system involves a few hundred thousand atoms and the observed coherence reflects the presence of macroscopic spinor fields. High field oscillations have also been observed in an experiment in Hamburg [145].

CHAPTER VIII

SPIN DOMAIN FORMATION IN FERROMAGNETIC SPIN-1 CONDENSATES

In this chapter, we focus on the spatial dynamics of spinor condensates leading to formation of spatial spin structures, including spin waves and domains in 2- and 3-component mixtures of the spin states. As seen in previous chapters, although the spin-dependent interaction (or $|c_2|$) is typically one to two orders of magnitude smaller than the spin-independent interaction (or c_0), it has dramatic effects on the spinor dynamics and spin structures. Furthermore the sign of c_2 determines the nature of the spinor ground states as well as other dynamical properties [42, 44, 45, 52, 53]. For instance, the miscibility of different 2-component mixtures of the spin states is determined by the sign of c_2. This feature was used by the MIT group to determine that, in the case of ^{23}Na, $c_2 > 0$, which corresponds to anti-ferromagnetic spinor ground state [42]. For ^{87}Rb $F = 1$ spinor condensates, c_2 was predicted to be less than zero corresponding to a ferromagnetic ground state [55, 56]. Measurements of spin relaxation confirmed this prediction [44, 45].

As shown in Fig. 8.1, the spinor condensates created in this trap have a rich spatial spin structure consisting of well-segregated domains formed along the weak, axial trap direction.

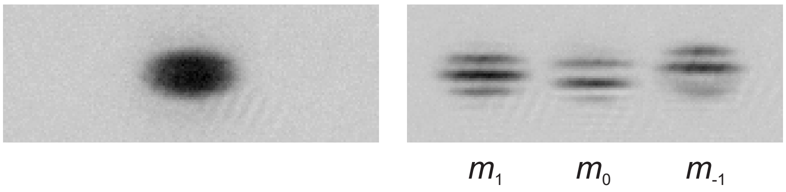

Figure 8.1: (left) Absorptive image of spinor condensate directly created in the optical trap showing the total column density of all spin components. (right) 'Stern-Gerlach' absorptive image of a spinor condensate taken with a weak magnetic field gradient applied during time of flight to separate the three spin states in space. The spinor condensate appears to be fragmented and presenting well segregated spin domains in all three spin states along the weak trap direction (z axis). For both images, the condensates are probed after 15 ms of time of flight and the field of view is 480 × 180 μm^2.

On the other hand, the total density profile shows little structure and is well described by the standard Thomas-Fermi wave function. The size of the observed spin domains is 21 μm, which is comparable to the spin healing length, $\xi_s \approx 15$ μm. The observed spin domains appear to be created simultaneously with the formation of the 3-component condensate. To study domain formation from a more controllable initial condition, we start with preparing condensates all in the m_{-1} state developed in our previous experiment [45]. We then create 2-component condensates by using phase coherent microwave pulses tuned to $F = 1 \leftrightarrow F = 2$ transitions and 3-component condensates via subsequent coherent spin mixing following initial spin state preparation [146].

Recall the coupled Gross-Pitaevskii (GP) equations for the order parameters of a spin-1 condensate:

$$\begin{aligned} i\hbar\frac{\partial\psi_{\pm1}}{\partial t} &= L_{\pm1}\psi_{\pm1} + c_2(n_0 + n_{\pm1} - n_{\mp1})\psi_{\pm1} + c_2\psi_0^2\psi_{\pm1}^* && (8.1)\\ i\hbar\frac{\partial\psi_0}{\partial t} &= L_0\psi_0 + c_2(n_1 + n_{-1})\psi_0 + 2c_2\psi_0^*\psi_1\psi_{-1}, && (8.2)\end{aligned}$$

where $L_{\pm1,0} = -\hbar^2\nabla^2/2m + V_t + E_{\pm1,0} + c_0 n$. The terms V_t, $E_{\pm1,0}$ and $n_{\pm1,0}$ are the trapping potential, Zeeman energies and densities for corresponding Zeeman projections $m_{\pm1,0}$, with the total density $n = n_1 + n_0 + n_{-1}$. Two types of binary interactions presented here are density and spin mean-field interactions, which are led by c_0 and c_2 coefficient respectively. The second term in Eqs. 8.1-8.2, led by c_2 coefficient, represents cross-phase modulation (or particle exchange collisions), and it results in the (im)miscibility of different Zeeman projections which can lead to phase separation and spin domain formation of two-component superfluids. The last term in Eqs. 8.1-8.2 is responsible for coherent spin mixing (or spin changing collisions) which causes spin populations to coherently interconvert among different Zeeman states, and provides a path to relax to a lower energy spin configuration in the presence of dissipation [42, 44, 45].

While the magnitude, $|c_2|n$, determines the time scale of the spinor dynamics, the sign of c_2 determines the magnetic properties of the spinors and the dynamical stability of spinor dynamics. Indeed, a spin-1 condensate offers a model system to study nonlinear atom optics [146, 147, 148] — the external and internal dynamics are generally inseparable, which provides a matter wave analogy of optical four-wave mixing in nonlinear media, and is ideal for studying nonlinear, spatio-temporal dynamics. On the other hand, under certain conditions the external and internal dynamics can be decoupled which greatly simplify the dynamics and allows studies of different spinor dynamics in greater detail.

When the available spin interaction energy is insufficient to create spatial spin domains, the external dynamics will be suppressed. This can occur when the spin healing length ξ_s is larger than the dimension of the condensate, and $\psi_{\pm1,0}$ share the same simple spatial wave function, known as the single-mode approximation (SMA) [39, 40]. This leads to a great simplification of Eq. 8.1-8.2. The internal dynamics are determined by $\rho_0(t)$, the fractional population of the m_0 state, and the spinor phase $\phi(t) \equiv \phi_1 + \phi_{-1} - 2\phi_0$, where ϕ_i is the phase of the m_i state. The populations of the other states are directly determined by $\rho_{\pm1} = (1 - \rho_0 \pm M)/2$, where $M = (N_1 - N_{-1})/N$ is the normalized global magnetism which is conserved, and N_i is the number of atoms in the m_i state with $N = N_{-1} + N_0 + N_1$. Within the SMA, the ground state spin populations and relative phase are readily found for arbitrary magnetization and magnetic field by minimizing the single mode Hamiltonian, $E = c\rho_0 \left[(1 - \rho_0) + \sqrt{(1 - \rho_0)^2 - M^2} \cos\theta\right] + \delta(1 - \rho_0)$, [146, 114, 117]. In particular, for $c_2 < 0$, the energy of the system at low fields is minimized for spinor phase $\phi = 0$ and population $\rho_0 = (1 - M^2)/2$. For other non-equilibrium populations or phases, the system will have excess spin energy that can drive a coherent evolution of the spinor system.

The results in the previous chapter have shown that the magnitude and rate of the coherent spin mixing can be tuned and even suppressed [146, 117]. In a field regime where the external quadratic Zeeman effect δ overrides internal spinor interactions, or $\delta \gg |c_2|n$, the system exhibits fast and small amplitude oscillations analogues to AC-Josephson oscillations with $\rho_0(t) \propto \delta^{-1} \sin 2\delta t$ [146]. Therefore, one can readily tune the amplitude of spin mixing to arbitrarily small values by applying a high biased magnetic field. E.g., for ^{87}Rb $F = 1$ condensate, if m_1 component is removed and a field of > 500 mG is applied, the amplitude of spin population oscillations can be reduced to $< 1\%$ of the total population [146, 117]. This type of 2-component systems was used to determine the miscibility of different spin components in anti-ferromagnetic Na spinor condensates [52]. The control and separation of two different types of spinor dynamics in the last chapter and in this chapter allow us to study the spatial spinor dynamics solely, or the interplay between these dynamics and coherent spin mixing which naturally occurs in spin-1 condensates.

8.1 Miscibility of Spin Components

The miscibility of different spin components are simply determined by the system energy. If the total system energy is lower when different components overlap compared to that when they are spatially (phase) separated, then they are miscible; otherwise, they are immiscible. The mean-field energy of the spinors can be obtained directly from the interaction Hamiltonian, Eq. 5.17. Recall that, in the mean-field limit, quantum fluctuations can be ignored and the spinor field operators can be replaced with the ground state order parameters, whose magnitudes are the square root of the densities, *i.e.*,

$$\begin{aligned}\mathbf{\Psi}_i &\rightarrow \psi_i \sim \sqrt{n_i}, &(8.3)\\ \mathbf{\Psi}_i^\dagger &\rightarrow \psi_i^* \sim \sqrt{n_i}, &(8.4)\end{aligned}$$

where $i = 1, 0, -1$. Here $\mathbf{\Psi}_i$, ψ_i, and $\sim \sqrt{n_i}$ are the field operator, order parameter, and the density of the ith spin component. Applying the above approximation to Eq. (5.17), the mean-field energy is given by

$$\begin{aligned}E_{MF} &= \frac{1}{2}\int \mathrm{d}^3r\{g_1 n_1^2 + g_0 n_0^2 + g_{-1} n_{-1}^2\\ &\quad +2g_{10}n_1n_0 + 2g_{1-1}n_1n_{-1} + 2g_{0-1}n_0n_{-1}\\ &\quad +4g_{1-1,00}n_0\sqrt{n_1n_{-1}}\}, \qquad (8.5)\end{aligned}$$

where g's are the mean-field interaction coefficients. In particular, $g_{a,b}$, g_{ab}, and $g_{1-1,00}$ stand for the one-fluid (self), two-fluid (cross-state), and three-fluid interaction coefficients. The values of g's are listed in Table 5.1.

Eq. (8.5) can be readily applied to determine the miscibility of two-component condensates. For a two-component condensate, it reduces to

$$E = \frac{1}{2}\int (g_a n_a^2 + g_b n_b^2 + 2g_{ab}n_an_b)\mathrm{d}^3r, \qquad (8.6)$$

If we assume equal population and homogeneous density for simplicity, the mean-field energy for the case of overlapped condensate is simply given as

$$E_o = \frac{N^2}{2V}\left(g_a + g_b + 2g_{ab}\right), \tag{8.7}$$

where N is the total number of atoms and V is the volume of the condensate. Similarly, the total mean-field energy for the case of phase separation is given as

$$E_s = \frac{N^2}{2}\left(\frac{g_a}{V_a} + \frac{g_b}{V_b}\right), \tag{8.8}$$

with the condition of equal pressure $n_a^2 g_a = n_b^2 g_b$ at equilibrium. When $E_o < E_s$ or when $g_{ab} < \sqrt{g_a g_b}$, two components are miscible; otherwise, they are immiscible [149, 123].

To study the miscibility of different spin components, we prepare two-component condensates with 75,000 atoms in each spin component [146] and allow them to evolve freely in the optical trap before probing. To reduce the spin mixing amplitude the magnetic field is kept > 420 mG, either along the tight (radial) or weak (axial) trap directions. When the magnetic field is along the weak trap direction, the field gradient is also compensated to < 0.2 mG/cm to minimize the phase separation caused by mechanical forces of the field gradient. For ^{87}Rb spin-1 spinors, the density mean-field, c_0, and spin-spin mean-field, c_2, were estimated to be 7.79×10^{-12} Hz·cm^3 and -3.61×10^{-14} Hz·cm^3 respectively. The interaction coefficients for intra- and inter- spin states are listed in Table 5.1, and their values are found to be $g_{\pm1,0} = g_{\pm1} = c_0 + c_2 = 7.76 \times 10^{-12}$ Hz·cm^3, $g_0 = c_0 = 7.79 \times 10^{-12}$ Hz·cm^3, and $g_{1,-1} = c_0 - c_2 = 7.83 \times 10^{-12}$ Hz·cm^3 [55, 56]. It is readily found that $g_{0,\pm1} < \sqrt{g_0 g_{\pm1}}$ and $g_{1,-1} < \sqrt{g_{-1} g_1}$, therefore, m_0 and $m_{\pm1}$ states should be miscible and m_1 and m_{-1} states should be immiscible. Our observations in Fig. 8.2 confirm those predictions and are consistent with the previous observations of ferromagnetic behaviors of $F = 1$ ^{87}Rb spinors [44, 45, 146]. We also notice that miscible condensates can still form domains when the large condensates are agitated.

While the miscibility of a 2-component system is determined by the intra- and cross-component mean-field interactions, number of spin domains formed, however, is determined by the total spin (internal) energy accessible to the spatial (external) degrees of freedom of the condensates. In a spin-1/2 condensate, spin mixing does not occur, and particle

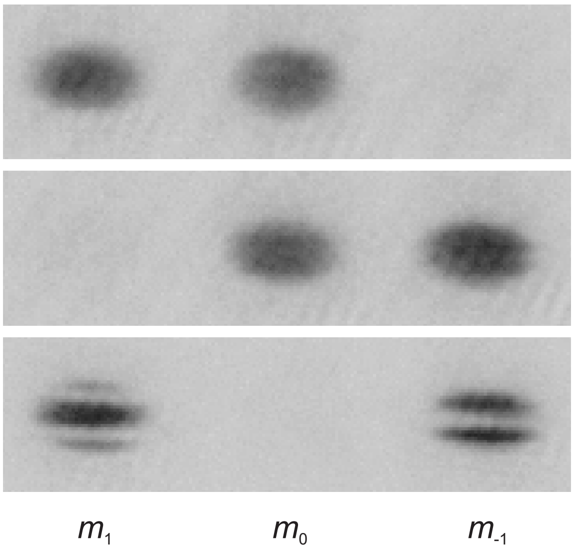

Figure 8.2: Stern-Gerlach absorptive images of 2-component condensates that are allowed to evolve for 500 ms in a field of 420 mG. Domain formation in the lower frame indicates the immiscibility of the m±1 states while the lack of domains in the other frames indicates the miscibility of m_0 and the other two states.

exchange collisions, which correspond to the two-fluid mean-field interactions, are solely responsible for the spinor dynamics. Under the presence of dissipation, relaxation to the ground state should lead two immiscible components to complete spatial (phase) separation. The formation of interlaced domains such as in Fig. 8.1 and 8.2 indicates incomplete relaxation, and the released internal spin energy is stored as the quantum pressure or the kinetic energy of the spinor condensates, which is revealed as complicated spinor order parameters or meta-stable spatial domains [52].

8.2 Spin Wave and Domain Formation in Ferromagnetic Condensates

In a spin-1 system, the spinor mean-field energy not only causes spin domain formation, but also can drive coherent spin mixing as shown in Chapter 7. When the condensate's dimension is larger than its spin healing length, the spin mixing dynamics are unstable [150] and perturbations can cause irreversibly conversion of the internal spin energy to external kinetic energy, forming meta-stable domains. This mechanism leads to the invalidity of the SMA. To demonstrate that spatial domains are induced by dynamical instability of spin mixing, we initiate coherent spin mixing with initial fractional spin populations $(0, 0.75, 0.25)$ and allow condensates to evolve freely until the amplitude of population oscillations are damped out. Fig. 8.3.a and 8.3.b show both the theoretical and experiment studies of the spatial-temporal dynamics of all three spin components along the weak trap direction. In the theoretical modelling, small amplitude noises at level of 10^{-5} are added to the order parameters of all three components at time zero [150, 151]. Our simulation shows that spin mixing causes non-stationary spatial variation in each spin component. This spatial variation presents a spin wave and persists for few seconds until the small noise is amplified to a level where the symmetry of this pattern is broken [150]. Experimental observations shown in Fig. 8.3.b verifies this type of spin waves; however, they only revive during the first 3 mixing cycles which indicates much larger noise, and this quickly leads to localization of wave fronts which serves to damp the spin mixing. Once the spin mixing is mostly damped out each fragment is settled to a spin domain.

To demonstrate that energy stored in the 3-component spin domains is derived from the internal energy used to drive spin mixing, and to identify the miscibility of 3-component condensate in the ground state, we perform the following experiment. We create a condensate with non-equilibrium spin population $(0, 1/2, 1/2)$ and allow the coherent spin mixing to take place in a low field. After mixing for 50 ms in which the spin populations reaches the ground state configuration, $(1/16, 3/8, 9/16)$, we impart a phase shift to bring the spinor condensate to its ferromagnetic ground state as demonstrated in Chapter 7 [146]. Fig. 8.4.a shows that all three components appear to be miscible and remain single domain thereafter. This indicates that domains will not form without excess kinetic energy, even when the condensate dimension is larger than the spin healing length. On the other hand, since the ground state should be a single-domain, it suggests that the formation of multiple domains indicates incomplete relaxation of the internal spin mean-field energy [52]. We notice in Fig. 8.4.b that although all three components appear to be miscible in the ferromagnetic ground state, $m_{\pm 1}$ components still tend to avoid each other. However, since the m_1 component is much smaller than the m_{-1} component, they are in weak-segregation phase and are inter-penetrated [149]. At 0.3 s we impart a second phase shift to move the spinor

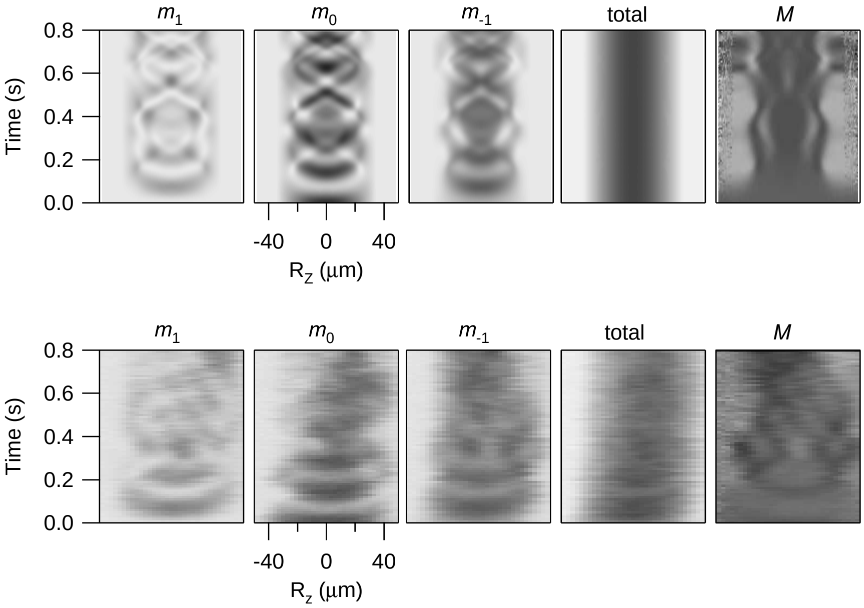

Figure 8.3: Spin waves and domain formation of ferromagnetic spin-1 condensates. Spin mixing is initiated with non-equilibrium spin populations, and density profiles of all three spin components along the weak trap direction (z axis) are plotted against mixing time. a) Numerical integration of Eq. 8.1-8.2 for initial fractional population $(0, 0.75, 0.25)$ with 10^{-5} initial amplitude noises on the order parameters. b) Experimental observations with the same initial spin population in a. Spin waves, referring to the non-stationary crescent shaped patterns in all three components, are initiated due to the coupling of spin mixing to spatial dynamics. After 3 revivals, spin wave fronts are fragmented which serves to damp the spin mixing, and each fragment eventually localized to form a spin domain.

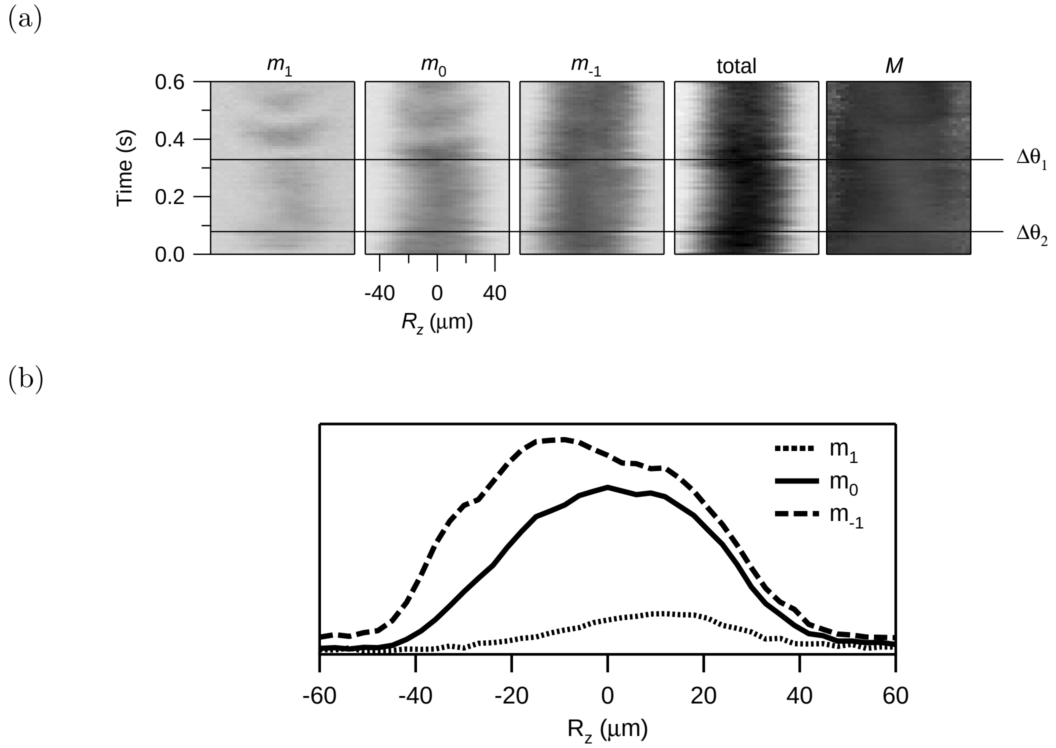

Figure 8.4: Miscibility of the ferromagnetic ground state. (a) A condensate with initial populations (0, 0.5, 0.5) is allow to spin mix for 50 ms and then coherently driven to its ferromagnetic ground state [146]. In this lowest internal energy state, all three condensates appear to be single-domain and are miscible. At 0.3 s the spinor condensate is driven away from its ground state, and spin mixing and spin waves are re-initiated. Note that the scale of optical density of m_1 component is reduced by 2 to enhance visual contrast. (b) Density plot at 120 ms. Although the three spin components are miscible in the ground state, however, m_1 and m_{-1} components still tend to avoid each other.

condensate out of the ground state to reinitiate spin mixing, and again the spin waves are immediately excited along the weak trap direction. This verifies that in a spin-1 condensate, the energy for initiating spatial (external) dynamics is derived from the internal spinor energy used to drive spin mixing.

It has been suggested that the dynamical instability in ferromagnetic spinors may be behind the spontaneous symmetry breaking of spin waves and domain formation [150]. This is because all of the spin mixing orbits, such as those equi-energy contours shown in Fig. 7.4.b, including the orbits near the ferromagnetic ground state, are unstable and are susceptible to the perturbations of noise. To investigate that, we initiate spin mixing with different initial spin population configurations which associate with different total spin energy. Here we illustrate the spin mixing with initial spin configurations of (0, 0.5, 0.5), and (0, 0.83, 0.17), and the experimental data are displayed in Fig. 8.5. The (0, 0.5, 0.5) configuration is closer to the ferromagnetic ground state, and possesses less spinor energy for driving the spin mixing. The second configuration is farther away from the ground state. As shown in Fig. 8.5.a, spin mixing and spin waves revive for 5 mixing cycles before three components phase separate, which is longer than in the case of Fig. 8.3.b. In contrast, spin mixing and spin waves do not revive as seen in Fig. 8.5.b. These measurements suggest that the degree of instability depends on the initial spinor energy; system with higher initial spinor energy is more unstable. These measurements suggest that dynamical instability indeed plays a role in domain formation.

Note that in the configuration shown in Fig. 8.5.b, it is observed in that m_0 component occupies the trap center at the onset of symmetry breaking, and the m_1 component is repealed to the edge of the trap. This is due to that m_0 state is the largest component, and m_1 component is the smallest one [R]. The magnetic field gradient, similar to other noises, may provide a small initial seed for unstable spinor modes, however, it is unlikely to be responsible for the separation of spin components and domain formation as can be seen in Fig. 8.5.b. In addition, release of higher internal spinor energy in the last case also leads to more complicated spatial spin domains. This test provides the evidence that the dynamical instability plays an important role in spontaneous domain formation.

8.3 Study of The Validity of Single-Mode Approximation

In the previous sections, the single focused trap has allowed us to study the 1D spatial dynamics on a cigar shaped condensate in the trap, for the condensate size is larger than the spin healing length along the axial direction. Is is of interest to compare the spin mixing with and without the interplay with spatial dynamics. Fig. 8.6 lists three trap geometries and the typical condensate size in these traps. For a typical density of 10^{14} cm^{-3}, the spin healing length in ^{87}Rb is 10 - 15 μm. Therefore, the condensate size in the isotropic (cross) trap and disk trap (lattice) is smaller than the spin healing length, and SMA may apply. To investigate that, we perform spin mixing in a condensate created in an isotropic (cross)

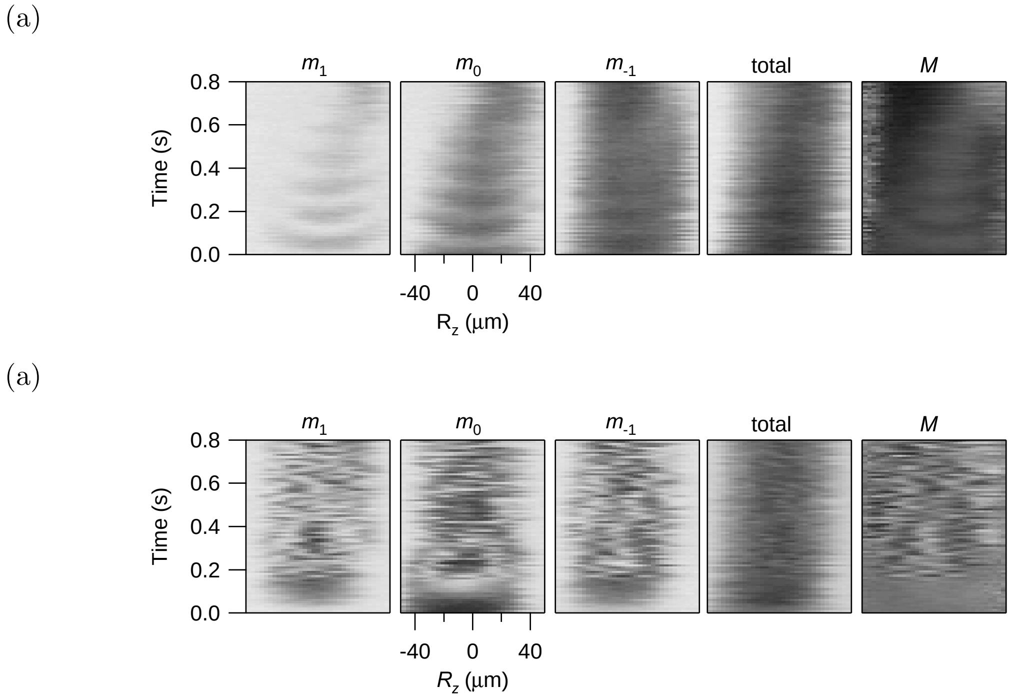

Figure 8.5: Dynamical instability of spin mixing. a) Spin mixing is initiated in a condensate with spin configuration of (0, 0.5, 0.5). It is observed that spin waves are revived for 5 mixing cycles before phase separation of spin components. b) For a spin configuration of (0, 0.83, 0.17), spin waves do not revive, and domains form much quicker than in the case of a.

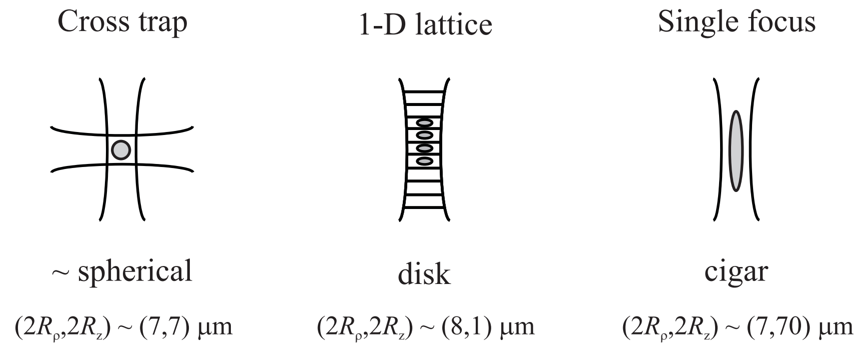

Figure 8.6: Trap geometry comparison. Condensates created in the cross trap and 1D lattice have smaller condensate size than the spin healing length.

optical trap. The condensate contains 48,000 atoms, and the trap frequency is $2\pi \times 230$ rad/s. In this case the spin healing length is 11 μm while the condensate diameter is only 7 μm. We observe 12 clear spin population oscillations, during which no spin waves (crescent shaped patterns) and domain are formed in the two directions shown in our images. The joint density plot along the axial direction are shown in Fig. 8.7.a, and plots of spin population oscillation vs. time for the condensates in the cross trap and in the single focus trap are displayed in Fig. 8.7.b. In the second plot, the coherent spin population oscillation in the cross trap damps out with a time constant of 3 sec, while the damping time constant is $<$ 250 ms in the single focus trap. Our observations suggests that the SMA remains valid when the condensate dimension is less than the spin healing length. When the SMA is valid, the spinor energy is kept in the internal degrees of freedom which leads to larger oscillation amplitude for longer time.

In summary, we have studied the miscibility and spin domain formation dynamics of a ferromagnetic spin-1 condensate, and we show that spin domain formation is induced by the spatial or spatio-temporal dynamics. We also show that in a spin-1 condensate, the kinetic energy stored in multi-domains is derived from internal spin energy. When this energy is not accessible or the condensate dimension is smaller its spin healing length, which characterizes the smallest stable domain, different spin components appear to be miscible and remain single domain. The implication of our observations and in this chapter and the last chapter therefore points to the validity of the coupled Gross-Pitaevskii equations used to describe spinor condensates, and verify that this spin-1 condensate is essentially the

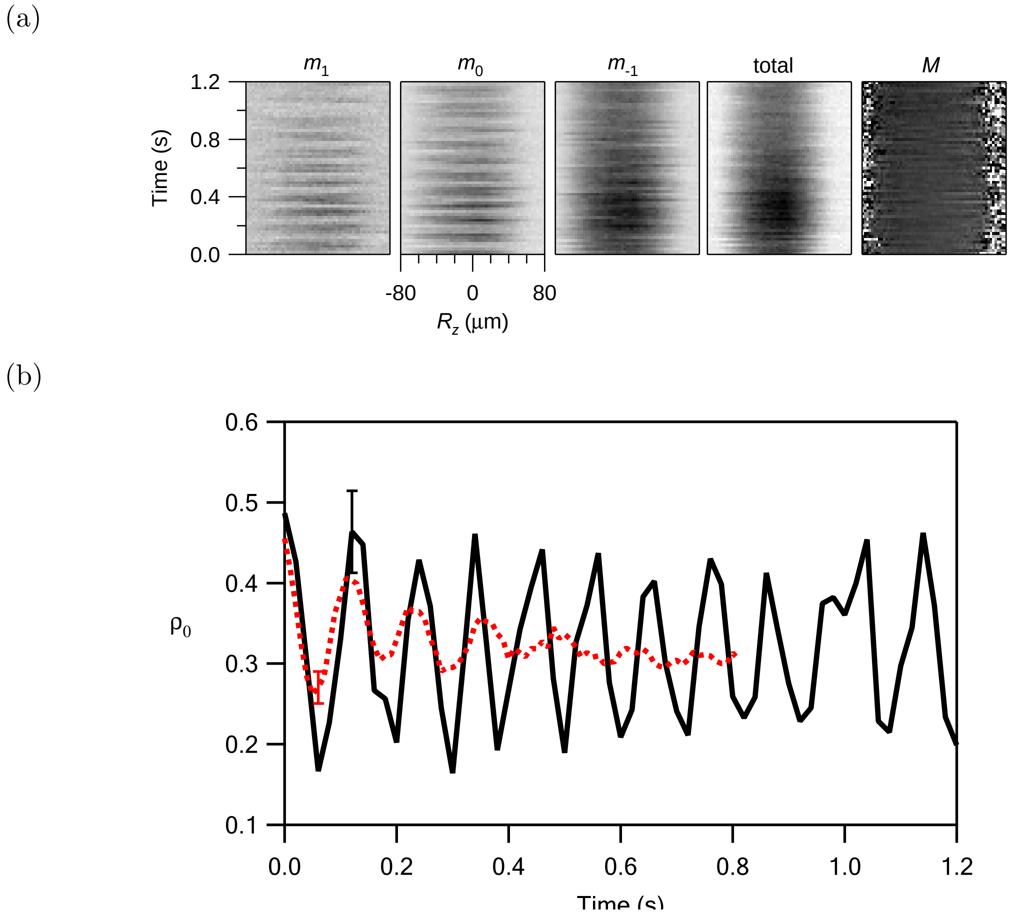

Figure 8.7: Spin mixing vs. the single-mode approximation (SMA). (a) To test the validity of the SMA, spin mixing is initiated in a crossed (isotropic) optical trap with initial fractional populations (0, 0.5, 0.5). Spin population oscillations up to 12 cycles are observed over 1.2 s during which no resolvable spin wave is observed (solid curve). The images are taken after 15 ms of free expansion. (b) The solid curve is the spin mixing results in the cross trap, and the dotted curve is the results in the single focus trap. The coherent spin mixing in the single focus trap damps out with a time constant of < 250 ms, while in the case of cross trap, the damping time constant is 3 s.

atomic matter wave analogue of optical four-wave mixing in nonlinear optical media [147]. This system thus provides a model for future studies on nonlinear dynamics, such as spinor solitons and quantum chaos.

CHAPTER IX

FINAL REMARKS

In this thesis, we have described how we have successfully extended our all-optical BEC technique to two new optical trap geometries. We can routinely create Bose-Einstein condensates by directly loading from a MOT with all three optical geometries. These three geometries have proven to play important roles in the studies of spinor condensates. While earlier experiments on spin-1 condensates were done with anti-ferromagnetic Na [42, 53, 52], our studies on the ferromagnetic ^{87}Rb spin-1 condensates have provided the other half of the physical picture for spin-1 spinor condensates.

We have observed spin mixing dynamics in ^{87}Rb $F = 1$ spinors and also in the excited $F = 2$ spinors, from which we confirmed the predicted ferromagnetic nature of ^{87}Rb ground ($F = 1$) state. In the second spinor experiment, we have unambiguously observed the coherent spin mixing by engineering the initial spin population and spinor phase, and from which we determined the spin-dependent interaction strength. We have also demonstrated coherent control of spin mixing, in which we drove the spinor condensate to and away from its ferromagnetic ground state. Using this method, we have measured the decoherence time of the ferromagnetic ground state.

The single focus trap geometry has allowed us to study spin domain formation and spatio-temporal dynamics of spinor condensates. Our studies on coherent spin mixing and spatial spinor dynamics thus validate the coupled Gross-Pitaevskii equations used to describe spin-1 condensates. This system is an atomic analogue to four-wave mixing of a laser beam in Kerr media [147]. In the future this spin-1 condensate system will provide a model system for studying atomic four-wave mixing and atom optics.

Coherent spin mixing is a type of internal Josephson oscillator, and therefore one can expect to observe phenomena related to the Josephson effects in weak-linked superconductors, such as dynamical localization or the so-called Shapiro effects [142, 128, 124, 131].

In order to observe this effect, stable and persistent spin population oscillations are required. To achieve that, the single-mode approximation needs to be satisfied. We have demonstrated that the cross trap geometry can forbid excitation of spatial spin waves and continue spin mixing for longer time. The spin mixing frequency is proportional to the condensate density, therefore reducing condensate density fluctuations should allow more stable spin mixing rate. Alternatively, spin mixing in a high magnetic field should bring the spin mixing to a regime where the external quadratic Zeeman effect dominates internal spin interactions. In this regime, spin mixing will be independent of the condensate density. The downside, however, is that the spin mixing amplitude is small in a high field and fluctuations of population from shot to shot will eventually limit the observation of spin mixing. In the future, creating condensates in the cross trap with fewer fluctuations in total population and density will be the key to increasing the number of oscillations.

Currently, our studies on spinor dynamics are in the mean-field limit regime where quantum fluctuations are small and thus are neglected, and the spinor dynamics is well-described by the Gross-Pitaevskii equation. When the condensate size contains only one thousand atoms or less, quantum fluctuations become prominent and cannot be neglected [54, 113]. This should allow us to study quantum spin mixing, or the so-called quantum atom optics. In particular, this spin-1 system has been predicted to possess complex ground states, spin squeezing, and spin entanglement via quantum spin mixing [54, 120, 132]. We have previously observed reduced noise on magnetization, in the future, developing new imaging techniques which is capable of shot-noise limit detection on only few hundred atoms should allow us to study spin squeezing directly.

APPENDIX A

TABLE OF CONSTANTS AND PROPERTIES OF ^{87}RB

Table A.1: Fundamental constants (2002 CODATA recommended values) and useful ^{87}Rb properties [57].

Quantity	Symbol	Value
Fundamental Constants		
Speed of Light	c	$2.997\,924\,58\times10^{8}$ m/s (exact)
Permeability of Vacuum	μ_0	$4\pi\times10^{-7}$ N/A^2 (exact)
Permittivity of Vacuum	ϵ_0	$(\mu_0 c^2)^{-1}$
Planck Constant	h	$6.626\,069\,3(11)\times10^{-34}$ J s
Elementary Charge	e	$1.602\,176\,53(14)\times10^{-19}$ C
Bohr Magneton	μ_B	$9.274\,009\,49(80)\times10^{-24}$ J/T
Bohr Radius	a_0	$0.529\,177\,208\,3(19)\times10^{-10}$ m
Bolzman Constant	k_B	$1.380\,650\,3(24)\times10^{-23}$ J/K
Basic Properties of ^{87}Rb		
Atomic Number	Z	37
Atomic Mass	m	$1.44316060(11)\times10^{-25}$ kg
Natural Abundance		27.83%
Nuclear Spin	I	3/2
Ground ($5^2\mathrm{S}_{1/2}$) State Properties		
Fine structure Landé g-factor	g_J	2.002 319 304 373 7(80)
Nuclear g-factor	g_I	-0.000995 141 4(10)
Hyperfine Splitting	ν_hf	6,834,682,610.90434(3) Hz
D_2 ($5^2\mathrm{S}_{1/2}\rightarrow 5^2P_{3/2}$) Transition		
Wavelength (vacuum)	λ	780.241 209 686(13) nm
Lifetime	τ	26.24(4) ns
Decay Rate	Γ	$2\pi\cdot6.065(9)$ MHz
$\lvert F=2, m_F=\pm2\rangle\rightarrow\lvert F'=3, m_F=\pm3\rangle$		
Saturation Intensity	I_sat	1.669(2) mW/cm^2
Resonance Cross Section	σ_0	2.907×10^{-9} cm^2
Scattering Lengths (s-wave)		
scattering length for spin-0 channel	$a_{F=0}$	101.8(2) a_0
scattering length for spin-2 channel	$a_{F=2}$	100.4(1) a_0

APPENDIX B

SPINOR DEGREES OF FREEDOM OF TWO SPIN-F ATOMS UNDER COLLISION

Let $N = 2f + 1$, which represents the number of internal (Zeeman) states of a spin-f particle. Then for two spin-f particles, the possible input channels are N^2. However, exchange symmetry ($g_{ij,kl} = g_{ji,kl}$) leads to only $N^2 - C_2^N = N^2 - \frac{N(N-1)}{2!} = \frac{N(N+1)}{2}$ input channels. By the same token, for each input channel, there are $\frac{N(N+1)}{2}(\equiv z)$ possible output channels, without considering spin conservation. For the first input channel (if we label those channels), there are z possible output channels. However, for the second input channel, there are only $z-1$ output channels, since it contains a time-reversal ($g_{ij,kl} = g_{kl,ij}$) of one of the cases already counted in the first input channel. So, the total free parameters are

$$\begin{aligned}
\nu &= z^2 - [1 + 2 + \cdots + (z-1)] \\
&= z^2 - \frac{1}{2}z(z-1) \\
&= [\frac{N(N+1)}{2}]^2 - \frac{1}{2}[\frac{N(N+1)}{2}][\frac{N(N+1)}{2} - 1] \\
&= \frac{1}{2}[\frac{N(N+1)}{2}]^2 + \frac{1}{2}[\frac{N(N+1)}{2}] \\
&= \frac{1}{2}\frac{N(N+1)}{2}[\frac{N(N+1)}{2} + 1] \\
&= \frac{1}{8}(N^2 + N)(N^2 + N + 2). \qquad \text{(B.1)}
\end{aligned}$$

In the case of two spin-1 particles ($F = 1$), there are 6 input channels under exchange symmetry, say, $(1,1), (1,0), (1,-1), (0,0), (0,-1)$,and $(-1,-1)$. And for each input channel, we have:

$(1,1) \rightarrow (1,1), (1,0), (1,-1), (0,0), (0,-1), (-1,-1)$:6 output channels under exchange symmetry condition.

$(1,0) \to (1,0),(1,-1),(0,0),(0,-1),(-1,-1)$: 5 output channels, we exclude the output channel $(1,1)$, since $(1,0) \to (1,1)$ is the time-reversal of $(1,1) \to (1,0)$.

$(1,-1) \to (1,-1),(0,0),(0,-1),(-1,-1)$: 4 output channels.

$\ldots$

Therefore, there are only $6+5+4+3+2+1 = 21$ free parameters need to be considered.

By using Eq. (B.1), we have $N = 3$ and $\nu = \frac{1}{8}(3^2+3)(3^2+3+2) = 21$, which agrees with the above calculations.

APPENDIX C

SPIN COUPLING OF TWO SPIN-1 ATOMS

In a system of two coupled spin-1 bosons, the maximally aligned spin state is $|F=2, m_F=2\rangle = |f=1, m_f=1\rangle|f=1, m_f=1\rangle$. For convenient, here we define $|F, M\rangle = \chi^F_M$, and $|f_1=1, m\rangle = \chi^{(1)}_m$ and $|f_2=1, m\rangle = \chi^{(2)}_m$.

We can render the other M states using ladder operators:

$$F_\pm|F, M\rangle = \hbar\sqrt{F(F+1) - M(M\pm 1)}|F, M\pm 1\rangle.$$

Here $F_\pm$ is the rising/lowering operator for total spin. It can be expressed as the sum of two operators for two atoms,

$$F_\pm = f^{(1)}_\pm + f^{(2)}_\pm,$$

where $f^{(1,2)}_\pm$ are the rising/lowering operators for atoms 1,2. Therefore,

$$\begin{aligned} F_-\chi^2_2 &= (f^{(1)}_- + f^{(2)}_-)(\chi^{(1)}_1\chi^{(2)}_1) \\ &= \hbar\sqrt{2}(\chi^{(1)}_0\chi^{(2)}_1 + \chi^{(1)}_1\chi^{(2)}_0) \\ &= 2\hbar\{\frac{1}{\sqrt{2}}(\chi^{(1)}_0\chi^{(2)}_1 + \chi^{(1)}_1\chi^{(2)}_0)\} \\ &= 2\hbar\chi^2_{1,}. \end{aligned}$$

By comparison, we find $\chi^2_1 = \frac{1}{\sqrt{2}}(\chi^{(1)}_0\chi^{(2)}_1 + \chi^{(1)}_1\chi^{(2)}_0)$. Similarly, $\chi^2_0 = \frac{1}{\sqrt{6}}(2\chi^{(1)}_0\chi^{(2)}_0 + \chi^{(1)}_{-1}\chi^{(2)}_1 + \chi^{(1)}_1\chi^{(2)}_{-1})$, $\chi^2_{-1} = \frac{1}{\sqrt{2}}(\chi^{(1)}_{-1}\chi^{(2)}_0 + \chi^{(1)}_0\chi^{(2)}_{-1})$, and $\chi^2_{-2} = \chi^{(1)}_{-1}\chi^{(2)}_{-1}$.

Since χ^1_1 must be orthogonal to χ^2_1, it is straightforward to show that $\chi^1_1 = \frac{1}{\sqrt{2}}(\chi^{(1)}_1\chi^{(2)}_0 - \chi^{(1)}_0\chi^{(2)}_1)$. Applying the lowering operator to this state, we can further find $\chi^1_0 = \frac{1}{\sqrt{2}}(\chi^{(1)}_1\chi^{(2)}_{-1} - \chi^{(1)}_{-1}\chi^{(2)}_1)$, and $\chi^1_{-1} = \frac{1}{\sqrt{2}}(\chi^{(1)}_0\chi^{(2)}_{-1} - \chi^{(1)}_{-1}\chi^{(2)}_0)$.

Finally, since χ^0_0 must be orthogonal to χ^2_0 and χ^1_0, and given that $F_\pm\chi^0_0 = 0$, it can be shown that $\chi^0_0 = \frac{1}{\sqrt{3}}(\chi^{(1)}_0\chi^{(2)}_0 - \chi^{(1)}_1\chi^{(2)}_{-1} - \chi^{(1)}_{-1}\chi^{(2)}_1)$.

By observation, we find that the states in the $F=0,2$ ($F=1$) manifold are exchange symmetric (anti-symmetric). Therefore, when the total external wavefunction of two colliding atoms are symmetric, the allowed total spin channels are $F =$ even for bosons and $F =$ odd for fermions.

APPENDIX D

INTERACTION HAMILTONIAN OF SPIN-1 BOSE GAS

Recall Eq. 5.16:

$$\mathbf{H}_{int} = \frac{1}{2}\int d^3\vec{r}\{c_0\mathbf{\Psi}_i^\dagger\mathbf{\Psi}_j^\dagger\mathbf{\Psi}_j\mathbf{\Psi}_i + c_2\mathbf{\Psi}_i^\dagger\mathbf{\Psi}_j^\dagger(\vec{\mathbf{f}}_{jk}\cdot\vec{\mathbf{f}}_{il})\mathbf{\Psi}_k\mathbf{\Psi}_l\}. \tag{D.1}$$

The spin independent (c_0) term in Eq. D.1 is given by

$$\begin{aligned} & \frac{c_0}{2}\mathbf{\Psi}_i^\dagger\mathbf{\Psi}_j^\dagger\mathbf{\Psi}_j\mathbf{\Psi}_i \\ = \; & \frac{c_0}{2}[\mathbf{\Psi}_1^\dagger\mathbf{\Psi}_1^\dagger\mathbf{\Psi}_1\mathbf{\Psi}_1 + \mathbf{\Psi}_0^\dagger\mathbf{\Psi}_0^\dagger\mathbf{\Psi}_0\mathbf{\Psi}_0 + \\ & \mathbf{\Psi}_{-1}^\dagger\mathbf{\Psi}_{-1}^\dagger\mathbf{\Psi}_{-1}\mathbf{\Psi}_{-1} + 2\mathbf{\Psi}_1^\dagger\mathbf{\Psi}_0^\dagger\mathbf{\Psi}_0\mathbf{\Psi}_1 + \\ & 2\mathbf{\Psi}_1^\dagger\mathbf{\Psi}_{-1}^\dagger\mathbf{\Psi}_{-1}\mathbf{\Psi}_1 + 2\mathbf{\Psi}_0^\dagger\mathbf{\Psi}_{-1}^\dagger\mathbf{\Psi}_{-1}\mathbf{\Psi}_0]. \end{aligned} \tag{D.2}$$

The spin dependent (c_2) terms are given by

$$c_2\mathbf{\Psi}_i^\dagger\mathbf{\Psi}_j^\dagger(\vec{\mathbf{f}}_{jk}\cdot\vec{\mathbf{f}}_{il})\mathbf{\Psi}_k\mathbf{\Psi}_l = \frac{c_2}{2}\mathbf{\Psi}_i^\dagger\mathbf{\Psi}_j^\dagger\{(\mathbf{f}_x)_{ik}(\mathbf{f}_x)_{jl} + (\mathbf{f}_y)_{ik}(\mathbf{f}_y)_{jl} + (\mathbf{f}_z)_{ik}(\mathbf{f}_z)_{jl}\}\mathbf{\Psi}_k\mathbf{\Psi}_l,$$

where $(\mathbf{f}_\alpha)_{ik}$ is the matrix element of the traceless Pauli spin-1 matrices, with $\alpha = x, y, z$ and $i, k = 1, 0, -1$. Given the spin-1 matrices,

$$\mathbf{f}_x = \frac{1}{\sqrt{2}}\begin{bmatrix} 0 & 1 & 0 \\ 1 & 0 & 1 \\ 0 & 1 & 0 \end{bmatrix}, \mathbf{f}_y = \frac{i}{\sqrt{2}}\begin{bmatrix} 0 & -1 & 0 \\ 1 & 0 & -1 \\ 0 & 1 & 0 \end{bmatrix}, \mathbf{f}_z = \begin{bmatrix} 1 & 0 & 0 \\ 0 & 0 & 0 \\ 0 & 0 & -1 \end{bmatrix},$$

We find

$$\mathbf{f}_x^{(1)}\mathbf{f}_x^{(2)} = [(f_x)_{10} + (f_x)_{01} + (f_x)_{0-1} + (f_x)_{-10}]^2, \tag{D.3a}$$

$$\begin{aligned} \mathbf{f}_y^{(1)}\mathbf{f}_y^{(2)} &= [(f_y)_{10} + (f_y)_{01} + (f_y)_{0-1} + (f_y)_{-10}]^2 \\ &= -\{[(f_x)_{01} + (f_x)_{-10}] - [(f_x)_{10} + (f_x)_{0-1}]\}^2, \end{aligned} \tag{D.3b}$$

$$\begin{aligned} \mathbf{f}_z^{(1)}\mathbf{f}_z^{(2)} &= [(f_z)_{11} + (f_z)_{-1-1}]^2 \\ &= (f_z)_{11}^2 + (f_z)_{-1-1}^2 + [(f_z)_{11}(f_z)_{-1-1} + h.c.]. \end{aligned} \tag{D.3c}$$

Combining Eq. (D.3a) and (D.3b), we have

$$\begin{aligned} & \mathbf{f}_x^{(1)}\mathbf{f}_x^{(2)} + \mathbf{f}_y^{(1)}\mathbf{f}_y^{(2)} \\ = \; & [(f_x)_{10} + (f_x)_{01} + (f_x)_{0-1} + (f_x)_{-10}]^2 - [-(f_x)_{10} + (f_x)_{01} - (f_x)_{0-1} + (f_x)_{-10}]^2 \\ = \; & 2\{[(f_x)_{01}(f_x)_{10} + (f_x)_{-10}(f_x)_{10} + (f_x)_{01}(f_x)_{0-1} + (f_x)_{-10}(f_x)_{0-1}] + h.c.\} \end{aligned} \tag{D.4}$$

Substitute Eq. (D.4) back into (D.1), we find

$$\begin{aligned} & \frac{c_2}{2}(\boldsymbol{\Psi}_i^\dagger\boldsymbol{\Psi}_j^\dagger[(\mathbf{f}_x)_{ik}(\mathbf{f}_x)_{jl} + (\mathbf{f}_y)_{ik}(\mathbf{f}_y)_{jl}]\boldsymbol{\Psi}_k\boldsymbol{\Psi}_l) \\ = \; & \frac{c_2}{2}2[\boldsymbol{\Psi}_1^\dagger\boldsymbol{\Psi}_0^\dagger\boldsymbol{\Psi}_0\boldsymbol{\Psi}_1 + \boldsymbol{\Psi}_1^\dagger\boldsymbol{\Psi}_{-1}^\dagger\boldsymbol{\Psi}_0\boldsymbol{\Psi}_0 + \boldsymbol{\Psi}_0^\dagger\boldsymbol{\Psi}_0^\dagger\boldsymbol{\Psi}_{-1}\boldsymbol{\Psi}_1 + \boldsymbol{\Psi}_0^\dagger\boldsymbol{\Psi}_{-1}^\dagger\boldsymbol{\Psi}_{-1}\boldsymbol{\Psi}_0] \end{aligned} \tag{D.5}$$

Similarly, substituting Eq. (D.3c) back into (D.1), we have

$$\begin{aligned} & \frac{c_2}{2}(\boldsymbol{\Psi}_i^\dagger\boldsymbol{\Psi}_j^\dagger(\mathbf{f}_z)_{ik}(\mathbf{f}_z)_{jl}\boldsymbol{\Psi}_k\boldsymbol{\Psi}_l) \\ = \; & \frac{c_2}{2}[\boldsymbol{\Psi}_1^\dagger\boldsymbol{\Psi}_1^\dagger\boldsymbol{\Psi}_1\boldsymbol{\Psi}_1 - 2\boldsymbol{\Psi}_1^\dagger\boldsymbol{\Psi}_{-1}^\dagger\boldsymbol{\Psi}_{-1}\boldsymbol{\Psi}_1 + \boldsymbol{\Psi}_{-1}^\dagger\boldsymbol{\Psi}_{-1}^\dagger\boldsymbol{\Psi}_{-1}\boldsymbol{\Psi}_{-1}] \end{aligned} \tag{D.6}$$

Combine eqn.(D.2), eqn.(D.6), and eqn.(D.5), we arrive at the interacting Hamiltonian,

$$\begin{aligned} \mathbf{H}_{int} &= \frac{1}{2}\int d^3\vec{r}\{c_0(\boldsymbol{\Psi}_i^\dagger\boldsymbol{\Psi}_j^\dagger\boldsymbol{\Psi}_j\boldsymbol{\Psi}_i) + c_2(\boldsymbol{\Psi}_i^\dagger\boldsymbol{\Psi}_j^\dagger[(\mathbf{f}_m)_{ik}(\mathbf{f}_m)_{jl}]\boldsymbol{\Psi}_k\boldsymbol{\Psi}_l)\} \\ &= \frac{1}{2}\int d^3\vec{r}\{(c_0+c_2)\boldsymbol{\Psi}_1^\dagger\boldsymbol{\Psi}_1^\dagger\boldsymbol{\Psi}_1\boldsymbol{\Psi}_1 + c_0\boldsymbol{\Psi}_0^\dagger\boldsymbol{\Psi}_0^\dagger\boldsymbol{\Psi}_0\boldsymbol{\Psi}_0 + (c_0+c_2)\boldsymbol{\Psi}_{-1}^\dagger\boldsymbol{\Psi}_{-1}^\dagger\boldsymbol{\Psi}_{-1}\boldsymbol{\Psi}_{-1} \\ &\quad +2(c_0+c_2)\boldsymbol{\Psi}_1^\dagger\boldsymbol{\Psi}_0^\dagger\boldsymbol{\Psi}_0\boldsymbol{\Psi}_1 + 2(c_0-c_2)\boldsymbol{\Psi}_1^\dagger\boldsymbol{\Psi}_{-1}^\dagger\boldsymbol{\Psi}_{-1}\boldsymbol{\Psi}_1 + 2(c_0+c_2)\boldsymbol{\Psi}_0^\dagger\boldsymbol{\Psi}_{-1}^\dagger\boldsymbol{\Psi}_{-1}\boldsymbol{\Psi}_0 \\ &\quad +2c_2\boldsymbol{\Psi}_{-1}^\dagger\boldsymbol{\Psi}_1^\dagger\boldsymbol{\Psi}_0\boldsymbol{\Psi}_0 + 2c_2\boldsymbol{\Psi}_0^\dagger\boldsymbol{\Psi}_0^\dagger\boldsymbol{\Psi}_{-1}\boldsymbol{\Psi}_1\}. \end{aligned}$$

APPENDIX E

SPINOR ENERGY FUNCTIONAL AND MEAN-FIELD GROUND STATES

The ground state is the minimal energy state, which can be obtained by minimizing the system energy. In the case where the density is homogeneous or when the single-mode approximation (SMA) is valid, the vectoral order parameter can be reduced to $\vec{\psi}(\vec{r}) = \sqrt{n(r)}(\zeta_1, \zeta_0, \zeta_{-1})^T$, and the mean-field ground state can be found by simply minimizing the following energy functional,

$$E = \int \mathrm{d}^3 r \psi_i^* \frac{-\hbar^2\nabla^2}{2m}\psi_i + n[V_{tr} - \mu + \frac{c_0 n}{2} + \frac{c_2 n}{2}\langle\vec{F}\rangle^2 + E_Z], \tag{E.1}$$

where V_{tr}, c_0, c_2, and E_z are the trapping potential, density interaction coefficient, spin interaction coefficient, and the Zeeman energy. Here $n = |\phi(r)|^2$ is the total density of the condensate, where $\phi(r)$ is the common spatial mode function. The total Zeeman energy in a B field is given by

$$E_Z = \sum_{i=1}^{3} E_i |\zeta_i|^2 = \sum_{i=1}^{3} E_i \rho_i, \tag{E.2}$$

where $\rho_i = |\zeta_i|^2$ with $\sum_{i=1}^3 \rho_i = 1$. Recall that the magnetization $M = \rho_1 - \rho_{-1}$ is a conserved quantity, then a spinor can be characterized by ρ_0 and M, and its Zeeman energy in an external field is given by

$$\begin{aligned} E_Z &= E_0\rho_0 + E_1\frac{1-\rho_0+M}{2} + E_{-1}\frac{1-\rho_0-M}{2} && \text{(E.3a)}\\ &= E_0 - M\frac{E_{-1}-E_1}{2} + (1-\rho_0)\frac{E_1+E_{-1}-2E_0}{2} && \text{(E.3b)}\\ &= E_0 - \eta M + \delta(1-\rho_0), && \text{(E.3c)} \end{aligned}$$

where $\eta = (E_{-1} - E_1)/2$ is the linear Zeeman shift, and $\delta = (E_1 + E_{-1} - 2E_0)/2$ is the quadratic Zeeman shift. However,

$$\begin{aligned} \langle F_z \rangle &= M, && \text{(E.4)} \\ \langle F_z^2 \rangle &= |\zeta_1|^2 + |\zeta_{-1}|^2 = 1 - \rho_0. && \text{(E.5)} \end{aligned}$$

By substitution, the Zeeman energy can be expressed as

$$E_Z = E_0 - \eta \langle F_z \rangle + \delta \langle F_z^2 \rangle. \tag{E.6}$$

To account for the conservation of particle number and magnetization in Eq. (E.1), one can introduce two Lagrange multipliers μ and η_0. With a homogeneous density or under SMA, the ground state structure is determined by the spin-dependent (anti-symmetric) part of the energy functional,

$$\begin{aligned} K &= \int d^3\vec{r} n[\frac{c_2 n}{2} \langle \vec{F} \rangle^2 - \tilde{\eta} \langle F_z \rangle + \delta \langle F_z^2 \rangle] && \text{(E.7a)} \\ &= \frac{c}{2} \langle \vec{F} \rangle^2 - \tilde{\eta} \langle F_z \rangle + \delta \langle F_z^2 \rangle, && \text{(E.7b)} \end{aligned}$$

where $c = c_2 \int \mathrm{d}^3 r \; n(r)^2$, and $\tilde{\eta} = \eta + \eta_0$. To further simplify this spin-dependent energy functional, we recall that

$$\begin{aligned} \langle F_x \rangle^2 &= \frac{1}{2} (\zeta_1^* \zeta_0 + \zeta_0^* \zeta_1 + \zeta_0^* \zeta_{-1} + \zeta_{-1}^* \zeta_0)^2, \\ \langle F_y \rangle^2 &= -\frac{1}{2} (-\zeta_1^* \zeta_0 + \zeta_0^* \zeta_1 - \zeta_0^* \zeta_{-1} + \zeta_{-1}^* \zeta_0)^2, \\ \langle F_z \rangle^2 &= (|\zeta_1|^2 - |\zeta_{-1}|^2)^2 = M^2, \\ \langle F_z^2 \rangle &= |\zeta_1|^2 + |\zeta_{-1}|^2 = 1 - \rho_0, \end{aligned}$$

where $\rho_i = |\zeta_i|^2$ with $\sum_{i=1}^3 \rho_i = 1$, and $M = \rho_1 - \rho_{-1}$. Then

$$\begin{aligned} \langle F \rangle^2 &= \langle F_x \rangle^2 + \langle F_y \rangle^2 + \langle F_z \rangle^2 && \text{(E.8a)} \\ &= 2(\zeta_1^* \zeta_0 + \zeta_0^* \zeta_{-1})(\zeta_0^* \zeta_1 + \zeta_{-1}^* \zeta_0) + (|\zeta_1|^2 - |\zeta_{-1}|^2)^2 && \text{(E.8b)} \\ &= 2 \left(\rho 1 \rho_0 + \zeta_0^{*2} \zeta_1 \zeta_{-1} + \zeta_0^2 \zeta_1^* \zeta_{-1}^* + \rho_{-1} \rho_0 \right) + M^2 && \text{(E.8c)} \\ &= 2 \left(\rho 1 \rho_0 + 2\rho_0 \sqrt{\rho_1 \rho_{-1}} \cos\theta + \rho_{-1} \rho_0 \right) + M^2. && \text{(E.8d)} \end{aligned}$$

Here we let $\zeta_i = \sqrt{\rho_i}\, e^{\theta_i}$, and we define the spinor phase to be $\theta \equiv \theta_1 + \theta_{-1} - 2\theta_0$. Minimizing $c\langle F\rangle^2$ requires

$$\theta = 0,\ c < 0, \tag{E.9}$$

$$\theta = \pi,\ c > 0. \tag{E.10}$$

Therefore,

$$\langle F\rangle^2 = 2\rho_0(\sqrt{\rho_1} \pm \sqrt{\rho_{-1}})^2 + M^2 \tag{E.11a}$$

$$= 2\rho_0 \left[(1-\rho_0) \pm \sqrt{(1-\rho_0)^2 - M^2}\right] + M^2, \tag{E.11b}$$

where "+" and "−" signs are for $c < 0$ and $c > 0$. Substitute back to Eq. (E.7), the spinor energy function is found as

$$K = c\rho_0 \left[(1-\rho_0 \pm \sqrt{(1-\rho_0)^2 - M^2}\right] + \frac{c}{2}M^2 - \eta M + \delta(1-\rho_0). \tag{E.12}$$

This is reminiscent of Eq. (5.28), with two additional terms, $\frac{c}{2}M^2 - \tilde{\eta}M$. These additional terms were omitted in Eq. (5.28) under conservation of magnetization. In a field with large gradient along the z direction, $\eta = \eta(z) = g_F \mu_B B' z$, where g_F is the Landé g-factor for electron, and μ_B is the Bohr magneton, the gradient will exert magnetic forces on m_1 and m_{-1} components and cause them to separate in space. In this circumstance, SMA is invalid and conservation of local magnetization does not hold. The ground state then presents a domain structure, and this structure can be found by minimizing Eq. (E.11) without conservation of magnetization. This kind of domain structures formed due to high field gradient has been observed by the MIT group in the anti-ferromagnetic Na $F = 1$ condensates [42].

When the field gradient is small such that the SMA is valid, the magnetization is conserved and minimization of K leads to the mean-field ground state in ref. [112]. In this thesis, the ground states we observed in the ^{87}Rb ferromagnetic $F = 1$ condensates are under validity of SMA and conservation of magnetization.

APPENDIX F

PROCEDURE FOR EXTRACTING C_2

As discussed in Chapter 3 , the density and the chemical potential of the condensate are often computed from the measured number of atoms, N, and the trap frequency, $\bar{\omega} = (\omega_x \omega_y \omega_z)^{1/3}$. Recall from Eqs. (3.28) and (3.32), the peak density is given as $n_0 = \mu/g$, where $g = 4\pi\hbar^2\bar{a}/m = c_0$ is the mean-field density interaction strength, and $\mu = (\frac{15\hbar^2 m^{1/2}}{2^{5/2}} N\bar{\omega}^3\bar{a})^{2/5}$ is the chemical potential. Here $\bar{a} = (2a_{F=2} + a_{F=0})/3$ is the averaged s-wave scattering length. However, measuring the trap frequencies and the absolute number of atoms in the condensate to within 15% are challenging. First, the parametric excitation technique that are used for measuring the trap frequencies is likely to excite superfluid modes of a condensate, which is not an integer multiple of the trap frequencies [28, 29]. Secondly, the trap depth is very shallow, typically 1 μK, and the trap frequencies are very low, which are more difficult to determine in general. On the other hand, measuring absolute number of atoms is always challenging. This is because an accurate measure of the imaging system efficiency is difficult to obtain. In addition, and absorption imaging can be affected by a stray field, since the optical transition ($|F = 2, m_F = 2\rangle \leftrightarrow |F' = 3, m_F = 3\rangle$)is field sensitive.

Alternatively, one can measure the density or the chemical potential directly from the expansion rate of condensates. Recall from Eq. 3.35a, when the reduced expansion time τ satisfies $\tau = t \cdot \omega_\perp \gg 1$, where t is the expansion time and $\omega_\perp$ is the trap frequency along the tight trap direction, the condensate radius is $R(t) \simeq \sqrt{\frac{2\mu}{m}}t = kt$. Here we define the expansion rate (slope) $k = \sqrt{2\mu/m}$. With the measured k, the chemical potential can be computed as $\mu = k^2 m/2$. To extract c, we measure the oscillation frequencies vs. populations, and then fit these data points to the theory, $c\sqrt{1-\rho_0^2}$ [114, 117], with free parameter c. Given that $c \equiv c_2 N \int |\phi|^4 d^3r$, where N is the total number of atoms, the spin

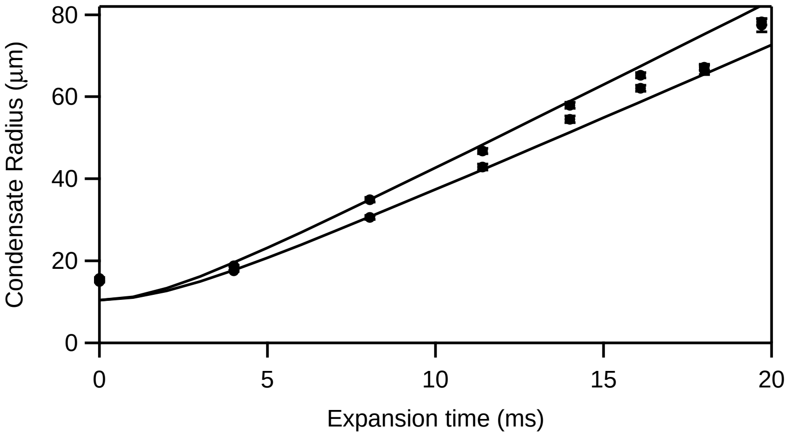

Figure F.1: BEC radius vs. expansion time. Measuring the expansion rate allows direct measurement of density. The solid curves are the theoretical predictions with 10 μm of imaging resolution, and the solid circles are the measured data. The theoretical predictions are deconvoluted from the imaging resolution and then fitted with a linear function to find the the slop k. The fitted slops are $k_{max} = 4.1$ μm/ms and $k_{min} = 3.6$ μm/ms. The deviation between the data and the theoretical predictions near time zero are due to that the optical densities are too high to measure the condensate radius correctly. In order to reduce the optical density, the absorption probe detuning is -5 MHz before 5 ms of drop time and -3 MHz after that.

interaction coefficient c_2 can be calculated as

$$c_2 = \frac{c}{N\int|\phi|^4\mathrm{d}^3r} = \frac{7}{2}\frac{c_0c}{k^2m}. \tag{F.1}$$

Here the averaged condensate density is given by,

$$N\int|\phi|^4\mathrm{d}^3r = \frac{4}{7}n_0 = \frac{4}{7}\frac{\mu}{g} = \frac{2}{7}\frac{k^2m}{c_0}, \tag{F.2}$$

where $n_0 = \mu/g$ is the peak density, and $g = (4\pi\hbar^2/m)\bar{a} = c_0$ is the density mean-field interaction strength. The details for finding the above integral will be given below.

With the measured $k = 3.9(4)$ μm/ms, the averaged condensate density is calculated to be $n_0 = 2.1(4)\times10^{14}$ cm^{-3}. Together with the measured $c = 4.3(3)$ Hz, the spin-dependent interaction coefficient is found to be $c_2 = -3.6(8)\times10^{-14}$ Hz/cm^3 or the difference of scattering lengthes $\Delta a = a_2 - a_0 = -1.4(3)$ Bohr. Note that the negative sign of c_2 is not determined by the measurements here, but was determined from studies of spinor ground states and from the miscibilities of different spin components which are shown in Chapter 6-8.

Computation of $\int |\phi|^4 \mathrm{d}^3 r$ The normalized Thomas-Fermi density profile is given by

$$\frac{1}{N} n(r) = |\phi|^2 = \frac{1}{Ng} \max[(\mu - \frac{1}{2} m\omega^2 r^2), 0],$$

where $n(r)$ is the condensate density, N is the total number of atoms, and $g = \frac{4\pi\hbar^2}{m}\bar{a} = c_0$. The condensate radius R is calculated as

$$R = \left(\frac{15Nc_0}{8\pi\frac{1}{2}m\omega^2}\right)^{1/5}, \tag{F.3}$$

which is solved by substituting the equation $\mu = \frac{1}{2}m\omega^2 R^2$ into the normalization integral, $\int_0^R |\phi|^2 \, \mathrm{d}^3 r = 1$. That is

$$\begin{aligned}\int_0^R |\phi|^2 \, d^3 r &= \frac{1}{Nc_0}\frac{1}{2}m\omega^2 \int_0^R (R^2 - r^2) 4\pi r^2 dr \\ &= \frac{4\pi m\omega^2 R^5}{15Nc_0} \\ &= 1.\end{aligned}$$

Given $\mu = \frac{1}{2}m\omega^2 R^2$, we also find that $R^3 = \frac{15Nc_0}{8\pi\mu}$. Substitute R into the following integral,

$$\begin{aligned}\int |\phi|^4 \, \mathrm{d}^3 r &= 4\pi(\frac{\frac{1}{2}m\omega^2}{Nc_0})^2 \int_0^R (R^2 - r^2)^2 r^2 \mathrm{d}r \\ &= 4\pi(\frac{15}{8\pi})^2 \frac{8}{105} R^{-3} \\ &= \frac{4}{7}\frac{\mu}{Nc_0}.\end{aligned}$$

From the above intetral, it is readily found that

$$N \int |\phi|^4 \mathrm{d}^3 r = \frac{4}{7}\frac{\mu}{c_0} = \frac{4}{7} n_0,$$

where the peak density $n_0 = \mu / c_0$.

REFERENCES

[1] M. H. Anderson, J. R. Ensher, M. R. Matthews, C. E. Wieman, and E. A. Cornell, "Observation of Bose-Einstein Condensation in a Dilute Atomic Vapor," *Science* **269**, 198 (1995).

[2] C. C. Bradley, C. A. Sackett, J. J. Tollett, and R. G. Hulet, "Evidence of Bose-Einstein Condensation in an Atomic Gas with Attractive Interactions," *Phys. Rev. Lett.* **75**, 1687 (1995).

[3] K. B. Davis *et al.*, "Bose-Einstein Condensation in a Gas of Sodium Atoms," *Phys. Rev. Lett.* **75**, 3969 (1995).

[4] W. C. Stwalley and L. H. Nosanow, "Possible New Quantum Systems," *Phys. Rev. Lett.* **36**, 910 (1976).

[5] I. F. Silvera and J. T. M. Walraven, "Stabilization of Atomic-Hydrogen at Low-Temperature," *Phys. Rev. Lett.* **44**, 164 (1980).

[6] E. L. Raab, M. Prentiss, A. Cable, S. Chu, and D. E. Pritchard, "Trapping of Neutral Sodium Atoms with Radiation Pressure," *Phys. Rev. Lett.* **59**, 2631 (1987).

[7] C. Monroe, W. Swann, H. Robinson, and C. Wieman, "Very Cold Trapped Atoms in a Vapor Cell," *Phys. Rev. Lett.* **65**, 1571 (1990).

[8] E. A. Cornell, J. R. Ensher, and C. E. Wieman, "Experiments in dilute atomic Bose-Einstein condensation," in *International School of Physics "Enrico Fermi", Course CXL*, edited by M. Inguscio, S. Stringari, and C. E. Wieman Varenna, Lake Como, Italy 1999 IOS Press.

[9] W. Ketterle, D. S. Durfee, and D. M. Stamper-Kurn, "Making, probing and understanding Bose-Einstein condensates (cond-mat/9904034)," in *International School of Physics "Enrico Fermi", Course CXL*, edited by M. Inguscio, S. Stringari, and C. E. Wieman Varenna, Lake Como, Italy 1999 IOS Press.

[10] M. R. Andrews *et al.*, "Observation of interference between two Bose condensates," *Science* **275**, 637 (1997).

[11] I. Bloch, T. W. Hansch, and T. Esslinger, "measurement of the spatial coherence of a trapped bose gas at the phase transition," *Nature* **403**, 166 (2000).

[12] B. P. Anderson and M. A. Kasevich, "Macroscopic quantum interference from atomic tunnel arrays," *Science* **282**, 1686 (1998).

[13] M. Albiez *et al.*, "Direct observation of tunneling and nonlinear self-trapping in a single bosonic Josephson junction," *Phys. Rev. Lett.* **95**, 010402 (2005).

[14] M. Greiner, O. Mandel, T. Esslinger, T. W. Hansch, and I. Bloch, "Quantum phase transition from a superfluid to a Mott insulator in a gas of ultracold atoms," *Nature* **415**, 39 (2002).

[15] M. O. Mewes *et al.*, "Output coupler for Bose-Einstein condensed atoms," *Phys. Rev. Lett.* **78**, 582 (1997).

[16] E. W. Hagley *et al.*, "A well-collimated quasi-continuous atom laser," *Science* **283**, 1706 (1999).

[17] I. Bloch, T. W. Hansch, and T. Esslinger, "Atom laser with a cw output coupler," *Phys. Rev. Lett.* **82**, 3008 (1999).

[18] E. A. Burt *et al.*, "Coherence, correlations, and collisions: What one learns about Bose-Einstein condensates from their decay," *Phys. Rev. Lett.* **79**, 337 (1997).

[19] S. Folling *et al.*, "Spatial quantum noise interferometry in expanding ultracold atom clouds," *Nature* **434**, 481 (2005).

[20] G. Baym and C. J. Pethick, "Ground-state properties of magnetically trapped Bose-condensed rubidium gas," *Phys. Rev. Lett.* **76**, 6 (1996).

[21] F. Dalfovo and S. Stringari, "Bosons in anisotropic traps: Ground state and vortices," *Phys. Rev. A* **53**, 2477 (1996).

[22] C. C. Bradley, C. A. Sackett, and R. G. Hulet, "Bose-Einstein condensation of lithium: Observation of limited condensate number," *Phys. Rev. Lett.* **78**, 985 (1997).

[23] E. A. Donley *et al.*, "Dynamics of collapsing and exploding Bose-Einstein condensates," *Nature* **412**, 295 (2001).

[24] C. J. Pethick and H. Smith, *Bose-Einstein Condensation in Dilute Gases* (Cambridge University Press, Cambridge, UK, 2002).

[25] M. R. Matthews *et al.*, "Vortices in a Bose-Einstein condensate," *Phys. Rev. Lett.* **83**, 2498 (1999).

[26] K. Madison, F. Chevy, W. Wohlleben, and J. Dalibard, "Vortex Formation in a Stirred Bose-Einstein Condensate," *Phys. Rev. Lett.* **84**, 806 (2000).

[27] J. R. Abo-Shaeer, C. Raman, J. M. Vogels, and W. Ketterle, "Observation of vortex lattices in Bose-Einstein condensates," *Science* **292**, 476 (2001).

[28] D. S. Jin, J. R. Ensher, M. R. Matthews, C. E. Wieman, and E. A. Cornell, "Collective Excitations of a Bose-Einstein Condensate in a Dilute Gas," *Phys. Rev. Lett.* **77**, 420 (1996).

[29] M. O. Mewes *et al.*, "Collective excitations of a Bose-Einstein condensate in a magnetic trap," *Phys. Rev. Lett.* **77**, 988 (1996).

[30] M. R. Andrews *et al.*, "Propagation of sound in a Bose-Einstein condensate," *Phys. Rev. Lett.* **79**, 553 (1997).

[31] S. Burger *et al.*, “Dark solitons in Bose-Einstein condensates,” *Phys. Rev. Lett.* **83**, 5198 (1999).

[32] J. Denschlag *et al.*, “Generating solitons by phase engineering of a Bose-Einstein condensate,” *Science* **287**, 97 (2000).

[33] K. E. Strecker, G. B. Partridge, A. G. Truscott, and R. G. Hulet, “Formation and propagation of matter-wave soliton trains,” *Nature* **417**, 150 (2002).

[34] M. D. Barrett, J. A. Sauer, and M. S. Chapman, “All-optical formation of an atomic Bose-Einstein condensate,” *Phys. Rev. Lett.* **87**, 010404 (2001).

[35] D. M. Stamper-Kurn *et al.*, “Optical confinement of a Bose-Einstein condensate,” *Phys. Rev. Lett.* **80**, 2027 (1998).

[36] Y. Takasu *et al.*, “Spin-singlet Bose-Einstein condensation of two-electron atoms,” *Phys. Rev. Lett.* **91**, 040404 (2003).

[37] W. Hansel, P. Hommelhoff, T. W. Hansch, and J. Reichel, “Bose-Einstein condensation on a microelectronic chip,” *Nature* **413**, 498 (2001).

[38] H. Ott, J. Fortagh, G. Schlotterbeck, A. Grossmann, and C. Zimmermann, “Bose-Einstein condensation in a surface microtrap,” *Phys. Rev. Lett.* **8723**, 230401 (2001).

[39] T. L. Ho, “Spinor Bose condensates in optical traps,” *Phys. Rev. Lett.* **81**, 742 (1998).

[40] T. Ohmi and K. Machida, “Bose-Einstein condensation with internal degrees of freedom in alkali atom gases,” *J. Phys. Soc. Jpn.* **67**, 1822 (1998).

[41] C. J. Myatt, E. A. Burt, R. W. Ghrist, E. A. Cornell, and C. E. Wieman, “Production of two overlapping Bose-Einstein condensates by sympathetic cooling,” *Phys. Rev. Lett.* **78**, 586 (1997).

[42] J. Stenger *et al.*, “Spin domains in ground-state Bose-Einstein condensates,” *Nature* **396**, 345 (1998).

[43] A. Grlitz *et al.*, “Sodium Bose-Einstein condensates in the F=2 state in a large-volume optical trap,” *Phys. Rev. Lett.* **90**, 010404 (2003).

[44] H. Schmaljohann *et al.*, “Dynamics of F=2 spinor Bose-Einstein condensates,” *Phys. Rev. Lett.* **92**, 040402 (2004).

[45] M. S. Chang *et al.*, “Observation of spinor dynamics in optically trapped Rb-87 Bose-Einstein condensates,” *Phys. Rev. Lett.* **92**, 140403 (2004).

[46] A. J. Leggett, “Theoretical Description of New Phases of Liquid-He-3,” *Rev. Mod. Phys.* **47**, 331 (1975).

[47] J. C. Wheatley, “Experimental Properties of Superfluid He-3,” *Rev. Mod. Phys.* **47**, 415 (1975).

[48] D. J. Dean and M. Hjorth-Jensen, “Pairing in nuclear systems: from neutron stars to finite nuclei,” *Rev. Mod. Phys.* **75**, 607 (2003).

[49] A. P. M. Maeno and Y., “The superconductivity of Sr_2RuO_4 and the physics of spin-triplet pairing,” *Rev. Mod. Phys.* **75**, 657 (2003).

[50] C. V. Ciobanu, S. K. Yip, and T. L. Ho, “Phase diagrams of F=2 spinor Bose-Einstein condensates,” *Phys. Rev. A* **61**, 033607 (2000).

[51] E. A. Cornell, D. S. Hall, M. R. Matthews, and C. E. Wieman, “Having it both ways: Distinguishable yet phase-coherent mixtures of Bose-Einstein condensates,” *J. Low Temp. Phys.* **113**, 151 (1998).

[52] H. J. Miesner *et al.*, “Observation of metastable states in spinor Bose-Einstein condensates,” *Phys. Rev. Lett.* **82**, 2228 (1999).

[53] D. M. Stamper-Kurn *et al.*, “Quantum tunneling across spin domains in a Bose-Einstein condensate,” *Phys. Rev. Lett.* **83**, 661 (1999).

[54] C. K. Law, H. Pu, and N. P. Bigelow, “Quantum spins mixing in spinor Bose-Einstein condensates,” *Phys. Rev. Lett.* **81**, 5257 (1998).

[55] N. N. Klausen, J. L. Bohn, and C. H. Greene, “Nature of spinor Bose-Einstein condensates in rubidium,” *Phys. Rev. A* **64**, 053602 (2001).

[56] E. G. M. van Kempen, S. J. J. M. F. Kokkelmans, D. J. Heinzen, and B. J. Verhaar, “Interisotope determination of ultracold rubidium interactions from three high-precision experiments,” *Phys. Rev. Lett.* **88**, 093201 (2002).

[57] D. A. Steck, “Rubidium 87 D Line Data,” (2003).

[58] J. Vanier and C. Audoin, *The quantum physics of atomic frequency standards* (A. Hilger, Philadelphia, 1988).

[59] H. J. Metcalf and P. van der Straten, *Laser Cooling and Trapping* (Springer-Verlag, New York, 1999).

[60] K. B. Macadam, A. Steinbach, and C. Wieman, “A Narrow-Band Tunable Diode-Laser System with Grating Feedback, and a Saturated Absorption Spectrometer for Cs and Rb,” *Am. J. Phys.* **60**, 1098 (1992).

[61] W. Demtroder, *Laser Spectroscopy*, 2nd ed. (Springer, New York, 1996).

[62] M. D. Barrett, *A Quest for BEC: An all-optical alternative*, PhD thesis Georgia Institute of Technology 2002.

[63] C. C. Bradley, J. Chen, and R. G. Hulet, “Instrumentation for the Stable Operation of Laser-Diodes,” *Rev. Sci. Inst.* **61**, 2097 (1990).

[64] C. E. Wieman and L. Hollberg, “Using Diode-Lasers for Atomic Physics,” *Rev. Sci. Inst.* **62**, 1 (1991).

[65] K. G. Libbrecht and J. L. Hall, “A Low-Noise High-Speed Diode-Laser Current Controller,” *Rev. Sci. Inst.* **64**, 2133 (1993).

[66] S. Friebel, R. Scheunemann, J. Walz, T. W. Hansch, and M. Weitz, “Laser cooling in a CO_2-laser optical lattice,” *Appl. Phy. B* **67**, 699 (1998).

[67] J. D. Jackson, *Classical Electrodynamics*, 2nd ed. (Willey, New York, 1975).

[68] E. A. Cornell, J. R. Ensher, and C. E. Wieman, "Experiments in dilute atomic Bose-Einstein condensation (cond-mat/9903109)," in *International School of Physics "Enrico Fermi" on Bose-Einstein Condensation in Atomic Gases*, edited by M. Inguscio, S. Stringari, and C. E. Wieman p. 15 IOS Press 1998.

[69] S. Chu, J. E. Bjorkholm, A. Ashkin, and A. Cable, "Experimental Observation of Optically Trapped Atoms," *Phys. Rev. Lett.* **57**, 314 (1986).

[70] C. S. Adams, H. J. Lee, N. Davidson, M. Kasevich, and S. Chu, "Evaporative Cooling in a Crossed Dipole Trap," *Phys. Rev. Lett.* **74**, 3577 (1995).

[71] T. Takekoshi, J. R. Yeh, and R. J. Knize, "Quasi-electrostatic trap for neutral atoms," *Opt. Comm.* **114**, 421 (1995).

[72] R. Grimm, M. Weidemuller, and Y. B. Ovchinnikov, "Optical dipole traps for neutral atoms," *Adv. Atom. Mol. Opt. Phys.* **42**, 95 (2000).

[73] D. J. Han, M. T. DePue, and D. S. Weiss, "Loading and compressing Cs atoms in a very far-off-resonant light trap," *Phy. Rev. A* **6302**, 023405 (2001).

[74] A. Robert *et al.*, "A Bose-Einstein Condensate of Metastable Atoms," *Science* **292**, 461 (2001).

[75] H. Haken and H. C. Wolf, *Molecular Physics and Elements of Quantum Chemistry* (Springer, Berlin, 1995).

[76] F. Reif, *Fundametals of Statistical and Thermal Physics* (McGraw Hill, New York, 1965).

[77] S. Friebel, C. D'Andrea, J. Walz, M. Weitz, and T. W. Hansch, "CO_2-laser optical lattice with cold rubidium atoms," *Phy. Rev. A* **57**, R20 (1998).

[78] V. I. Arnold, *Mathemtaical Methods of Classical Mechanics*, 2nd ed. (Springer-Verlag, New York, 1988).

[79] F. Dalfovo, L. Pitaevskii, and S. Stringari, "Order parameter at the boundary of a trapped Bose gas," *Phys. Rev. A* **54**, 4213 (1996).

[80] Y. Castin and R. Dum, "Bose-Einstein condensates in time dependent traps," *Phys. Rev. Lett.* **77**, 5315 (1996).

[81] F. Gerbier *et al.*, "Experimental study of the thermodynamics of an interacting trapped Bose-Einstein condensed gas," *Phy. Rev. A* **70**, 013607 (2004).

[82] G. Cennini, G. Ritt, C. Geckeler, and M. Weitz, "All-optical realization of an atom laser," *Phys. Rev. Lett.* **91**, 240408 (2003).

[83] T. Kinoshita, T. Wenger, and S. Weiss, David, "All-optical Bose-Einstein condensation using a compressible crossed dipole trap," *Phys. Rev. A* **71**, 011602 (2005).

[84] T. Weber, J. Herbig, M. Mark, H. C. Nagerl, and R. Grimm, "Bose-Einstein condensation of cesium," *Science* **299**, 232 (2003).

[85] W. D. Phillips 2005.

[86] S. R. Granade, M. E. Gehm, K. M. O'Hara, and J. E. Thomas, "All-optical production of a degenerate Fermi gas," *Phys. Rev. Lett.* **88**, 120405 (2002).

[87] R. Scheunemann, F. S. Cataliotti, T. W. Hansch, and M. Weitz, "An optical lattice with single lattice site optical control for quantum engineering," *J. Opt. B* **2**, 645 (2000).

[88] J. H. Denschlag *et al.*, "A Bose-Einstein condensate in an optical lattice," *J. Phys. B* **35**, 3095 (2002).

[89] D. Jaksch, H. J. Briegel, J. I. Cirac, C. W. Gardiner, and P. Zoller, "Entanglement of atoms via cold controlled collisions," *Phys. Rev. Lett.* **82**, 1975 (1999).

[90] G. K. Brennen, C. M. Caves, F. S. Jessen, and I. H. Deutsch, "Quantum logic gates in optical lattices," *Phys. Rev. Lett.* **82**, 1060 (1999).

[91] S. Kuhr *et al.*, "Deterministic delivery of a single atom," *Science* **293**, 278 (2001).

[92] J. A. Sauer, K. M. Fortier, M. S. Chang, C. D. Hamley, and M. S. Chapman, "Cavity QED with optically transported atoms," *Phy. Rev. A* **69**, 051804 (2004).

[93] S. Chu, "The manipulation of neutral particles," *Rev. Mod. Phys.* **70**, 685 (1998).

[94] W. D. Phillips, "Laser cooling and trapping of neutral atoms," *Rev. Mod. Phys.* **70**, 721 (1998).

[95] T. A. Savard, K. M. OHara, and J. E. Thomas, "Laser-noise-induced heating in far-off resonance optical traps," *Phy. Rev. A* **56**, R1095 (1997).

[96] M. E. Gehm, K. M. O'Hara, T. A. Savard, and J. E. Thomas, "Dynamics of noise-induced heating in atom traps," *Phy. Rev. A* **58**, 3914 (1998).

[97] T. Ido, Y. Isoya, and H. Katori, "Optical-dipole trapping of Sr atoms at a high phase-space density," *Phys Rev A* **61**, 061403 (2000).

[98] T. Takekoshi and R. J. Knize, "CO_2 laser trap for cesium atoms," *Opt. Lett.* **21**, 77 (1996).

[99] S. J. M. Kuppens, K. L. Corwin, K. W. Miller, T. E. Chupp, and C. E. Wieman, "Loading an optical dipole trap," *Phy. Rev. A* **62**, 013406 (2000).

[100] K. M. O'Hara, S. R. Granade, M. E. Gehm, and J. E. Thomas, "Loading dynamics of CO_2 laser traps," *Phy. Rev. A* **63**, 043403 (2001).

[101] Y. Takasu *et al.*, "High-density trapping of cold ytterbium atoms by an optical dipole force," *Phys. Rev. Lett.* **90**, 023003 (2003).

[102] C. Orzel, A. K. Tuchman, M. L. Fenselau, M. Yasuda, and M. A. Kasevich, "Squeezed states in a Bose-Einstein condensate," *Science* **291**, 2386 (2001).

[103] W. K. Hensinger *et al.*, "Dynamical tunnelling of ultracold atoms," *Nature* **412**, 52 (2001).

[104] F. S. Cataliotti *et al.*, "Josephson junction arrays with Bose-Einstein condensates," *Science* **293**, 843 (2001).

[105] M. Greiner, O. Mandel, T. W. Hansch, and I. Bloch, "Collapse and revival of the matter wave field of a Bose-Einstein condensate," *Nature* **419**, 51 (2002).

[106] D. C. O'Shea, *Elements of modern optical design* (Wiley, New York, 1985).

[107] K. B. Davis, M. O. Mewes, and W. Ketterle, "An Analytical Model for Evaporative Cooling of Atoms," *Appl. Phys. B* **60**, 155 (1995).

[108] D. S. Hall, M. R. Matthews, J. R. Ensher, C. E. Wieman, and E. A. Cornell, "Dynamics of component separation in a binary mixture of Bose-Einstein condensates," *Phys. Rev. Lett.* **81**, 1539 (1998).

[109] D. S. Hall, M. R. Matthews, C. E. Wieman, and E. A. Cornell, "Measurements of relative phase in two-component Bose-Einstein condensates," *Phys. Rev. Lett.* **81**, 1543 (1998).

[110] J. E. Williams and M. J. Holland, "Preparing topological states of a Bose-Einstein condensate," *Nature* **401**, 568 (1999).

[111] M. Koashi and M. Ueda, "Exact eigenstates and magnetic response of spin-1 and spin-2 Bose-Einstein condensates," *Phys. Rev. Lett.* **84**, 1066 (2000).

[112] W. X. Zhang, S. Yi, and L. You, "Mean field ground state of a spin-1 condensate in a magnetic field," *New J. Phys.* **5**, 77 (2003).

[113] E. V. Goldstein and P. Meystre, "Quantum theory of atomic four-wave mixing in Bose-Einstein condensates," *Phys. Rev. A* **59**, 3896 (1999).

[114] H. Pu, C. K. Law, S. Raghavan, J. H. Eberly, and N. P. Bigelow, "Spin-mixing dynamics of a spinor Bose-Einstein condensate," *Phys. Rev. A* **60**, 1463 (1999).

[115] J. P. Burke, P. S. Julienne, C. J. Williams, Y. B. Band, and M. Trippenbach, "Four-wave mixing in Bose-Einstein condensate systems with multiple spin states," *Phys. Rev. A* **70**, 033606 (2004).

[116] D. R. Romano and E. J. V. de Passos, "Population and phase dynamics of F=1 spinor condensates in an external magnetic field," *Phys. Rev. A* **70**, 043614 (2004).

[117] W. Zhang, D. L. Zhou, M.-S. Chang, M. S. Chapman, and L. You, "Coherent spin mixing dynamics in a spin-1 atomic condensate," *Phys. Rev. A* **72**, 013602 (2005).

[118] A. E. Leanhardt, Y. Shin, D. Kielpinski, D. E. Pritchard, and W. Ketterle, "Coreless vortex formation in a spinor Bose-Einstein condensate," *Phys. Rev. Lett.* **90**, 140403 (2003).

[119] T. Isoshima, K. Machida, and T. Ohmi, "Spin-domain formation in spinor Bose-Einstein condensation," *Phys. Rev. A* **60**, 4857 (1999).

[120] L. M. Duan, J. I. Cirac, and P. Zoller, "Quantum entanglement in spinor Bose-Einstein condensates," *Phys. Rev. A* **65**, 033619 (2002).

[121] H. Pu and P. Meystre, “Creating macroscopic atomic Einstein-Podolsky-Rosen states from Bose-Einstein condensates,” *Phys. Rev. Lett.* **85**, 3987 (2000).

[122] J. P. Burke, C. H. Greene, and J. L. Bohn, “Multichannel cold collisions: Simple dependences on energy and magnetic field,” *Phys. Rev. Lett.* **81**, 3355 (1998).

[123] D. Stamper-Kurn and W. Ketterle, “Spinor Condensates and Light Scattering From Bose-Einstein Condensates (cond-mat/0005001 v1 29),” in *Les Houches Summer School, Section LXXII*, edited by R. Kaiser, C. Westbrook, and F. David pp. 139–208 Les Houches, France 1999 Springer, Berlin.

[124] H. Pu, S. Raghavan, and N. P. Bigelow, “Manipulating spinor condensates with magnetic fields: Stochastization, metastability, and dynamical spin localization,” *Phy. Rev. A* **61**, 023602 (2000).

[125] T. Kuwamoto, K. Araki, T. Eno, and T. Hirano, “Magnetic field dependence of the dynamics of Rb-87 spin-2 Bose-Einstein condensates,” *Phys. Rev. A* **69**, 063604 (2004).

[126] M. R. Matthews *et al.*, “Watching a superfluid untwist itself: Recurrence of rabi oscillations in a Bose-Einstein condensate,” *Phys. Rev. Lett.* **83**, 3358 (1999).

[127] S. Yi, O. E. Mustecaplioglu, C. P. Sun, and L. You, “Single-mode approximation in a spinor-1 atomic condensate,” *Phy. Rev. A* **66**, 011601 (2002).

[128] A. Barone and G. Paterno, *Physics and applications of the Josephson effect* (Wiley, New York, 1982).

[129] J. Javanainen, “Oscillatory Exchange of Atoms between Traps Containing Bose Condensates,” *Phys. Rev. Lett.* **57**, 3164 (1986).

[130] A. Smerzi, S. Fantoni, S. Giovanazzi, and S. R. Shenoy, “Quantum coherent atomic tunneling between two trapped Bose-Einstein condensates,” *Phys. Rev. Lett.* **79**, 4950 (1997).

[131] J. C. Davis and R. E. Packard, “Superfluid 3He weak links,” *Rev. Mod. Phys.* **74**, 741 (2001).

[132] L. You, “Creating Maximally Entangled Atomic States in a Bose-Einstein Condensate,” *Phys. Rev. Lett.* **90**, 030402 (2003).

[133] M. Erhard, H. Schmaljohann, J. Kronjager, K. Bongs, and K. Sengstock, “Bose-Einstein condensation at constant temperature,” *Phy. Rev. A* **70**, 031602 (2004).

[134] T. Isoshima, T. Ohmi, and K. Machida, “Double phase transitions in magnetized spinor Bose-Einstein condensation,” *J. Phy. Soc. Jpn.* **69**, 3864 (2000).

[135] W. X. Zhang, S. Yi, and L. You, “Bose-Einstein condensation of trapped interacting spin-1 atoms,” *Phy. Rev. A* **70**, 043611 (2004).

[136] M. D. Barrett *et al.*, “All-Optical Atomic Bose-Einstein Condensates,” in *XVIII International Conference on Atomic Physics*, edited by H. R. Sadeghpour, E. J. Heller, and D. E. Pritchard Cambridge, MA, USA 2002 World Scientific.

[137] T. L. Ho and S. K. Yip, "Fragmented and single condensate ground states of spin-1 Bose gas," *Phys. Rev. Lett.* **84**, 4031 (2000).

[138] J. R. Ensher, D. S. Jin, M. R. Matthews, C. E. Wieman, and E. A. Cornell, "Bose-Einstein condensation in a dilute gas: Measurement of energy and ground-state occupation," *Phys. Rev. Lett.* **77**, 4984 (1996).

[139] E. A. Donley, N. R. Claussen, S. T. Thompson, and C. E. Wieman, "Atom-molecule coherence in a Bose-Einstein condensate," *Nature* **417**, 529 (2002).

[140] M. Greiner, C. A. Regal, and D. S. Jin, "Emergence of a molecular Bose-Einstein condensate from a Fermi gas," *Nature* **426**, 537 (2003).

[141] M. Tinkham, *Introduction to superconductivity*, 2nd ed. (McGraw Hill, New York, 1996).

[142] S. Shapiro, "Josephson Currents in Superconducting Tunneling: The Effect of Microwaves and Other Observations," *Phys. Rev. Lett.* **11**, 80 (1963).

[143] L. Deng *et al.*, "Four-wave mixing with matter waves," *Nature* **398**, 218 (1999).

[144] A. Widera *et al.*, "Coherent collisional spin dynamics in optical lattices," *Phys. Rev. Lett.* **95**, 190405 (2005).

[145] J. Kronjager *et al.*, "Evolution of a spinor condensate: Coherent dynamics, dephasing, and revivals," *Physical Review A* **72**, 063619 (2005).

[146] M.-S. Chang, Q. Qin, W. Zhang, L. You, and M.-S. Chang, "Coherent Spinor dynamics in a spin-1 Bose condensate," *Nature Physics* **1**, 111 (2005).

[147] G. P. Agrawal, *Nonlinear Fiber Optics* (Academic Press, Boston, 1989).

[148] N. P. Robins, W. P. Zhang, E. A. Ostrovskaya, and Y. S. Kivshar, "Modulational instability of spinor condensates," *Phy. Rev. A* **64**, 021601 (2001).

[149] P. Ao and S. T. Chui, "Binary Bose-Einstein condensate mixtures in weakly and strongly segregated phases," *Phys. Rev. A* **58**, 4836 (1998).

[150] W. Zhang, D. L. Zhou, M.-S. Chang, M. S. Chapman, and L. You, "Dynamical instability and domain formation in a spin-1 Bose condensate," *Phys. Rev. Lett.* **95**, 180403 (2005).

[151] H. Saito and M. Ueda, "Spontaneous magnetization and structure formation in a spin-1 ferromagnetic Bose-Einstein condensate," *Phy. Rev. A* **72**, 023610 (2005).